SPARK PLASMA SINTERING OF TANTALUM CARBIDE AND GRAPHENE REINFORCED TANTALUM CARBIDE COMPOSITES

By

AJITH KUMAR KALLURI

Bachelor of Science in Mechanical Engineering

VIT University

Vellore, India

2010

Submitted to the Faculty of the
Graduate College of the
Oklahoma State University
in partial fulfillment of
the requirements for
the Degree of
MASTER OF SCIENCE
December, 2012

SPARK PLASMA SINTERING OF TANTALUM CARBIDE AND GRAPHENE REINFORCED TANTALUM CARBIDE COMPOSITES

Thesis Approved:

Dr. Sandip P. Harimkar

Thesis Adviser

Dr. A. Kaan Kalkan

Dr. Raman P. Singh

ACKNOWLEDGEMENTS

I would like to thank my advisor Dr. Sandip P. Harimkar for his kind advise, guidance, and patience throughout my masters. I would also be grateful to Dr. A. Kaan Kalkan and Dr. Raman P. Singh for being my committee members and their valuable suggestions throughout my thesis.

I would like to convey my deepest sense of gratitude to Ashish Singh for his valuable suggestions, support, and care, Sriharsha Karumuri for his encouragement, moral support and Sudheer Bandla for his help with my thesis. I could not have completed my thesis without their help. It will take a life time to forget the precious time, love and support which they gave when in need. I would also like to thank Amy Aurilio for her help with my thesis write up.

Last but not the least; I am very grateful to my parents (Ramesh Babu Kalluri and Sarada Gogineni) and my sister (Divya Sree Kalluri) for their love, support and encouragement throughout my career. Heartful thanks to my uncle Dr. Sridhar Gogineni, his wife Manasa Gogineni, my sister Neelima Kalluri and my very lovable niece Sreeja Gogineni who never let me miss home. Special thanks to Venkata Ramana Gogineni, Srihari Gogineni, Sudhakar Yalamanchili, Amar Kumar Kakumanu, Srinivas Musunuru and their family members for their affection, support and advice. I would like to thank Vamsi Krishna Adusumalli, Phaneendra Sakhamuri and Preetham Kumar Kuknoor for being my best friends from my childhood. I am also thankful to my friends Kavitha Madhuri Inampudi, Harsha Vardhan Reddy, Harinath Reddy, Karthik Reddy Gade, Marri

Nishikanth Reddy, Dileep Reddy Nagireddygari, and Meka brothers (Satish and Supreeth). The journey during my masters became pleasant with good companions; especially I would like to thank Satish Garla, Abhinay Goud Burra, Santosh Resu, Pardhasaradhi Repalli, Murali Krishna Kondurubhaskara, Yogesh Pothiganti, Sowmya Nellutla and Gargeyi Baipa for being good friends. I thank Gargeyi Baipa, Arjun Rajakutty, Govindraajan, Amin, Timi and Teejay for the enlightening discussions.

I would like to thank John Degeorge, Andrew Arterbery, Anthony Parson, Eugene Cunningham for employing me at the library. I would also like to acknowledge Kaitlyn Gregg, Ramandeep Singh, Andreas Missailidis, Melissa Smith and other colleagues for their constant support.

Name: AJITH KUMAR KALLURI

Date of Degree: December, 2012

Title of Study: SPARK PLASMA SINTERING OF TANTALUM CARBIDE AND GRAPHENE REINFORCED TANTALUM CARBIDE CERAMIC COMPOSITES.

Major Field: Mechanical and Aerospace Engineering

Abstract:

Tantalum carbide (TaC), an ultra-high temperature ceramic (UHTC), is well known for its exceptional properties such as high hardness (15-19 GPa), melting point (3950 °C), elastic modulus (537 GPa), chemical resistance, and thermal shock resistance. To make TaC to be the future material for hypersonic vehicles, it is required to improve its thermal conductivity, strength, and fracture toughness. Researchers have previously reinforced TaC ceramic with carbides of silicon and boron as well as carbon nanotubes (CNTs), however, these reinforcements either undergo chemical changes or induce defects in the matrix during processing. In addition, these reinforcements exhibit a very minimal improvement in the properties. In the present work, we attempted to improve TaC fracture toughness by reinforcing with graphene nano-platelets (GNPs) and processing through spark plasma sintering at high temperature of 2000 °C, pressure of 70 MPa, and soaking time of 10 min. In addition, we investigated the active densification mechanism during SPS of TaC powder and the effect of ball milling time on mechanical properties of sintered TaC.

A relative density of >96% was achieved using SPS of monolithic TaC (<3 μm). Ball milling improved the sintering kinetics and improved the mechanical properties (microhardness, bi-axial flexural strength, and indentation fracture toughness). Activation energy (100 kJ/mol) and stress exponent (1.2) were obtained using the analytical model developed for power-law creep. Grain boundary sliding is proposed as active densification mechanism based on these calculations. Reinforcing GNPs (2-6 vol.%) in the TaC matrix improved relative density (99.8% for TaC-6 vol.% GNP). Also ~150% and ~180% increase in flexural strength and fracture toughness, respectively, was observed for TaC-6 vol.% GNP composite. The significant improvement in these properties is attributed to improved densification and toughening mechanisms such as sheet pull-out and crack deflection due to reinforcement of graphene. Uniform dispersion of GNPs in the TaC matrix is observed from microstructural analysis. Raman spectroscopy analysis also indicated that GNPs are successfully retained in sintered TaC-GNP composites without any damage.

TABLE OF CONTENTS

Chapter Page

LIST OF TABLES

LIST OF FIGURES

CHAPTER 1

INTRODUCTION

1.1 Introduction

Tantalum carbide (TaC), an ultra-high temperature ceramic (UHTC), is well known for its exceptional properties such as high hardness (15-19 GPa), melting point (3950 °C), elastic modulus (537 GPa), chemical resistance, and thermal shock resistance [1]. To make TaC to be the future material for hypersonic vehicles, it is required to improve its thermal conductivity, strength, and fracture toughness. Researchers have previously reinforced TaC ceramic with carbides of silicon and boron as well as carbon nanotubes (CNTs), however, these reinforcements either undergo chemical changes or induce defects in the matrix during processing. In addition, these reinforcements exhibit a very minimal improvement in the properties. In this study, we reinforced TaC with graphene nano-platelets (GNPs), that have excellent tensile strength (130 GPa) and high Young's modulus (0.5-1 TPa) [2]. The effect of reinforcement content on densification behavior and mechanical properties of spark plasma sintered TaC-GNP composites was reported. This chapter includes the literature review on processing, properties, and applications of various UHTCs followed by detailed review on SPS processing of reinforced TaC composites.

1.2 Ultra high temperature ceramics (UHTCs): properties and applications

The ceramics that possess melting points higher than 2500 °C are generally referred to as UHTCs The search for high temperature materials initiated with the development of atmospheric re-entry vehicles and hypersonic flight vehicles [3, 4]. These applications require materials that can withstand high temperatures and extremely reactive environments. Therefore, the materials used for these applications must be resistant to chemical attack and thermal shock. TaC, TiB_2, HfC, HfB_2, ZrB_2, ZrC, and TaB_2 are some of the important UHTCs. Density and melting points for some of the important UHTCs are given in Fig.1.

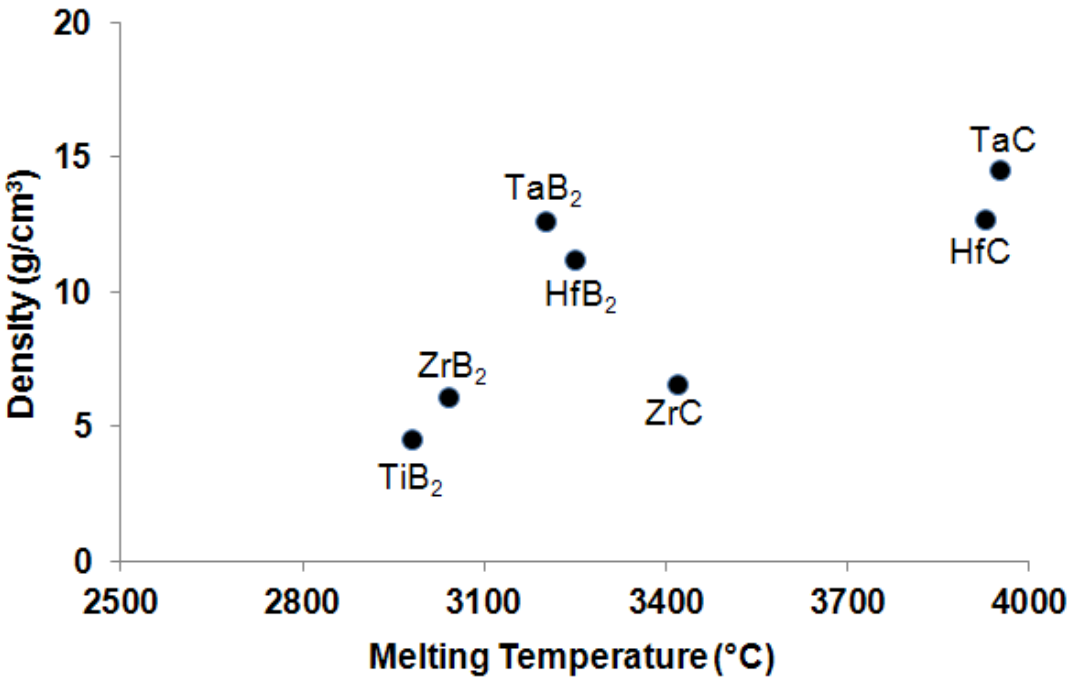

Fig.1 Density and melting points for some of the important UHTCs [4].

Due to these exceptional properties, UHTCs are used in a variety of applications listed below:

1. Leading edge and nose caps components for re-entry and hypersonic vehicles.
2. Rocket nozzles that are exposed to temperatures higher than 2000 °C.
3. Thermal protection systems used in military applications.
4. Coatings for cutting and milling tools to improve shock resistance.
5. Coatings for pump shafts, packing sleeves, and feed screws for the chemical industry.
6. Electrical heaters and electrical igniters.
7. Coatings for molten metal crucibles and fusion – reactor applications [5].

1.3 Reinforcements for UHTCs

Reinforcements are generally added to these UHTCs to obtain better mechanical, thermal and oxidation resistant properties. The most common reinforcements for UHTCs are silicon carbide (SiC) particles and whiskers [6-10], and carbon nanotubes (CNTs) [10-12].

1.3.1 Silicon carbide (SiC) particles and whiskers

Silicon carbide with good oxidation resistance up to 1700 °C and high hardness (32 GPa) is one of the most common reinforcements used in UHTCs. Several investigations reported that SiC as a reinforcement in UHTCs will improve the fracture toughness and strength of the material [13-16]. SiC improves the fracture toughness of the material by toughening mechanisms such as crack deflection and shearing of the reinforcement particles. Another main contribution from SiC as a reinforcement is that it improves the

oxidation resistance of the UHTC by forming layers of glassy SiO_2 on the surface at elevated temperatures [17]. Zhang *et al.* [18] processed SiC whisker-reinforced ZrB_2 ceramics at a temperature of 1750-2000 °C by hot pressing. The investigation revealed that SiC whiskers were not stable in ZrB_2 matrix above 1900 °C and disintegrated into particles. An increase in fracture toughness of ~71% compared to monolithic ZrB_2 for samples sintered at 1800 °C. Whisker bridging, and crack deflection around whiskers were observed as the primary toughening mechanisms. Recently, Yadhukulakrishnan *et al.* [10] processed ZrB_2–SiC composites using SPS. It was reported that addition of SiC improved the relative density from 85% to 99% compared to monolithic ZrB_2. Adding 40 vol.% SiC to ZrB_2 also increased the fracture toughness to 2.32 $MPa.m^{½}$, which is ~65% higher compared to monolithic ZrB_2 processed at similar processing parameters (1900 °C, 70MPa pressure, and 15 min dwell time). Snyder *et al.* [19] wet ball milled ZrB_2-SiC-ZrC powder by using yttria- stabilized zirconia medium and prepared the samples by drying in a rotary evaporator. The attained ZrB_2-SiC-ZrC powder was consolidated at temperature of 1800 °C using SPS. It was reported that a higher percentage of SiC in the composite improved the density, hardness, strength, and thermal conductivity without grain growth.

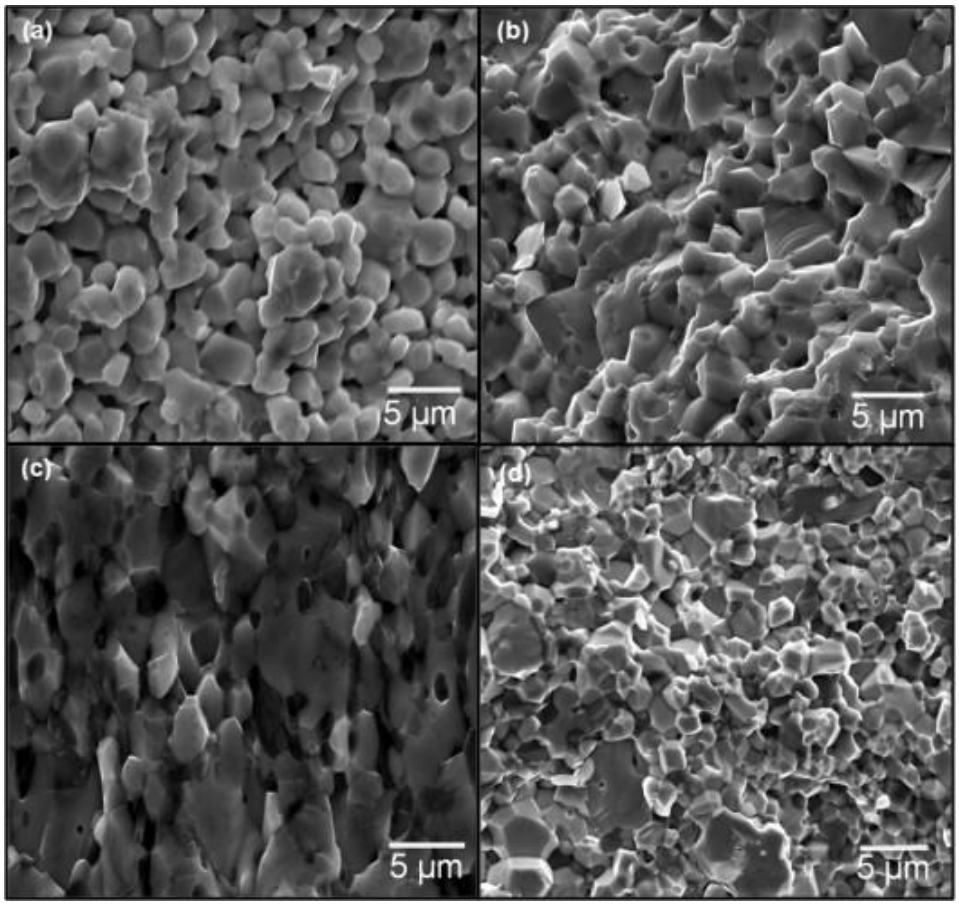

Fig. 2 SEM micrographs showing the fracture surfaces of (a) ZrB_2, and (b-d) ZrB_2 reinforced with 10, 20, and 30 vol.% SiC, respectively [10].

1.3.2 Carbon nanotubes (CNTs)

Carbon nanotubes having tensile strength of 65 GPa, Young's modulus of 1 TPa and thermal conductivity of 3000 W/(mk) [20] are of special interest as nano-scale reinforcements in polymers, metals/alloys, and ceramics [21-26]. Since the discovery of CNTs in 1991, significant efforts have been made to utilize these useful properties in a wide range of applications including electronic, health, defense, and energy applications [27-30]**.** Single-wall carbon nanotubes (SWNTs) as the reinforcement in alumina was reported by Guo-dong *et al.*[31]. They used SPS to sinter SWNT-Al_2O_3 composites at

1150 °C for 3 min. It was reported that the toughness values tripled with addition of 10 vol.% SWNTs to Al_2O_3. Detailed analysis confirmed that SWNTs were strongly entangled with the alumina matrix. Some of the SWNTs were distributed along the grain boundaries, improving the toughness of alumina ceramic composites. In general multi-walled carbon nanotubes (MWNTs) are used as reinforcements in UHTCs due to their excellent mechanical and thermal properties. Jiang *et al.* [32] reported that addition of 5 wt.% MWNTs to TiN, SPS sintered at 703 K resulted in an improvement in thermal conductivity of 97%. Adding MWNTs improved the tribological performance of Si_3N_4 [33]. It was reported that about 40% reduced friction coefficient and ~80% lower wear volumes were attained for the MWNTs reinforced Si_3N_4 when compared to monolithic Si_3N_4. Recently, Yadhukulakrishnan *et al.* [10] reported fracture toughness of 3.53±0.47 $MPa.m^{1/2}$ for 6 vol.% MWNTs reinforced ZrB_2 composites (1.51±0.02 $MPa.m^{1/2}$ for Monolithic ZrB_2) SPS sintered at 1900 °C. It was concluded that the improvement in fracture toughness was due to CNT pull-outs and crack deflection mechanisms.

1.3.3 Graphene nano-platelets (GNPs)

Graphene is a two dimensional sheet in which sp^2 bonded carbon atoms are tightly packed in a hexagonal crystalline structure [34]. A graphene platelet consists of a few layers of graphene sheets. GNPs can be widely employed for applications in field effect transistors, sensors, solar cells, and clean energy devices [35].The research reports related to graphene reinforced materials has increased in recent days due to its extra-ordinary electrical, thermal conductivity and mechanical properties [2, 36, 37]**.** Graphene has been successfully used as reinforcement in several polymer and structural ceramic systems

[38-40], but the details of these works are not discussed here as it is beyond the scope of thesis. Table 1 below shows some of the properties of GNPs.

Table 1 Typical properties of graphene nano-platelets (GNPs) [41].

Property	**Value**
Density	2.2 g/cm^3
Young's modulus	0.5-1 TPa
Tensile strength	130 GPa
Electrical conductivity	~ 20,000 S/cm
Thermal conductivity	~ 5300 W/(mK)
Surface area	~ 2675 m^2/g

Currently, GNPs as reinforcement in ceramics is the subject of great interest in the scientific community. Walker *et al.* [42] used GNPs as the reinforcement in bulk silicon nitride ceramics and sintered the samples at a temperature of 1650 °C and 35 MPa pressure. It was reported that adding 1.5 vol.% of GNPs to Si_3N_4 increased the fracture toughness to ~6.6 MPa.m$^{1/2}$ compared to monolithic Si_3N_4 (~2.8 MPa.m$^{1/2}$) It was also described that GNPs are anchored in the grain boundaries of the matrix and acted as a continuous wall along the grain boundaries that arrested the crack propagation. This mechanism as well as novel toughening mechanisms such as crack bridging, and crack deflection resulted in improving the fracture toughness of GNP reinforced silicon nitride.

To understand the stability of GNPs, Nieto *et al.* [2] consolidated bulk GNP samples at a high temperature of 1850 °C and pressure of 80 MPa by using SPS. They reported that GNPs were able to survive at such high sintering temperatures. Energy dissipation mechanisms such as sliding of platelets and multiple bending at sharp angles were observed, as shown in Fig. 3. The tribological studies confirmed that GNPs provide lubricating effect at higher loads (3N).

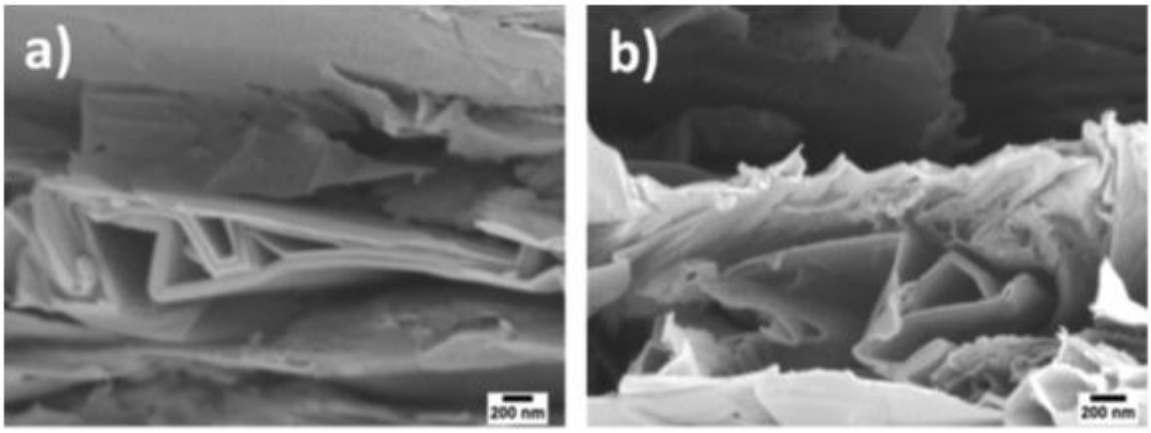

Fig. 3 Energy dissipation mechanisms: (a) bending at sharp angles in multiple stack of GNPs, and (b) bending at sharp angles in single stack of GNP [2].

1.4 Ball milling of UHTCs

High energy ball milling of UHTCs is generally performed to reduce the starting particle size or for uniform dispersion of reinforcement into the matrix. During the ball milling process, the powder particles are repeatedly flattened, fractured and welded. It was reported by Suryanarayana *et al.* [43] that when two balls collide during ball milling, some amount of powder is trapped between them and the force of impact plastically deforms the powder particles eventually leading to fracture. It was also reported that the

efficiency of particle size reduction during ball milling is very low and only 0.1% of reduction in size can be achieved. It was also reported by Beatriz *et al.* [44] that ball milling has the ability to influence the kinetics of sintering. A review on the effect of ball milling parameters on mechanical properties of UHTCs will be discussed below.

Galan *et al*. [45] performed high energy ball milling of ZrB_2 powder to observe the effect of milling time and ball-to-powder ratio on the particle size. They performed ball milling for the times in the range of 3-180 min. with ball-to-powder ratios of 2 and 4. It was reported that particle size refinement occurred through brittle fracture. The size of particles decreased rapidly during the initial times then gradually, and finally reached an asymptotic limit where the particle size does not show any dependence on the milling time. As shown in Fig. 4, the particle size reduced rapidly to below 100 nm in about 10 min. of ball milling, however not much variation in grain size is attained with ball milling time of 25 min. to 180 min. It was also reported that if the ball-to-powder ratio is higher, the reduction in particle size will be faster and smaller particle size can be achieved ultimately (Fig. 4).

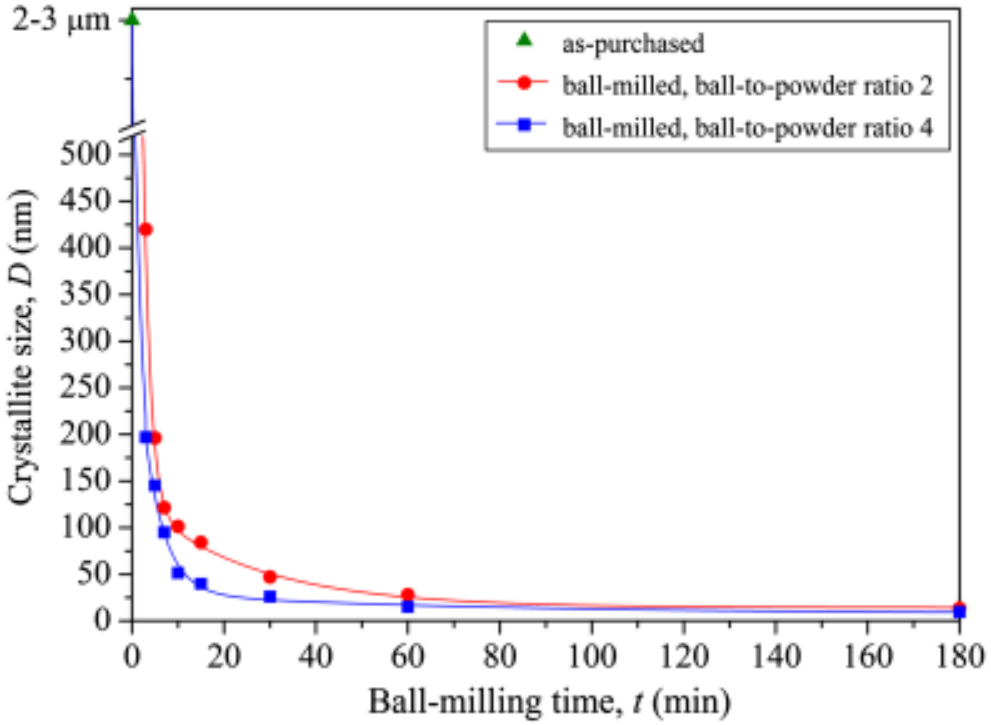

Fig. 4 Effect of ball milling time and ball-to-powder ratio on the particle size of ZrB_2 [45].

Kim *et al*. [46] consolidated ball milled TaC powder using high-frequency induction heated sintering process. TaC powder was ball milled at a speed of 250 rpm for 1, 4, and 10 h with ball-to-powder ratio of 30:1 and mechanical properties of sintered samples was investigated. It was reported that high hardness of 22 GPa and fracture toughness of 5.1±0.3 $MPa.m^{1/2}$ were achieved for 10 h ball milled sample due to fine refinement of grains. It was also reported that particle size decreased from 935 nm to 33 nm with 10 h of ball milling. Figure 5 below shows the SEM images of TaC powders ball milled. It can be observed that fine crystallite size was attained with increase in ball milling time.

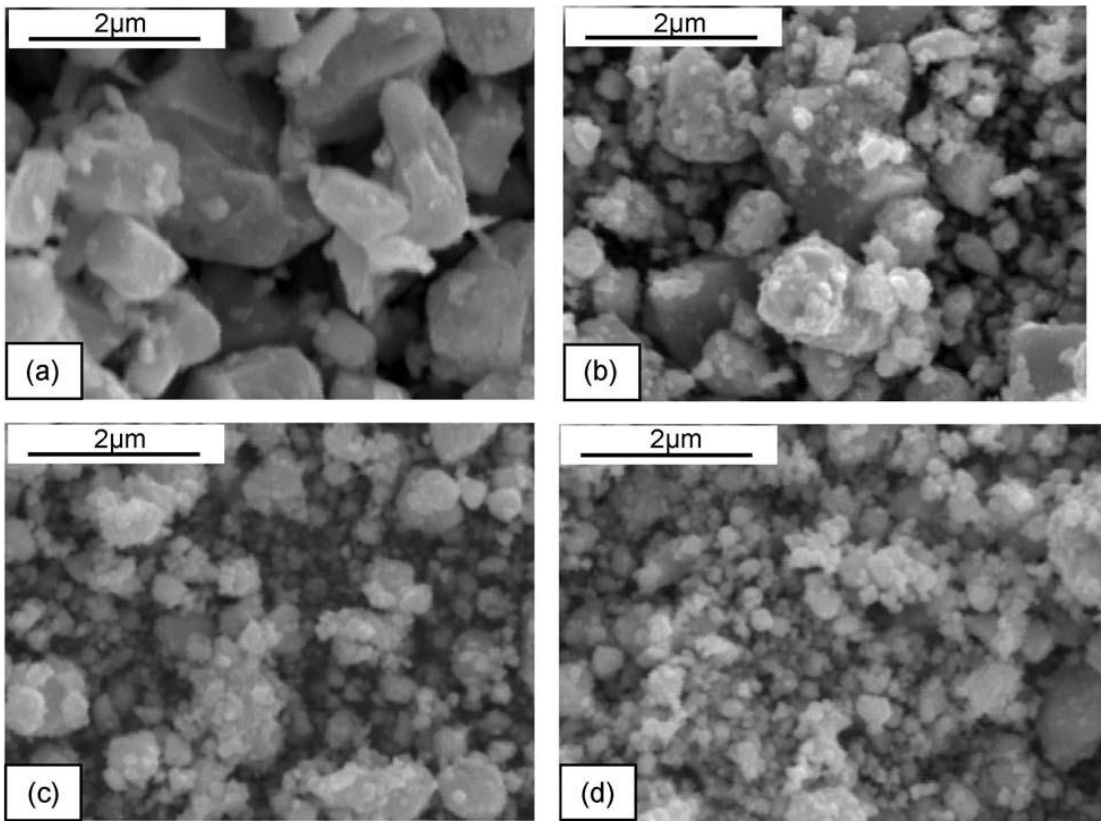

Fig. 5 SEM micrographs of TaC powder ball milled for (a) 0, (b) 1, (c) 4, and (d) 10 h [46].

Beatriz *et al*.[44] performed wet ball milling of ZrC powder at different times with ball-to-powder ratio of 4 and consolidated with SPS. It was reported that the crystallite refinement occurred with increase in ball milling time and resulted in improving the SPS kinetics of ZrC. The formation of agglomerates improved the green density of the compact resulting in final density at lower sintering temperatures and times.

Ball milling was also performed in several investigations [7, 47, 48] to achieve good dispersion of reinforcement into the matrix. Kim *et al*. [48] performed high energy ball milling for 10 h at a speed of 62 rpm with ball-to-powder ratio of 16:1 for achieving good

dispersion of SiO_2 into the ZnS. The attained ball milled powder was processed using SPS at temperature of 1200 °C with a pressure of 90 MPa for 5 min. It was reported that ball milling resulted in attaining the denser samples. The improvement in fracture toughness and hardness were also observed due to the dispersion hardening and crack deflection mechanisms induced by fine SiO_2 phase.

1.5 Tantalum carbide (TaC): structure, properties, and applications

Tantalum is a transition metal of the fifth group and is considered as a refractory metal. The carbides formed by this group elements are very important due to their exceptional properties such as high melting points, high hardness, and good chemical inertness. Most of the transition metal carbides have closed-packed or nearly closed-packed atomic arrangements in which smaller carbon atoms are placed into interstitial sites [49]. The structure of transition metal carbides can be determined from Hagg rules [50]**.** According to Hagg rules, if the radius ratio $r=r_C/r_M$, where r_C is the radius of nonmetal atom and r_M is the radius of transition metal atom, is less than 0.59 the compound formed should then have a simple structure. Table 2 below shows the radius ratios for transition metal carbides.

Table 2 Radius ratios (*r*) for the transition metal carbides [50].

	Group IV	**Group V**	**Group VI**
4th Period	Ti-C 0.526	V-C 0.576	Cr-C 0.609
5th Period	Zr-C 0.483	Nb-C 0.530	Mo-C 0.556
6th Period	Hf-C 0.486	**Ta-C 0.529**	W-C 0.553

It can be observed from Table 2 that, except for chromium (Cr), all other metal carbides have radius ratio of less than 0.59 indicating that metal atoms in carbides often form simple fcc, hcp, or simple hexagonal lattices. The crystal structure of TaC compound, where all the octahedral interstitial sites are occupied by carbon in the fcc lattice, is shown in Fig. 6. Such an arrangement leads to cubic (NaCl) crystal structure.

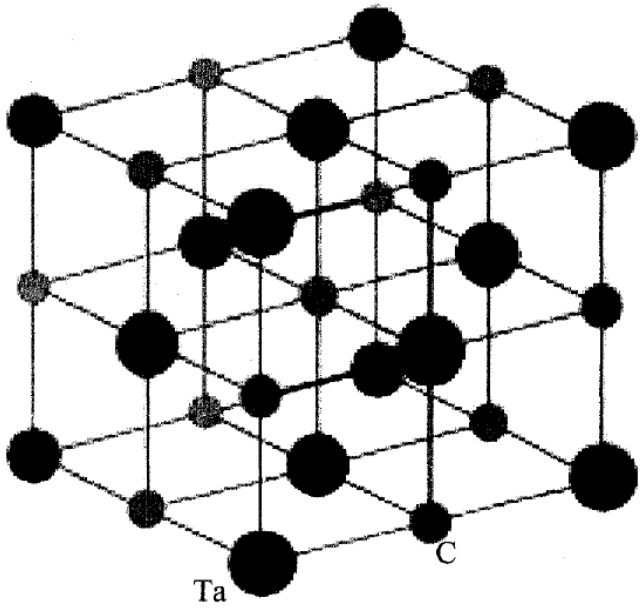

Fig. 6 Crystal structure of TaC [51].

While tantalum forms TaC and Ta_2C with carbon atoms, only the mono carbide phase (TaC) is of industrial importance. The properties of TaC are summarized in Table 3 below.

Table 3 Properties of tantalum carbide [50].

Property	Value
Density (solid)	14.5 g/cm^3
Thermal conductivity	22.1 W/m.°C at 20 °C
Electrical resistivity	25 μΩ.cm
Melting point	3950 °C
Vickers hardness	16.7 GPa
Shear modulus	214 GPa
Modulus of elasticity	285-560 GPa
Bulk modulus	414 GPa
Transverse rupture strength	350-400 MPa

Due to such exceptional properties as mentioned above, TaC is produced industrially in appreciable quantity. A summary of applications of TaC is given below:

1. Leading edge and nose caps components for re-entry and hypersonic vehicles.
2. Rocket nozzles that are exposed to temperatures higher than 2000 °C.
3. Coatings for WC-Co cutting tools to improve cutting characteristics, shock resistance, high- temperature hardness, wear, and oxidation resistance.
4. Electrical heaters and electrical igniters.
5. Coatings for molten metal crucibles and fusion–reactor applications.
6. Automotive wear resistant liners.

1.6 Processing of UHTCs

The production of UHTC powders in industrial scale has been the matter of attraction in the recent times due to its numerous applications. TaC is usually produced by carbo-thermal reduction of Ta_2O_5 with carbon. This method has been used industrially due to low cost of raw materials. TaC can also be synthesized by gas phase reaction of $TaCl_5$ with hydrocarbons, and polymeric precursors derived from tantalum alkoxides [52]. The powder synthesized from these processes has low specific area and can be used in applications such as cutting tools that require wear and shock resistance. However, the electrochemistry applications such as oxidation resistant coatings, electrodes, and conducting films require the material to possess higher surface areas. TaC powders with high surface areas have been developed recently from gel-derived precursors and liquid precursors in which a mixture of tantalum ethylate and carbon nano powders are used [53]. The powdered form of TaC developed from the above discussed processes can be used as starting powder and consolidated into bulk form using hot pressing, pressureless sintering, reactive hot pressing, vacuum plasma spray technique, spark plasma sintering, and high frequency induction heating sintering etc. This section reviews some of these processing approaches for UHTCs. The studies on processing of TaC composites using these approaches will also be discussed in detail in the review section on reinforced TaC composites.

1.6.1 Hot pressing

Hot pressing is a process that involves application of heat and uniaxial pressure to compact different ceramics to full density with controlled microstructure. Researchers

have widely used the hot pressing to process TaC and other ultra-high temperature ceramics.

Monteverde *et al.* [54] hot pressed ZrB_2-SiC based UHTCs and carried out electrical discharge machining (EDM) for designing nose-cap prototypes. Hot pressing was carried out at a temperature of 1500 °C. The fracture toughness and flexure strength were measured at room temperature and at 1500 °C to understand the durability of composite at high temperatures. A decrease in fracture toughness from 4.1 $MPa.m^{1/2}$ to 2.6 $MPa.m^{1/2}$ and flexure strength from 900 MPa to 250 MPa was reported with increasing temperatures from room temperature to 1500 °C. They also assessed the EDM machinability of UHTC blocks into complex shapes by and concluded that machined surface with roughness less than 1 μm can be attained. Figure 7 shows the ZrB_2-SiC UHTC block that was machined in the form of nose-cone by EDM technique.

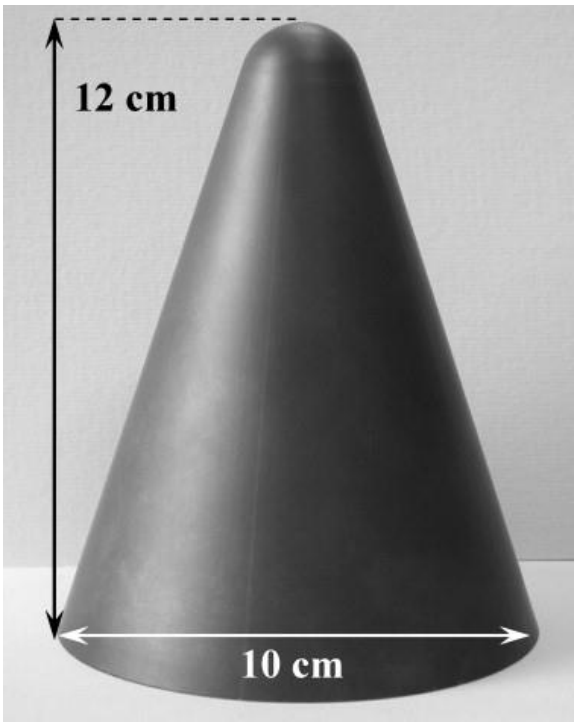

Fig. 7 Hot pressed ZrB_2-SiC block machined in the form of nose-cone using EDM technique [54].

Diletta *et al*. [55] processed HfB_2–15 vol.% $MoSi_2$ composites using hot pressing at 1900 °C. It was reported that 99% dense composite can be formed with decrease in grain size from 10 μm (monolithic HfB_2) to 1.5 μm (HfB_2–15 vol.% $MoSi_2$ composite). A new phase HfO_2 was formed during the sintering, as shown in Fig. 8. It was also concluded that $MoSi_2$ acts as a suitable sintering additive for densification of HfB_2. Flexure strength was performed at room temperature and at 1500 °C. It was observed that composites exhibit high strength values (548±20 MPa) due to high refractoriness of the phases present.

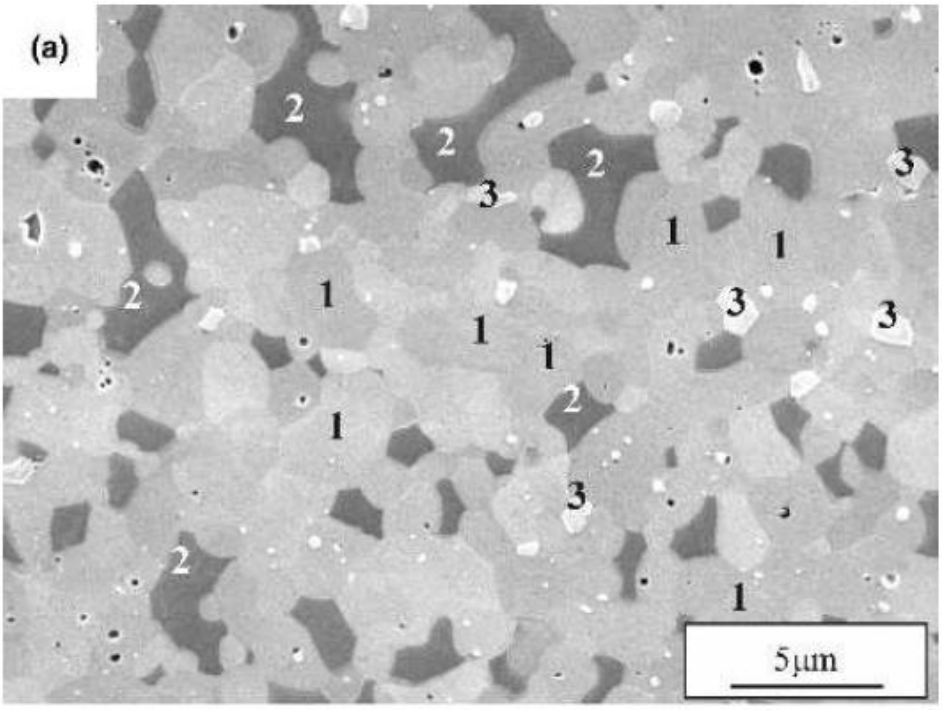

Fig. 8 SEM micrograph from the polished surface of hot pressed HfB_2-$MoSi_2$ composite showing HfB_2, $MoSi_2$, and HfO_2 phases indicated as 1,2, and 3, respectively [55].

A comparison between the conventional hot pressing and SPS was done by Balbo *et al.* [56]. They sintered ZrB_2–15 vol.% $MoSi_2$ composites at similar sintering conditions of 1750 °C and 30 MPa with a heating rate of 100–150 K/min and observed no major differences in microstructural features and mechanical properties. Figure 9 below shows the micrographs of sintered ZrB_2–15 vol.% $MoSi_2$ by using the hot pressing and SPS processes.

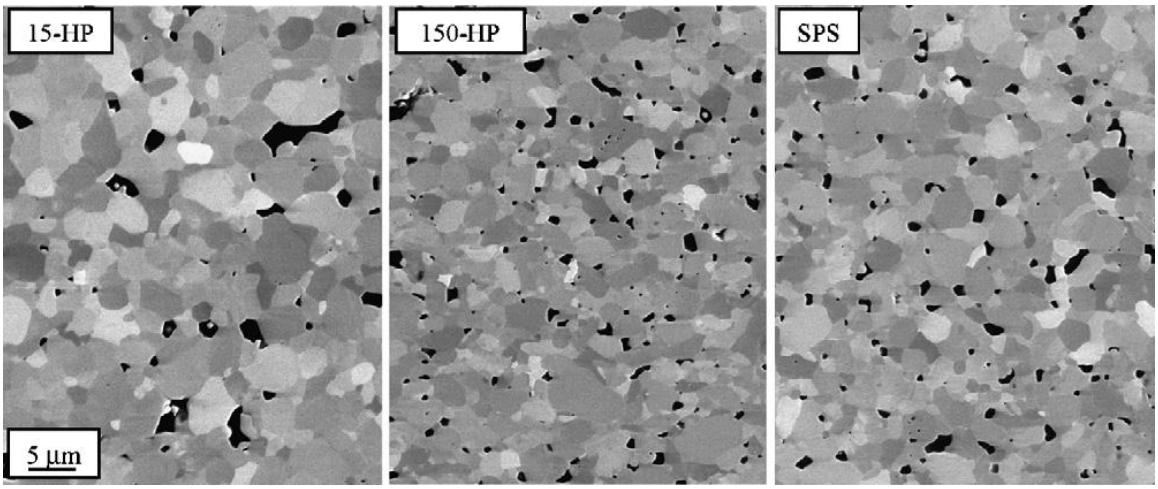

Fig. 9 SEM micrograph from hot pressed and SPS sintered ZrB_2-15 vol.% $MoSi_2$ samples showing SiO_2 pockets (dark regions) [56].

1.6.2 Pressureless sintering

Pressureless sintering is another novel process employed to fabricate UHTCs at high temperatures. This process involves high temperatures without any applied pressure. The density variations in the final compact can be avoided by using this process.

Recently, Talmy *et al.* [57] processed multi-phase ceramics using pressureless sintering at 1700 °C to 1900 °C. TaC and B_4C mixture were used to prepare TaC-TaB_2-C system. The mixtures were first cold pressed in a steel mold at 100 MPa, and then cold isostatic pressing was employed at 300 MPa. The pressureless sintering of obtained samples for 2 h improved the density and hardness compared to pure TaC. It was also concluded that the grain growth of TaC was suppressed due to the presence of TaB_2. Figure 10 shows the SEM images of TaC-TaB_2-C ceramics prepared by pressureless sintering. It can be observed from the Fig. 10 that the grain size increases with decreasing

TaB_2 and C content. The microstructure was also uniform with trans-granular form of fracture. The presence of C can be easily identified in ceramics sintered with $TaC:B_4C$ ratio of 4:1.

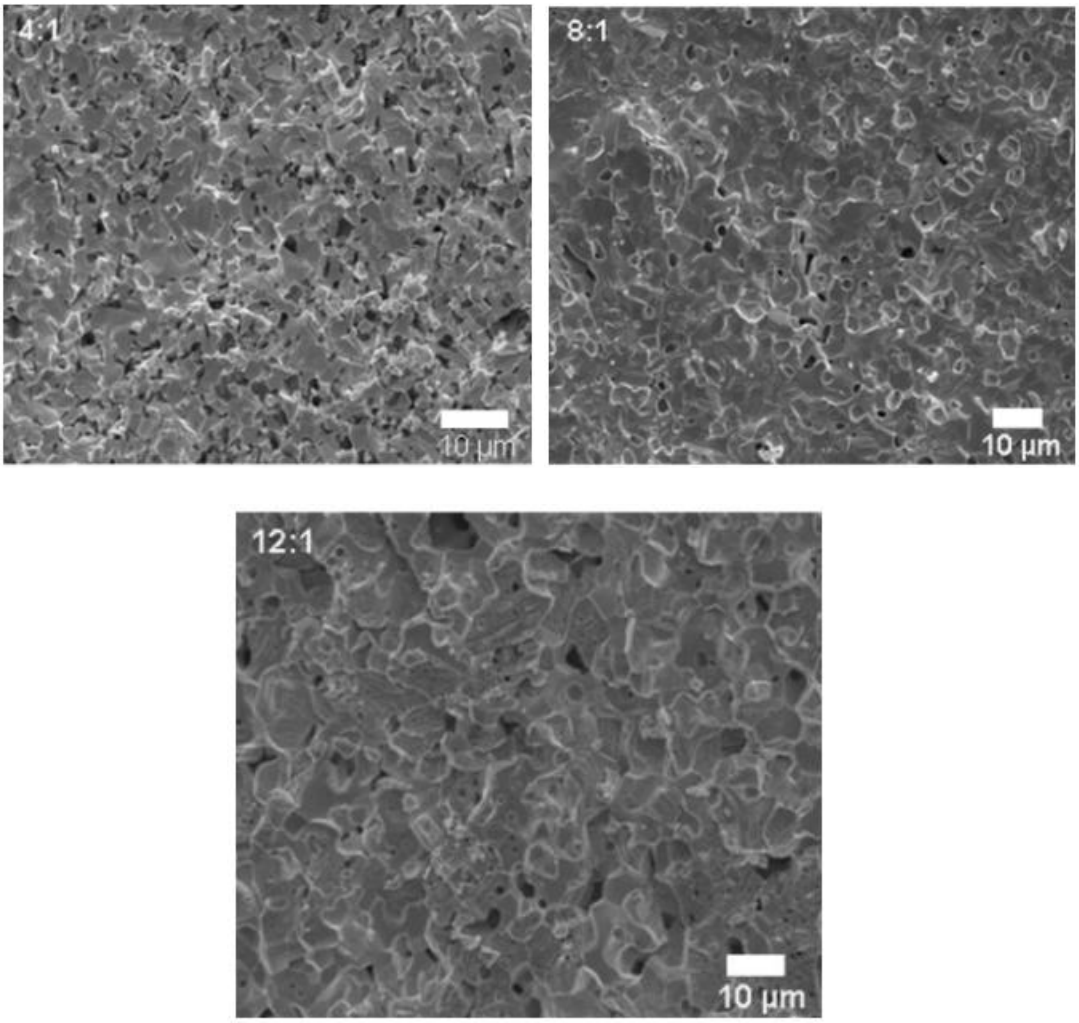

Fig. 10 SEM micrographs from $TaC\text{-}TaB_2\text{-}C$ ceramics pressureless sintered using different $TaC:B_4C$ ratios (4:1, 8:1, and 12:1) [57].

Zhang *et al.* and Yan *et al.* [8, 58] reported the fabrication of ZrB2-SiC composites using ball milling and pressureless sintering. While Zhang *et al.* used Mo as a

sintering aid, Yan *et al.* used B_4C and C as the sintering aids. They reported nearly full density of the samples by using the pressureless sintering process. A solid solution formed by Mo with ZrB_2 was also reported by Zhang *et al.* (Fig 11). B_4C addition by Yan *et al.* resulted in good dispersion of SiC particles in ZrB_2 matrix without formation of any new phases. Significant improvements in fracture toughness, flexure strength, and elastic modulus were reported by both studies.

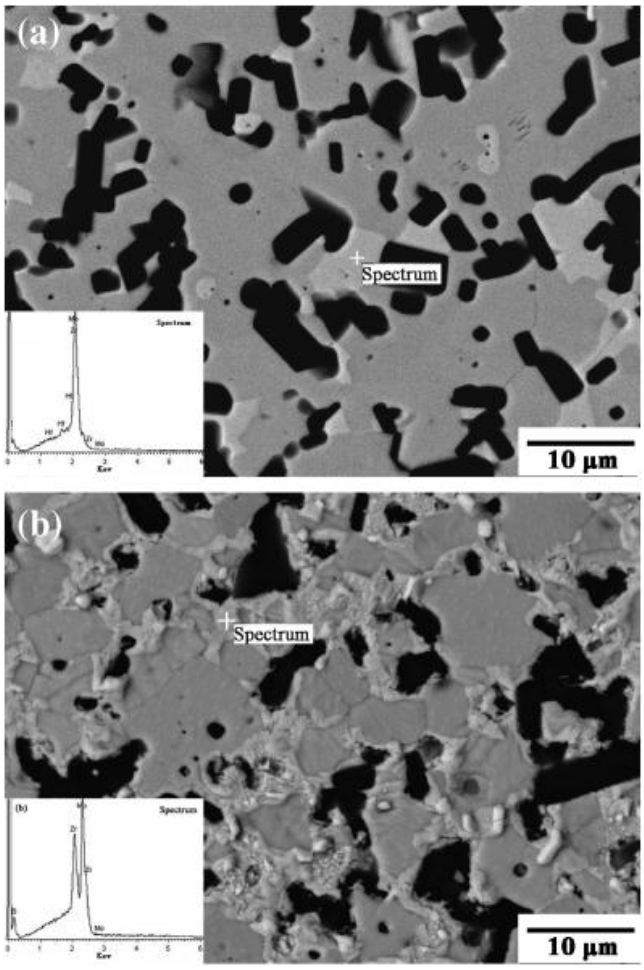

Fig. 11 EDS analysis showing the SiC (dark area), ZrB_2 (dark grey area), and Zr-B-Mo solid phase (gray area) in the ZrB_2-SiC composites pressureless sintered at 2250 °C for 2 h [58].

1.6.3 Reactive hot pressing

In reactive hot pressing, material phases react under pressure at high temperature to form high density ceramics. This process is an alternative method used to process UHTCs. The process is almost similar to hot pressing, with the exception of starting reactive powders used in reactive hot pressing.

Monteverde *et al.* [59] used reactive hot pressing for the processing of HfB_2–SiC composite. The in-situ reaction between starting Hf/Si/B_4C taken in the molar ratio of 2.2/0.8/1 converted the constituents into HfB_2 and SiC ceramics. The obtained ceramics were hot pressed at 1450 °C for 60 min. It was reported that the reactive hot pressed sample consists of HfB_2, SiC, and HfO_2 phases, as shown in Fig. 12. It was also reported that SiC phase acted as an inhibitor and also improved the oxidation resistance of the sample. The microhardness of 19 GPa, Young's modulus of 520 GPa, and flexure strength of 315±10 MPa were reported.

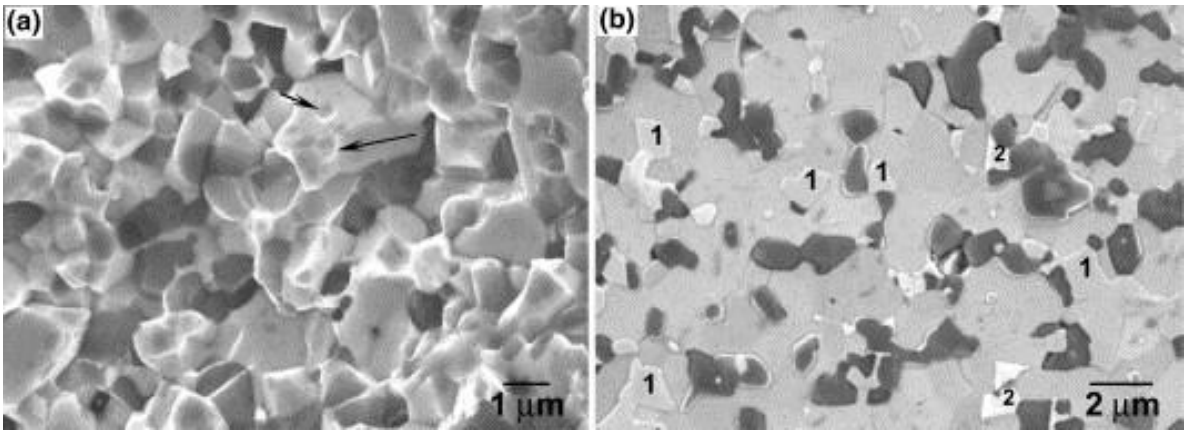

Fig. 12 SEM micrographs from reactive hot pressed HfB_2-SiC composites showing (a) SiC particles on the HfB_2 grains on fractured surface, and (b) HfC and HfO_2 grains indicated as 1 and 2, respectively, on the polished surface [59].

Rangaraj *et al.* [9] produced ZrB_2- SiC composites by reactive hot pressing using Zr, B_4C, C, and Si as the starting powders. The reactive hot pressing was carried out at 1600 °C, 40 MPa for 60 min. It was reported that ZrC phase attributes to densification of the composite. In the same study, it was reported that addition of nickel (to promote densification) does not improve the densification.

1.6.4 Spark plasma sintering (SPS)

Spark plasma sintering (SPS) is one of the most recent sintering processes that involve pulsed direct current and uniaxial pressure. Detailed discussion of the process is presented in the section 1.7.

1.6.5 Plasma spray deposition

While densification and near-net shaping of UHTCs can be achieved through conventional processes discussed above, the applications such as propulsion liners for space shuttles and thermal protective coatings require the fabricated component to be thin walled, contoured structure, or coatings. An alternative process developed to overcome the difficulty is a plasma spray deposition. The plasma spray deposition is one of the thermal spray deposition process in which partially melted material is deposited on the surface of the material. Current is applied to heat the material in the coating precursor and the melted material is deposited on the surface to be coated.

Balani *et al.* [60] fabricated freestanding TaC structure using vacuum plasma spray (VPS) technique. Figure 13 shows the TaC cylinder deposited by VPS technique.

They reported that the generated microstructure showed the anisotropic behavior due to the partial transformation of phases and incomplete formation of grain boundaries. Hardness values of 21.25±2.69 GPa (axial direction), 26.90±9.42 GPa (transverse direction) and fracture toughness of 3.46±0.79 $MPa.m^{1/2}$ (axial direction), 3.41±0.92 $MPa.m^{1/2}$ (transverse direction) were reported.

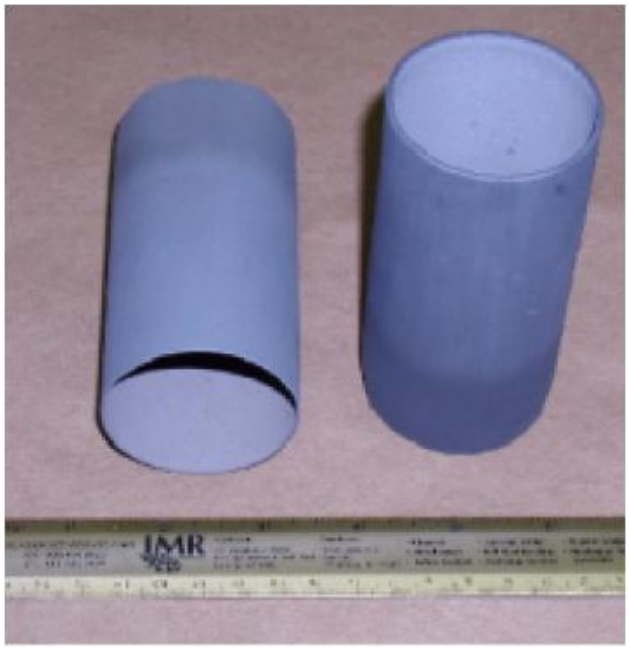

Fig. 13 TaC cylinders (50 mm in diameter, 100 mm in height, and 1.5 mm in thickness) deposited by vacuum plasma spray technique [60].

Tului *et al.* [61] fabricated the ZrB_2-SiC composite by plasma spray deposition. 25 wt.% SiC powder was blended with ZrB_2 by using the spray drying technique, and the powder was sprayed onto a flat graphite substrate. After studying the thermal and mechanical behavior and conducting the plasma wind tunnel test, Tului *et al.* reported

that UHTC plasma sprayed coatings can be able to withstand high temperature oxidizing conditions. Figure 14 shows the plasma spray deposited ZrB_2-SiC composite undergoing the plasma wind tunnel test.

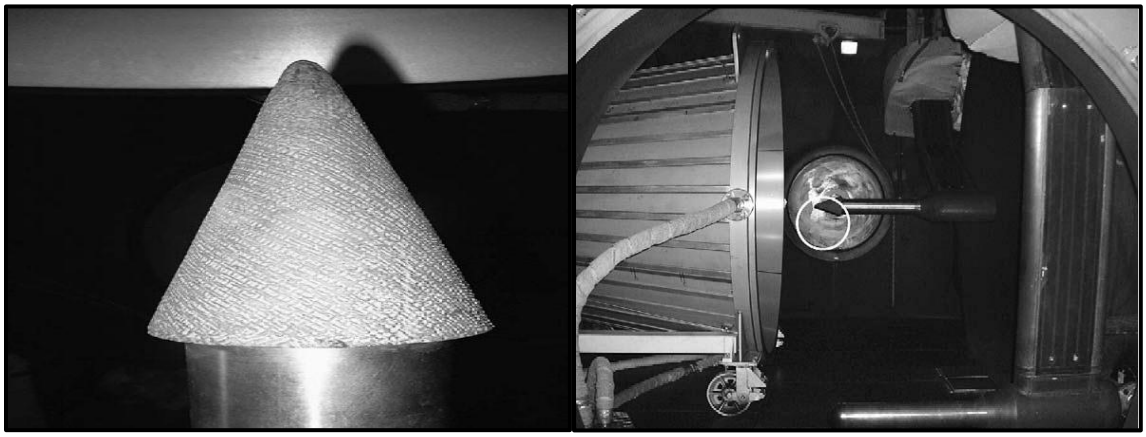

Fig. 14 Plasma spray deposited ZrB_2-SiC composite undergoing plasma wind tunnel test (image on the right), the shape of the ZrB_2-SiC composite (test article) is showed at the center of white circle and in the left side image [61].

1.7 Spark plasma sintering (SPS)

SPS is a novel technique that involves simultaneous application of pulsed direct current and uniaxial pressure to consolidate the materials. As shown in Fig. 15 [62], the powder to be sintered (sample) is placed in between the graphite die and punches which are electrically conductive, and the uniaxial pressure (P), and pulsed direct current are applied simultaneously. Apart from joule heating, pulsed direct current produces other effects such as increase in diffusion rate, removal of oxides and other impurities from the surface that leads to better densification. Presence of spark/discharge during SPS is debatable and under investigation.

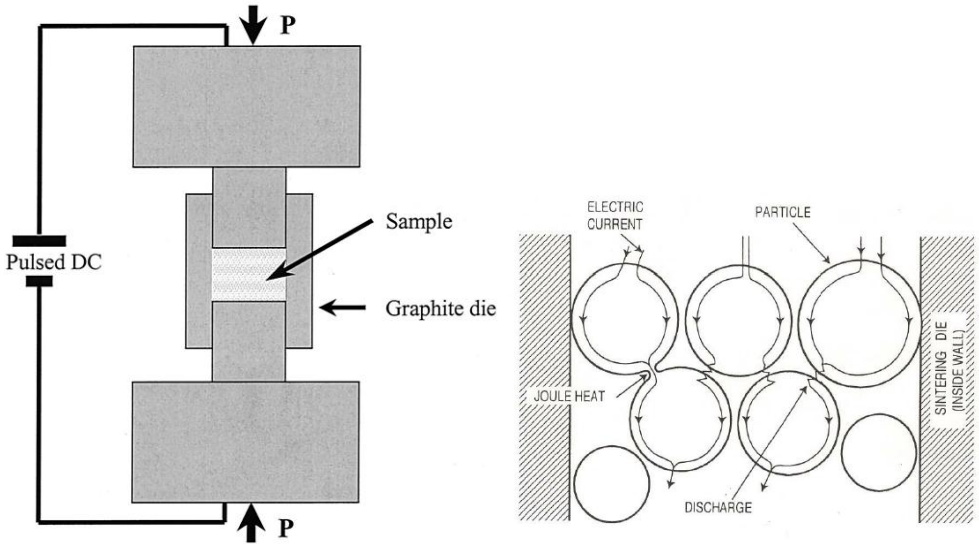

Fig. 15 A schematic showing spark plasma sintering set up and mechanisms of sintering [62, 63].

Due to unique features of the process, such as high heating and cooling rates (up to 1000K/min), very short holding times (minutes), SPS process has been used to fabricate a variety of materials. Figure 16 shows the typical examples of various materials that can be sintered using SPS process.

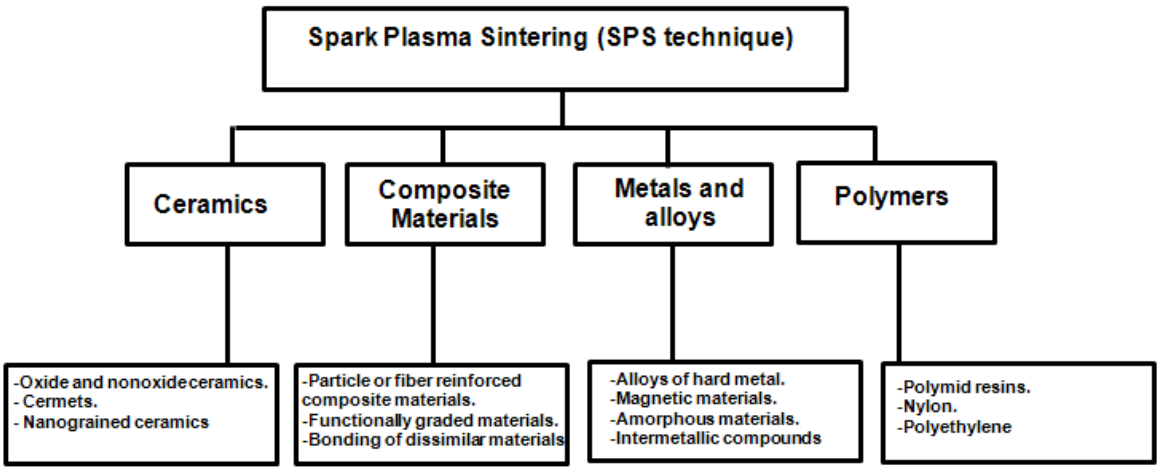

Fig. 16 Flow chart showing examples of various materials that can be processed using SPS process [64, 65].

Past works by several researchers [66, 67] concluded that fully dense materials can be attained by using SPS process. Improvement in mechanical and electrical properties along with dense microstructure is mainly observed. Increase in oxidation and corrosion resistance has also been reported.

1.7.1 Effect of SPS processing parameters on densification

The six important user-defined parameters of the SPS experiment are shown in Fig. 17. Of all the parameters the effect of heating rate, temperature, pressure and current are considered to be dominant in densification of materials. This section reviews the effect of these parameters on densification and microstructural behavior of the sintered samples.

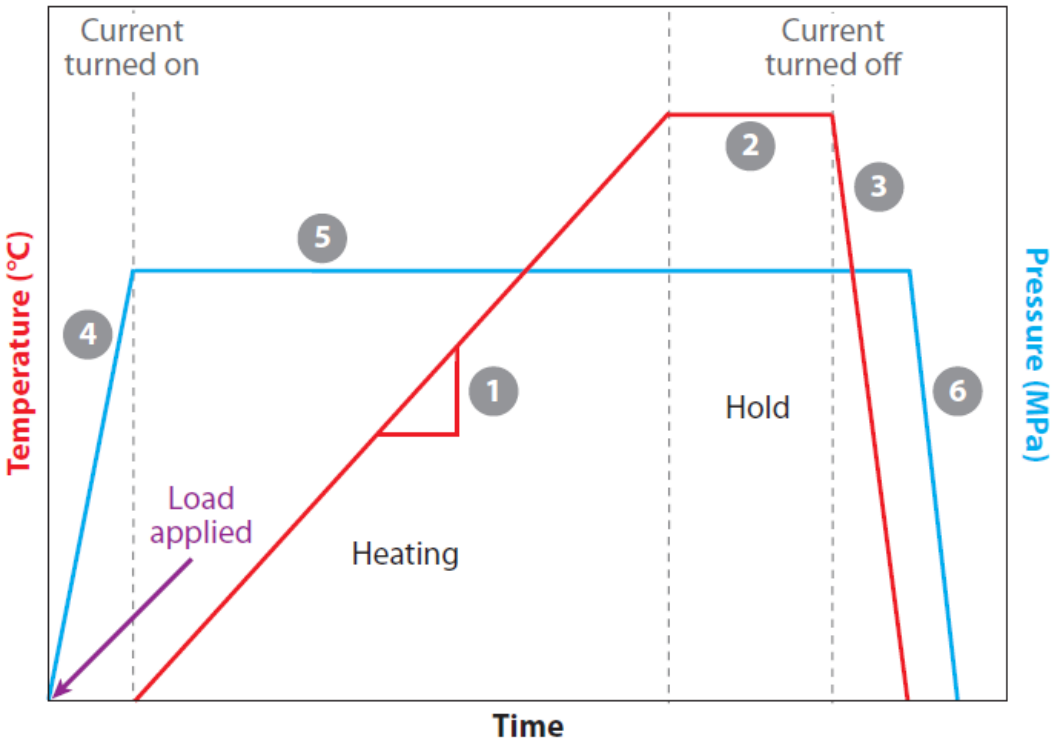

Fig. 17 Six important user defined parameters for SPS sintering: (1) heating rate, (2) maximum (hold) temperature, (3) cooling rate, (4) load application rate, (5) maximum load hold, and (6) load removal rate [62].

1.7.1.1 Heating rate

Heating rate is one of the most important parameters that differentiate SPS from conventional hot pressing process. Investigations on the effect of heating rate by various researchers on different materials concluded that lower heating rates (50-300 °C/min) did not affect the final density, whereas if the higher heating rates (up to 600 °C/min) were applied the final density decreased. Chen *et al.* [68] explained that this observation was mainly due to large thermal gradients prevailing with the high heating rates that cause the sample to sinter from outside, but there was considerable porosity inside. It was also

concluded that with increase in heating rates (50-300 °C/min) the grain size decreased [69]. Figure 18 below shows the effect of heating rate on density and grain size of Al_2O_3 samples sintered at 1300 °C and 1400 °C. It can be observed that both grain size and temperature decreased with increase in heating rate after 300 °C/min.

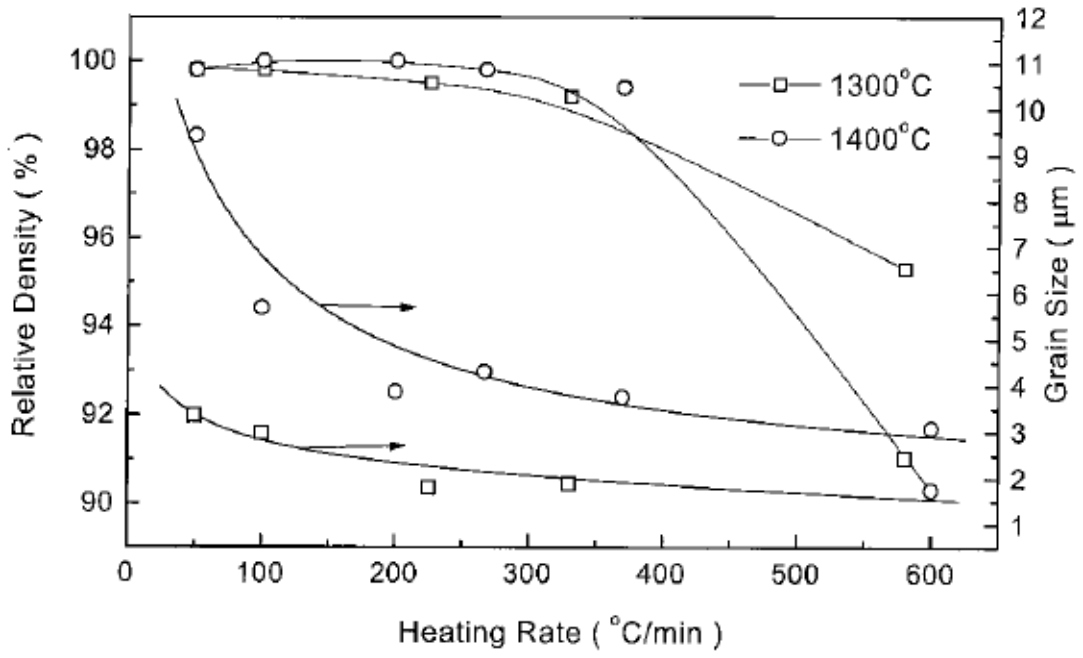

Fig. 18 Effect of heating rate on density and grain size of Al_2O_3 samples sintered at 1300 °C and 1400 °C [70].

1.7.1.2 Temperature

Sintering temperature plays an important role in powder densification. During SPS process, the heat required for increasing the temperature comes from the flowing current in the form of joule heat with a heat generation rate (Q). The heat generation rate is given by the equation,

$$Q = JE \quad \text{..... (1.1)}$$

where, J is the current density, and E is the electrical field.

Garay *et al.* [62] conducted the experiments on various metals, oxides and ceramics and concluded that with increase in temperature the density tends to increase. He also induced a linear curve fit to understand the relationship between density and temperature and gave the equation as

$$\rho = s\left(\frac{T}{T_m}\right) + b \quad \text{..... (1.2)}$$

where ρ is relative density, s is slope or temperature sensitivity, T is processing temperature, T_m is the melting point, and b is the intercept on density axis.

Table 4 shows the values of temperature sensitivity for various materials given by Garay *et al.* [62]**.** It can be observed that the temperature sensitivity for ceramics is higher compared to metals, which conclude that densification in ceramics, is mainly dependent on temperature whereas for metals densification is dependent on plastic deformation and current effects such as electro migration.

Table 4 Temperature sensitivity (*s*) for various ceramics and metals [62].

Material	**Temperature sensitivity** (*s*)
Ceramics	
Al_2O_3	2.3
ZrO_2 (8 mol% Y_2O_3)	3
MgO	2.1
TiO_2	3.1
SiC	1.7
Metals	
Al	0.6
Ta	0.9
Cu	0.6

1.7.1.3 Pressure

Higher pressure applied at a particular temperature helps in attaining a higher density sample and better sintering of the powder. Applied pressure has two types of effects on sintering. First, it helps in rearrangement of powder particles and breaking of agglomerates. This effect is termed as mechanical effect, and second, is the intrinsic effect in which it adds to driving force for sintering [69, 71]. The equation below shows the intrinsic effect of pressure

$$\frac{d\rho}{(1-\rho)dt} = B\left(g\frac{\gamma}{x} + P\right) \quad \text{..... (1.3)}$$

where ρ = Fractional density

B = term that contains diffusion coefficient and temperature

g = geometric constant

γ = surface energy

x = particle size scale

t = time

P = applied external pressure

The intrinsic effect of pressure mainly relies on the particle size (related to γ) of the powder. If the particle size is small, the relative contribution of pressure in sintering is small and vice versa.

1.7.1.4 Current

The applied pulsed DC current plays two important roles in SPS. First, is to provide heat and second is to create plasma. The plasma will cause the cleansing effect on the surface and helps in sintering enhancement by reducing the oxide layer on the powder. Researchers used various routes such as theoretical analysis [72], studies on effect of DC pulsing on various properties of sintered materials [73], numerical modeling [74] to understand the mechanisms. However, these mechanisms related to generation of plasma by applying pulsed DC current are still under debate and no further conclusions were drawn from the mechanisms that are already proposed.

1.8 Reinforced TaC composites: A review

To improve the properties of TaC, researchers conducted various experiments and added different reinforcements in the TaC matrix. Literature suggests that CNTs and ceramics are the main reinforcements added to TaC. This section mainly deals with the reinforced TaC composites and various processes used to develop these TaC composites.

1.8.1 CNT reinforced TaC composites

CNTs are relatively new reinforcements used in TaC composites when compared to ceramic reinforcements. SPS is the only process used to fabricate CNT reinforced TaC composites. In 2010, Khaleghi *et al.* [11] added 0.77 wt.% CNT to TaC using SPS and sintered at 2300 °C and 30 MPa. The investigation revealed that adding CNTs increased density from 92% to 96% with an improvement in rupture strength from 336 MPa to 550 MPa. They also concluded that CNTs also act as a sintering aid and helps as grain growth inhibitor. Recently Bakshi *et al.* [12] fabricated TaC–4 wt.% CNT composites using SPS at a temperature of 1850 °C and at three different pressures of 100, 255, and 363 MPa. The authors used both long length (10-20 μm) and short length (1-3 μm) CNTs and dispersed them in TaC matrix by using wet chemistry, and spray drying techniques respectively. The experimental results concluded that spray drying was the better dispersion technique compared to wet chemistry and sintering at lower pressures (100 MPa) was better for improving the characteristics of CNT added TaC composites. They also observed that longer CNTs acts as better reinforcements compared to shorter CNTs

as they showed better densification. Table 5 shows the hardness, elastic modulus, and density values attained for TaC-CNT composites SPS sintered at 1850 °C and 100 MPa.

Table 5 Hardness, elastic modulus, and density of TaC–CNT composites SPS sintered at 1850 °C and 100 MPa [12].

CNT content (wt.%)	**Relative density** (%)	**Hardness** (GPa)	**Elastic modulus** (GPa)
0	89	17.8±3.2	335±28
4.0 (Long CNTs)	95	22.9±2.1	395±17
4.0 (Short CNTs)	94	17.5±2.4	331±47

The damage of CNTs at higher pressures (255 and 363 MPa) was also observed and it was reported that CNTs converted to flaky graphitic structure as shown in Fig. 19. Figure 20 shows the fracture surface of TaC–4 wt.% CNT samples sintered at a pressure of 100 MPa and 1850 °C in which good dispersion of CNTs was observed as reported by Bakshi *et al.* [12]**.**

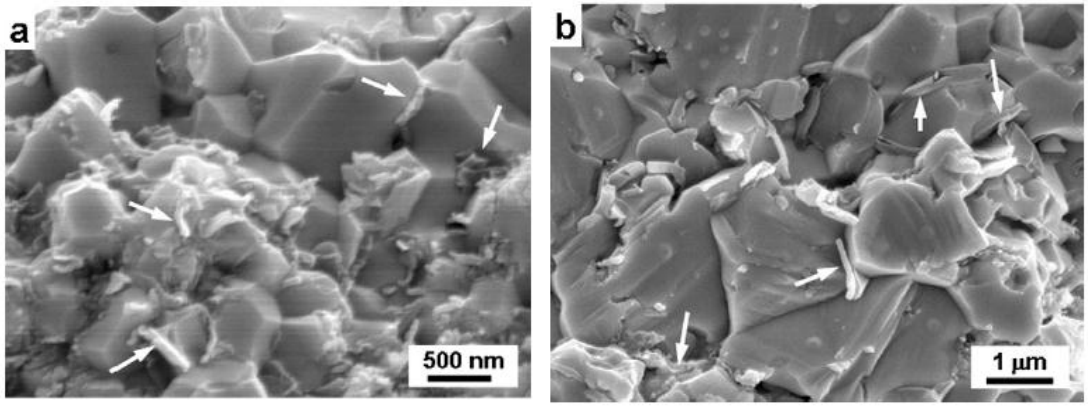

Fig. 19 SEM micrographs showing damaged CNTs in (a) TaC–long length CNT, and (b) TaC–short length CNT composites sintered at 1850 °C and 363 MPa [12].

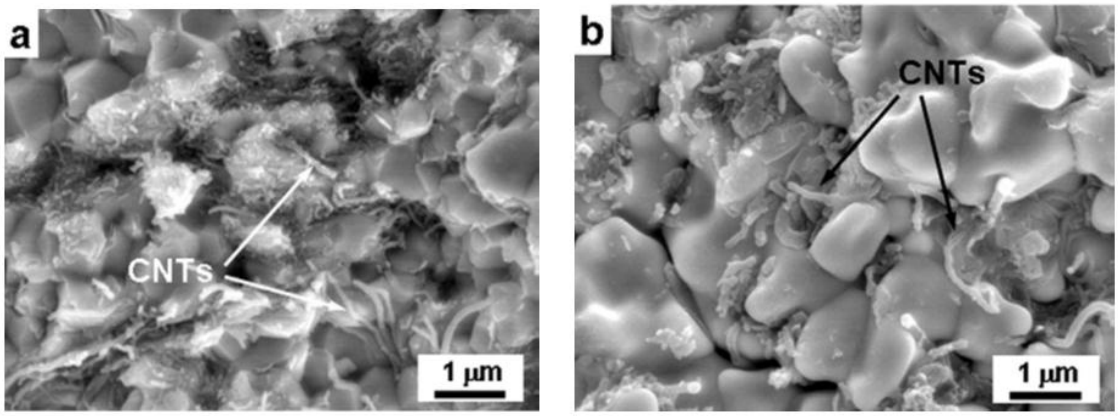

Fig. 20 SEM micrographs showing CNTs in fracture surface of (a)TaC-long length CNT, and (b) TaC-short length CNT samples sintered at 1850 °C and 100 MPa [12].

1.8.2 Ceramic reinforced TaC composites

Different particles such as SiC, B_4C, and TaB_2 were investigated as reinforcements for TaC. It was reported that reinforcing TaC with various ceramic particles improved the density of material by inhibiting the grain growth along with increase in hardness, elastic modulus, and fracture toughness of the composites.

Liu *et al.* [6] fabricated the ball milled TaC/SiC composites by SPS process at 1800 °C for 5 min. They reported that addition of SiC particles (40 vol.%) to TaC increased the fracture toughness and flexure strength to 6.8 $MPa.m^{1/2}$, and 703 MPa, respectively. It was reported that due to the thermal expansion mismatch between TaC (6.3×10^{-6} /K) and SiC (4.3×10^{-6} /K), thermal residual stresses were developed near the SiC particle localities. These developed thermal residual stresses favored the interfacial debonding and crack deflection which resulted in improving the strength of material. It was also reported that SiC particles assisted in attaining the fully dense samples by eliminating the closed porosities and decreased the grain size of TaC.

Liu *et al.* [47] used TaC, B_4C, and Ta as the starting powders to spark plasma sinter TaC/TaB_2 composites. They reported that TaB_2 phase was formed at around 1580 °C and resulted in improving the density of final sample. They also observed that 11 wt.% TaB_2 in TaC matrix improved the hardness from 13.2 to 23.9 GPa and fracture toughness from 2.8 to 4.5 $MPa.m^{1/2}$.

Zhang *et al.* [1] added 0.36 wt.% B_4C to TaC and compared the results to pure TaC and 0.43 wt.% B_4C+0.13 wt.% C added TaC samples. They hot pressed all the samples at temperatures ranging from 1900 °C to 2400 °C and concluded that addition of

B_4C improved the final density of the sample and resulted in attaining the full density at comparatively lower temperatures. They also reported that large variation in grain growth was observed for B_4C (9 µm) and B_4C+C (12.2 µm) added samples compared to pure TaC (1.3 µm) hot pressed at same temperature of 2200 °C. Addition of higher amounts of B_4C (1 and 2 wt.%) to TaC resulted in formation of TaB_2 and C phases for hot pressed samples at 2100 °C as reported by Zhang *et al.* [75]**.** They also concluded that relative density increased from 94 to 98% and hardness improved from 14 to 16 GPa due to formation of TaB_2. A decrease in Young's modulus was observed due to presence of carbon. Figure 21 below shows the microstructure of 0.36 wt.% B_4C and 2 wt.% B_4C added TaC composites.

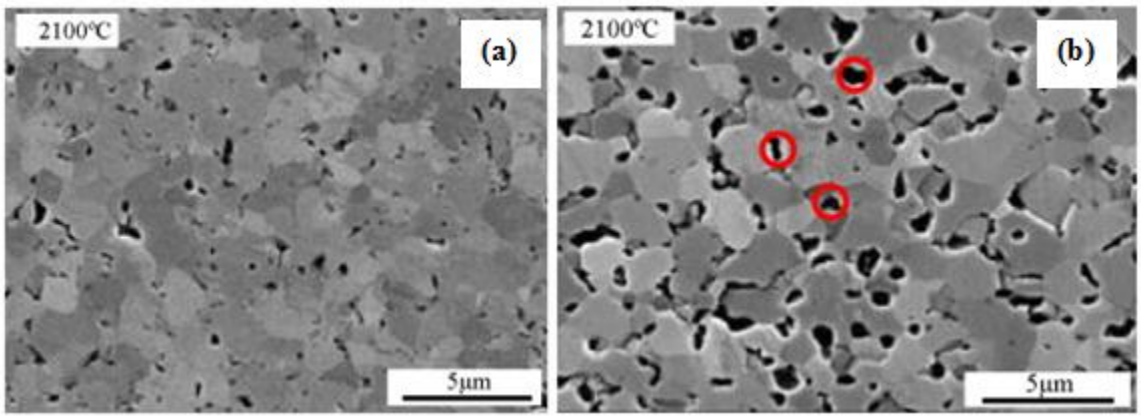

Fig. 21 Microstructure of (a) TaC+0.36 wt.% B_4C composite, and (b) TaC+2 wt.% B_4C composites hot pressed at 2100 °C [75].

Bakshi *et al*. [76] fabricated TaC–1wt.% B_4C powder and pure TaC powder using SPS at 1850 °C and three different pressures of 100, 255, and 363 MPa. They reported that at higher pressures, fully dense TaC samples were obtained with increase in TaC

grain size. Addition of B_4C increased the relative density at lower pressure (100 MPa) from 89% to 97% and aided in resisting the grain growth even at pressure of 363 MPa. It was observed that TaB_2/C formed at grain boundaries helped in pinning grain boundary and inhibiting grain growth. Figure 22 below shows the TaB_2/C phase formed at grain boundaries (a) and carbon flakes present in between TaC grains (b). A 93% improvement in relative fracture toughness due to B_4C addition was also reported.

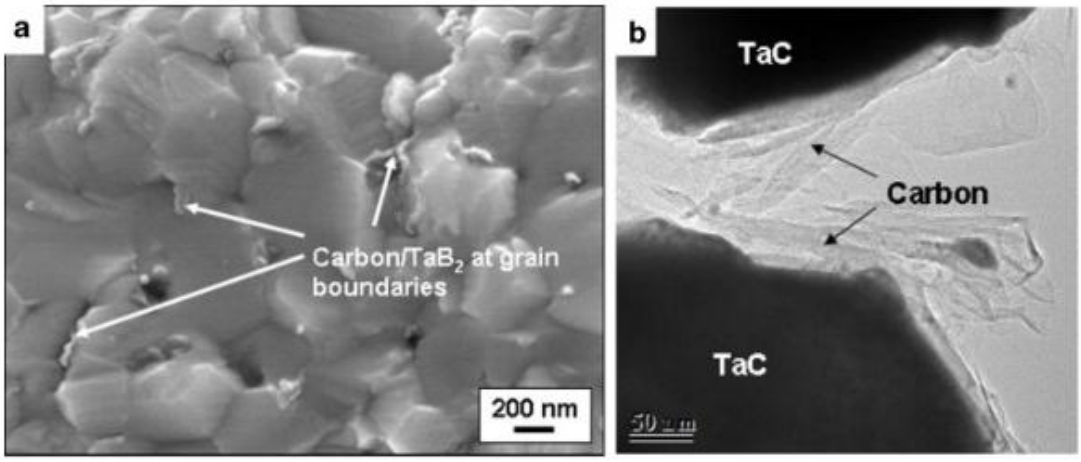

Fig. 22 (a) SEM micrograph showing TaB_2/C phase at TaC grain boundaries in $TaC+B_4C$ sample sintered at 363 MPa, and (b) TEM image showing carbon flakes between TaC grains in $TaC+B_4C$ sample sintered at 363 MPa [76].

1.9 Densification of TaC

Tantalum carbide (TaC), due to its strong covalent bonding and low-self diffusion coefficients show poor sinterability without external pressure [77]**.** Previous studies by various researchers [78-80] confirmed that dominant mechanism of densification for pressure activated sintering is power-law creep. Rahaman *et al.* [81] established an analytical model for power-law creep to predict the sintering mechanism during SPS and hot pressing. The equation below describes the densification rate during pressure activated sintering processes such as hot pressing, hot isostatic pressing, and SPS [82].

$$\frac{d\varepsilon}{dt} = \frac{1}{\rho}\frac{d\rho}{dt} = A\frac{D\mu b}{KT}\left(\frac{b}{G}\right)^{m}\left(\frac{\sigma}{\mu}\right)^{n} \quad \text{..... (1.4)}$$

where $\frac{d\varepsilon}{dt}$ is the creep rate, ρ is the instantaneous relative density, A is a constant, D the diffusion coefficient, μ the instantaneous shear modulus, G the grain size, σ instantaneous effective stress applied to power bed, T is absolute temperature, b the burgers vector, and m and n are exponents characteristic of the mechanism of creep or densification.

The research on the study of densification mechanisms during sintering of TaC was initiated in the 1980's. Shvab *et al.* [83] sintered TaC samples at temperatures of 2400 °C–2700 °C in hydrogen atmosphere without applying any pressure and concluded that high temperatures and longer holding times improved the grain growth which subsequently restricted the densification. They also calculated the activation energy for grain growth during pressureless sintering and reported the value to be 380 kJ/mol. Kislyi *et al.* [84] densified TaC compacts using pressureless sintering of TaC powder as the starting material. A density of 89% was attained even after using a sub-micron size

particle of 0.17 μm at a temperature of 2700 ℃. They also concluded that fine powders (<7-8 μm) of TaC started densification at temperatures above 1400 °C by diffusion-viscous flow mechanism and reported that activated grain boundary sliding mechanism was responsible for densification during initial stage of sintering, where as volume self-diffusion mechanism was observed during long holding periods.

Recently, hot pressing and SPS were employed to densify TaC powders. Additives such as B_4C, SiC, and CNTs were added to improve the density of TaC. Zhang *et al.* [75] investigated B_4C reinforced TaC and achieved a relative density of >98% by using hot pressing at a temperature of 2100 °C. Bakshi *et al.* [12, 76] processed TaC+CNT, TaC+B_4C composites using SPS at a temperature of 1850 °C and attained relative densities of 94% (TaC+CNT) and 97% (TaC+B_4C) by applying a pressure of 100 MPa. Even though the experiments were performed for the improvement of density using additives and employing pressure activated sintering, no attempts were made to study the theoretical densification mechanisms during SPS of TaC powders.

Gendre *et al*. [82] studied the densification mechanisms active during the SPS of $ZrC_{0.94}O_{0.05}$ powders. They sintered the samples at three different pressures of 25, 50, and 100 MPa by applying a constant temperature of 1750 °C. An analytical model derived from creep deformation studies of ceramics was used to determine the densification mechanisms and activation energy of 700 kJ/mol was obtained. Inter-granular glide mechanism was found to be responsible for densification at lower pressure (25 MPa), and dislocation motion mechanism operates at higher pressures (100 MPa).

Densification mechanism active during SPS of calcium oxide and titanium dioxide doped alumina (codoped α-alumina) material was proposed by Bernard *et al.* [85]. The analysis of the sintering mechanism was done for three different soaking temperatures of 1050, 1100, and 1150 °C by varying the soaking time between 5 to 15 min. A significant increase in grain size was reported with increase in sintering temperature. The calculated values of the stress exponent (*n*) and grain size exponent (*m*) were reported as 1, and 3, respectively with activation energy of 250 kJ/mol. From the attained values, it was proposed that grain boundary sliding, accommodated by oxygen-grain boundary diffusion was the active densification mechanism during SPS of codoped α-alumina material.

The activation energy in turn mainly depends upon "*n*" and "*m*" values. A variety of models were developed to investigate the high temperature creep behavior for ceramic poly crystals by calculating *m* and *n* values, and finding the character of activation energy ("bulk" or "grain boundary"). Such models can be transferred to SPS problem by considering power-law creep rate equation. Table 6 below shows the different densification mechanisms that were proposed for different cases and various m and n values.

Table 6 Densification mechanisms proposed for different stress exponent (*n*) and grain size exponent (*m*) values [85].

Case no.	Value of n & m	Densification mechanisms	Activation energy character
Case 1. If grain boundaries are perfect sources/sinks of vacancies	n=1 & m=2	grain boundary sliding accommodated by volume diffusion.	bulk
	n=1& m=3	grain boundary sliding accommodated by grain boundary diffusion.	grain boundary
Case 2. If grain boundaries are not perfect sources/sinks of vacancies	n=2 & m=1	grain boundary sliding accommodated by an in-series (interface-reaction/lattice diffusion) mechanism controlled by interface-reaction shape.	bulk
	n=2 & m=2	grain boundary sliding accommodated by an in-series (interface-reaction/grain boundary diffusion) mechanism controlled by interface-reaction shape.	grain boundary
Case 3. If the dislocations source density is independent on the effective stress	n=4.5 & m=0	dislocation climb controlled mechanism.	bulk
Case 4. If the dislocations source density depends on the effective stress	n=3 & m=0	dislocation climb controlled mechanism.	bulk

1.10 Objective

The objective of the present work is to investigate spark plasma sintering, densification mechanisms, and microstructure-properties relationships for

- Monolithic TaC.
- TaC ball milled for 30 min. and 60 min.
- TaC–GNP composite with reinforcements of 2, 4, and 6 vol.% GNP.

CHAPTER 2

EXPERIMENTAL DETAILS

2.1 Materials

In the current study, TaC powder that is 99.7% pure with an average particle size of <3 μm and multi walled graphene platelets (GNPs) of 30 μm in diameter and 25 nm in thickness were used as starting powders. Table 7 below shows the details of materials used in the current study.

Table 7 Specifications of materials used in this study.

Material	**Density** (g/cm^3)	**Average size**	**Supplier**
Tantalum carbide (TaC)	13.9	<3 μm	Inframat Advanced Materials
Graphene nano-platelets (GNPs)	2.1	30 μm (in diameter) 25 nm(in thickness)	American Elements

2.2 Experimental procedure

2.2.1 Powder preparation

For the first study, as-received TaC was ball milled for 30 min. and 60 min. at a speed of 750 rpm. The ball-to-powder ratio was taken as 5:1. Ball milling was also performed for uniform dispersion of GNPs into TaC. Both TaC and GNPs were placed in 125 ml tungsten mixing jar and tungsten balls of 10 mm diameter were added and ball milling was performed at speed of 300 rpm for 30 min. for dispersion of GNPs. Wet milling was executed by adding 10 ml of acetone and 0.1% of poly acrylic acid (PAA). The objective of adding acetone was to prevent the material from sticking to the balls and walls of the jar, whereas PAA was used as a dispersive agent. 2, 4, and 6 vol.% of GNPs were added to TaC and the main aim was to achieve good dispersion of GNPs in TaC. As-received TaC was also ball milled at 300 rpm to confirm that improvement in mechanical properties is due to addition of GNPs. Figure 23 below shows the high energy ball milling equipment used for mixing the powder.

Fig. 23 High energy ball mill used for mixing powders in the OSU laboratory.

2.2.2 Fabrication of samples

SPS was the manufacturing process used to fabricate all the samples. SPS machine (model SPS 10-3) used was manufactured by Thermal Technologies LLC and it has the capability of attaining high heating rates such as 600 °C/min. Figure 24 shows the different components of SPS equipment used for current study. The SPS equipment mainly consists of three components: power unit, heating furnace, and vacuum pump. As all samples were sintered at high temperatures of 1700 °C–2100 °C, liquid argon gas was used to attain high cooling rates and a high vacuum of 0.002 to 0.003 Torr was maintained for attaining purest samples. Graphite dies and punches were used to fabricate samples and die temperatures were measured by K type and C type thermocouples.

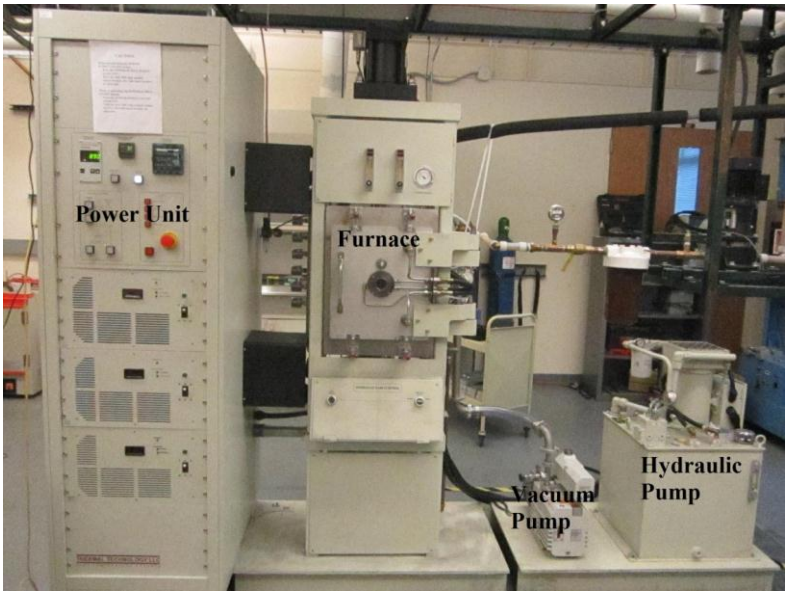

Fig. 24 Spark plasma sintering equipment in the OSU laboratory showing different components.

Since TaC is an UHTC with melting point of 3880 °C, sintering should be performed relatively at high temperatures. In SPS, the final sample is achieved by placing material in between punches and dies and processing at required temperature and pressure (as shown in Fig. 25). The material and design of the punches and dies depends upon the temperature and pressure to be achieved. Due to its high thermal and electrical conductivity, graphite is used for making punches and dies for SPS. In the present study, graphite dies and punches are used to sinter TaC composites at a constant pressure of 70 MPa.

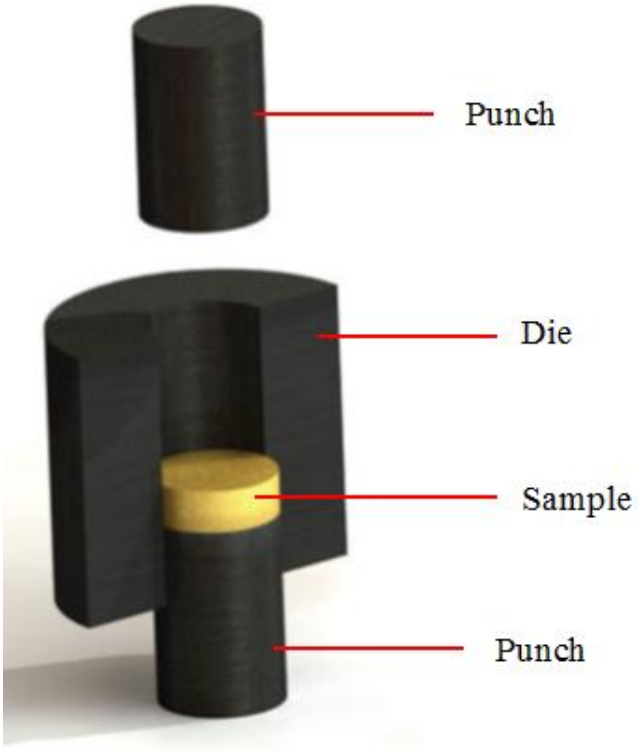

Fig. 25 Schematic of the punches, die, and sample assembly used for SPS sintering [47].

2.3 Characterization and testing methods

SPS sintered TaC composites were polished using SiC paper of 400 grit to remove the graphite foil attached on all the surfaces. Diamond plate was used to level the samples and then was grinded with SiC paper until 1200 grit. A fine polished surface was attained to observe the metallographic features and for undertaking micro indentation. Alumina powder of 0.05 µm and diamond polisher of 0.01 µm were used to attain the polished surface.

2.3.1 Density measurement

Density of samples was measured using Archimedes principle with distilled water as immersion medium. The theoretical density of TaC-GNP composite was calculated from the rule of mixtures in which true density of TaC was taken to be 13.9 g/cm^3 and GNP to be 2.1 g/cm^3 respectively. The relative density of each sample is calculated using the following equation

$$percentage\ of\ densification = \frac{density\ of\ sintered\ sample}{theoretical\ density\ of\ powder} \times 100 \ldots\ldots. (2.1)$$

Figure 26 below shows the apparatus (Mettler Toledo-Delta Range XD204) used to measure the weight and density of the sintered sample.

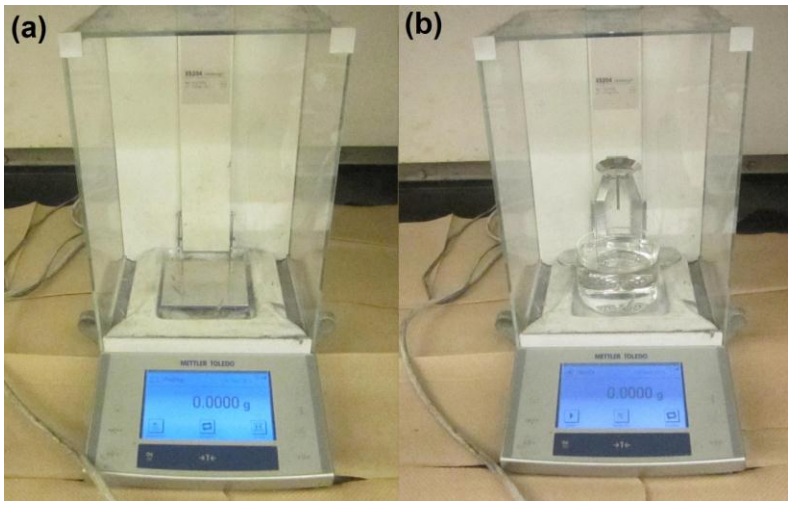

Fig. 26 Equipment for density measurement.

2.3.2 Microstructure and phase analysis

The x-ray diffraction analysis of the monolithic TaC, ball milled TaC and TaC–GNP composite samples was carried out using Philips Norelco X-ray diffractometer (as shown in Fig. 27(a)) operating with Cu Kα (λ=1.54178 Å) radiation at 45 kV and 40 mA. The diffraction angle (2θ) was varied between 20° and 90° at a step increment of 0.02° 2θ with a count time of 1 s. The characterization of the microstructure was conducted using a scanning electron microscope (JSM-6360, JOEL) shown in Fig. 27(b). Raman spectroscopy was also conducted on the fractured surface of the TaC-GNP composites using WITec alpha300 R Raman system at a laser power of 0.8 mW with a spot size of 20 μm and laser excitation of 532 nm. Raman spectra were acquired for SPS processed monolithic TaC, TaC-GNP composites, ball milled TaC-GNP powder and pristine GNP in the frequency range of 1200–3000 cm^{-1}. The structural quality and the presence of GNPs in the ball milled powder and sintered samples were investigated.

Fig. 27 (a) X-ray diffractometer, and (b) Scanning electron microscope for phase and microstructural characterization.

2.3.3 Mechanical testing

2.3.3.1 Microhardness

Hardness of the samples was measured by using a microhardness tester developed by Clarke Inc. as shown in Fig. 28. Indentations were taken at a load of 1000 g and holding time of 15 s. The microhardness was measured from indentations taken on the polished surface of the sample. Around forty readings were taken for each sample at different locations and an average value was reported.

Fig. 28 Microhardness tester.

2.3.3.2 Fracture toughness

Fracture toughness was measured on the polished surface using a microhardness tester (Tukon Inc.) displayed in Fig. 29. All the indentations were taken at a load of 5 kg with a holding time of 15 s. Fracture toughness (K_{IC}) was calculated using the Anstis equation [86].

$$K_{IC} = 0.016 \left(\frac{E}{H}\right)^{\frac{1}{2}} \frac{P}{c^{3/2}} \quad \text{(2.2)}$$

Where E is the elastic modulus (285 GPa for TaC), H is the hardness, P is the load applied (1000 g) and c is the crack length measured from center of the indents.

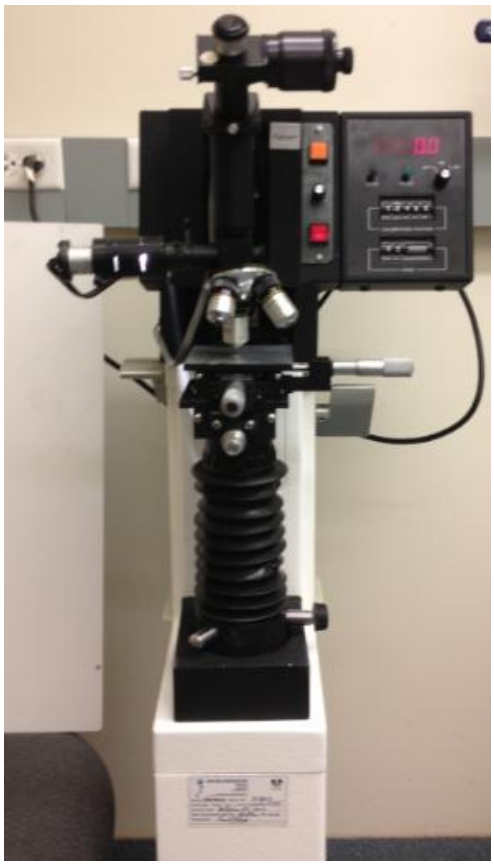

Fig. 29 Microhardness tester used for indentations at higher loads.

2.3.3.3 Flexure strength

Flexure strength of the monolithic TaC, ball milled TaC and TaC–GNP composite samples was measured using ring-on-ring (RoR) biaxial flexure testing method. The discs were loaded in RoR fixture using a table-top test frame (Instron 5567, Instron Corporation, USA). Controlled loading rate of 0.5 mm/min was applied and peak load at failure was recorded. A minimum 3 tests were performed for each kind of sample and average value along with standard deviation was reported. The flexure strength was calculated from the peak load at failure as per the equation given below [87]**.**

$$\sigma_{RoR} = \frac{3P}{2\pi t^2}\left(\frac{(1-\nu)(a^2-r^2)}{2R^2} + (1+\nu)\ln\frac{a}{r}\right) \quad \text{(2.3)}$$

where,

P is the applied load (N)

v is the Poisson's ratio

a is the radius of the support ring (m)

r is the radius of the load ring (m)

R and *t* are the radius and thickness (m) of the sample.

CHAPTER 3

RESULTS AND DISCUSSION

3.1 Effect of ball milling time on spark plasma sintering of TaC

In this investigation, monolithic TaC powder was ball milled for 30 min. and 60 min. at a speed of 750 rpm. Ball-to-powder ratio was taken as 5:1 and the ball milled powder was compared with as-received TaC powder. The effect of ball milling time on the mechanical properties of the SPS sintered TaC was studied.

3.1.1 Microstructure of ball milled TaC

Microstructure of the as-received TaC powder was shown in Fig. 30(a). It can be observed that the grains are angular in shape with uniform grain size. SEM images of the ball milled powder were presented in Fig. 30 (b) and (c). From Fig. 30, it is evident that agglomerates are formed for both the time intervals and the volume of agglomerates increased with an increase in ball milling time. The shape of TaC powder also became round with ball milling. The grain size measurement from SEM images of as-received and ball milled TaC powders confirmed decrease in particle size with increase in ball milling time.

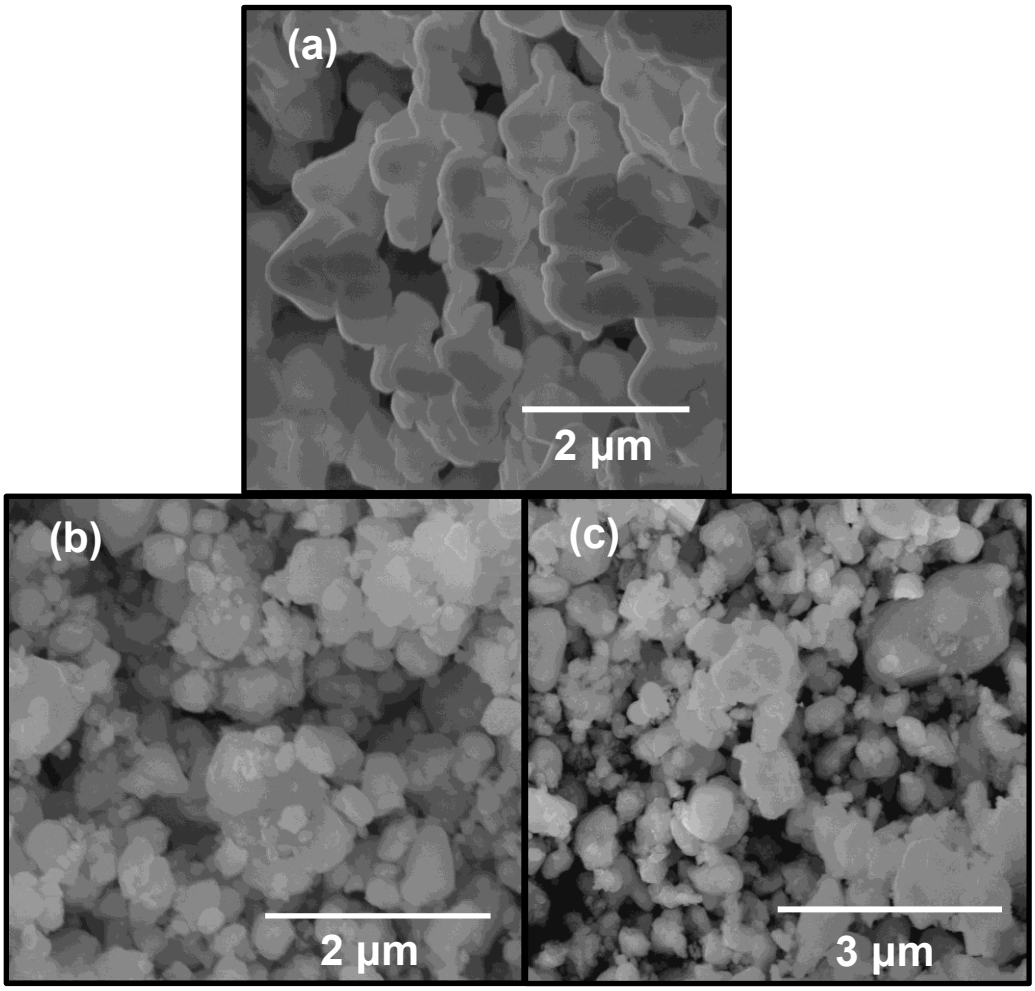

Fig. 30 High magnification SEM micrographs showing (a) as–received TaC powder, (b) TaC powder ball milled for 30 min., and (c) TaC powder ball milled for 60 min.

SEM images also reveal that non-uniform grains are produced in the ball milled powder. The above mentioned observations disclose the fact that, due to the force of impact between the tungsten carbide balls and powder particles the crystallite refinement occurred through repeated brittle fracture. The newly formed particles after the brittle fracture possess high surface energies and have the tendency to form agglomerates. The

size of particles decreased from 0.61±0.34 μm to 0.39±0.16 μm while the powder is ball milled for 30 min. whereas the particle size of 0.42±0.19 μm was observed for 60 min. ball milled powder. A slight increase in particle size for 60 min. ball milled powder was due to formation of agglomerates. This concludes that size of particles decreased with increase in ball milling time, and the rate of refinement decreased. It was reported [45] that a limiting value in particle size can be reached when the compressive stress induced by balls on the individual particles is below the fracture strength of particles. This might be the reason for not seeing much variation in particle size between 30 min. ball milled and 60 min. ball milled powder. It was also reported [43] that only 0.1% reduction in particle size can be attained with ball milling which is the main cause for observing not much variation in particle refinement.

3.1.2 Relative density and microstructure of sintered TaC

Figure 31 below shows the relative density of as-received TaC and ball milled TaC samples. The as-received TaC sample showed an average relative density of ~96%, which confirms that the selected parameters are suitable for attaining a relatively denser sample. The ball milled TaC samples showed nearly full density. This improvement in densification can be attributed to non-uniform grains, reduced grain size, and formation of agglomerates during the ball milling that relatively helps in rearrangement of the starting powder (this phenomena aid in increasing the green density of the sample).

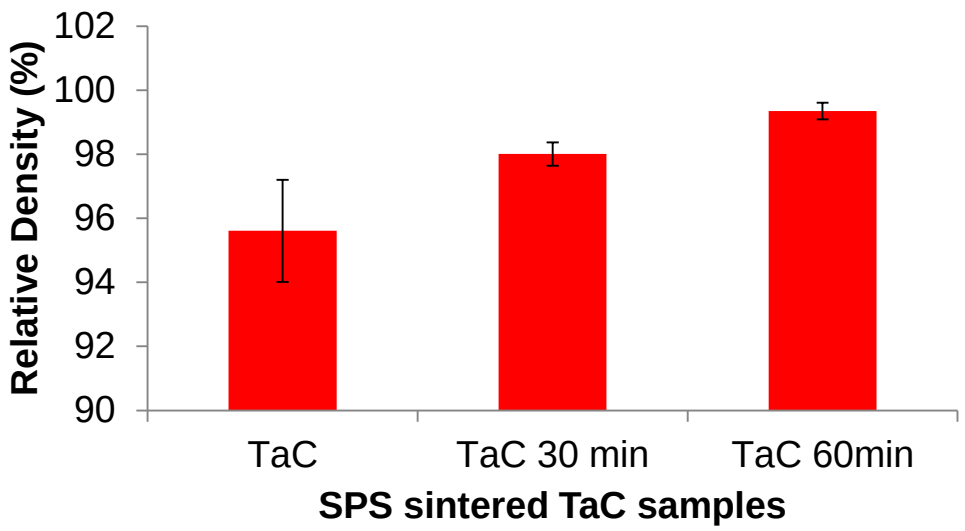

Fig. 31 Relative densities of SPS sintered TaC samples for different ball milling times.

To understand the densification behavior of TaC samples during SPS processing, the instantaneous relative density of as-received TaC and ball milled TaC were calculated by considering SPS displacement data. The attained displacement data was corrected by taking thermal expansion of graphite parts into account. For this correction, first TaC sample was sintered at a pressure of 70MPa for 2000 °C with soaking time of 10 min., and then displacement data was noted. Before sintering, the height of TaC powder bed was noted after applying an initial pressure of 5 MPa. Second, graphite rods were taken and sintered without any TaC powder at the same sintering conditions. The attained displacement of graphite rods was subtracted from displacement data achieved for TaC sample to obtain the displacement only due to TaC powder. The corrected height (L) of the sample was achieved by considering initial height of TaC powder bed and the final instantaneous relative density can be calculated from the following equation.

$$\rho = \left(\frac{L_f}{L}\right)\rho_f \quad \text{(3.1)}$$

where ρ is the instantaneous relative density, L_f is the final height of sample after sintering, L is the corrected height at time t, and ρ_f is the final relative density after sintering.

Figure 32 shows the densification as a function of SPS time and temperature. It can be noticed from Fig. 32 that with increase in ball milling time, the densification curves shift toward the left which indicates that densification is favored at comparatively lower sintering times. These identifications confirm that ball milling improves the sintering kinetics of TaC powder. The fine grain refinement achieved from ball milling and formed agglomerates due to their large area of inter-particle boundaries allowed the ball milled powder to have faster kinetics compared to as-received powder. From Fig. 32, it can be noticed that an initial jump in densification was observed at ~260–290 sec after the start of the sintering process followed by a linear stretch in densification. This phenomenon is mainly attributed to mechanical compaction of the TaC powder. The green density of ball milled samples was more when compared to as-received sample because of the presence of agglomerates. Due to the broad distribution of their size, these agglomerates aid in improving the powder packing density. A deviation from linear stretch was observed at a sintering time of ~840 sec for the as-received sample, ~720 sec for sample in which powder ball milled for 30 min. was used and finally ~540 sec for 60 min. ball milled powder sample. It can be noticed that with increase in ball milling time the linear stretch decreased simultaneously which confirms that densification is

progressively starting at lower sintering times with the use of size reduced crystalline powder attained from ball milling.

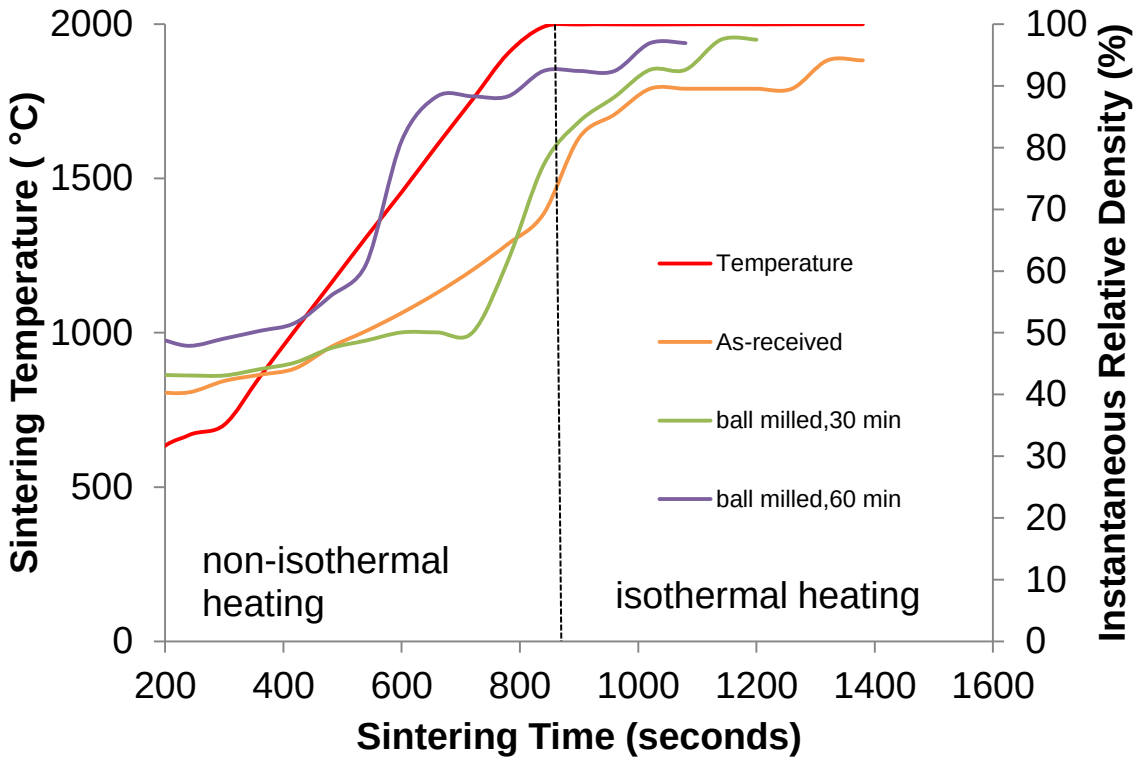

Fig. 32 Variation of sintering temperature and instantaneous relative density with sintering time for as-received TaC and ball milled TaC powders.

The dotted line on Fig. 32 represents the start of soaking time which represents the isothermal heating at 2000 °C. The as-received powder showed a relative density of ~70% at the start of soaking period and final density was attained after 480 sec of isothermal heating, whereas the ball milled samples showed ~77% (30 min ball milled powder) and ~92% (60 min ball milled powder) relative density at the start of isothermal

heating. Due to such high relative densities at the start of isothermal heating, the final densities were attained at lower soaking times of 300 sec and 180 sec respectively. The key reason in attaining higher densities for ball milled samples was due to change in mechanism responsible for mass transport. In the SPS of as-received TaC, the mass transport was done by surface diffusion mechanism where as in ball milled samples, due to formation of non-uniform grains and particle size refinement, the mass transfer was done by grain boundary diffusion. It was reported [88, 89] that during sintering, the surface diffusion only produces neck growth and grain coarsening whereas densification can be attained through grain boundary diffusion. Thus it can be understood that high energy ball milling improves the densification of sintered TaC by refining the particle sizes.

The SEM micrographs from the polished surface of the sintered monolithic samples are shown in Fig. 33. As shown in Fig. 33(a), the TaC sample in which as-received powder was used has uniformly distributed porosity compared to other samples accounting for its lower density. Figure 33 (b) shows the presence of some porosity along with increase in grain size. The grain size of ~16 μm is observed in ball milled TaC samples [Fig. 33(b) and 33(c)]. This increase in grain size is due to prolonged sintering during the soaking period even though nearly full density is obtained at lower soaking times (can be seen from Fig. 32). A fully dense sample without any porosity can be witnessed from Fig. 33(c).

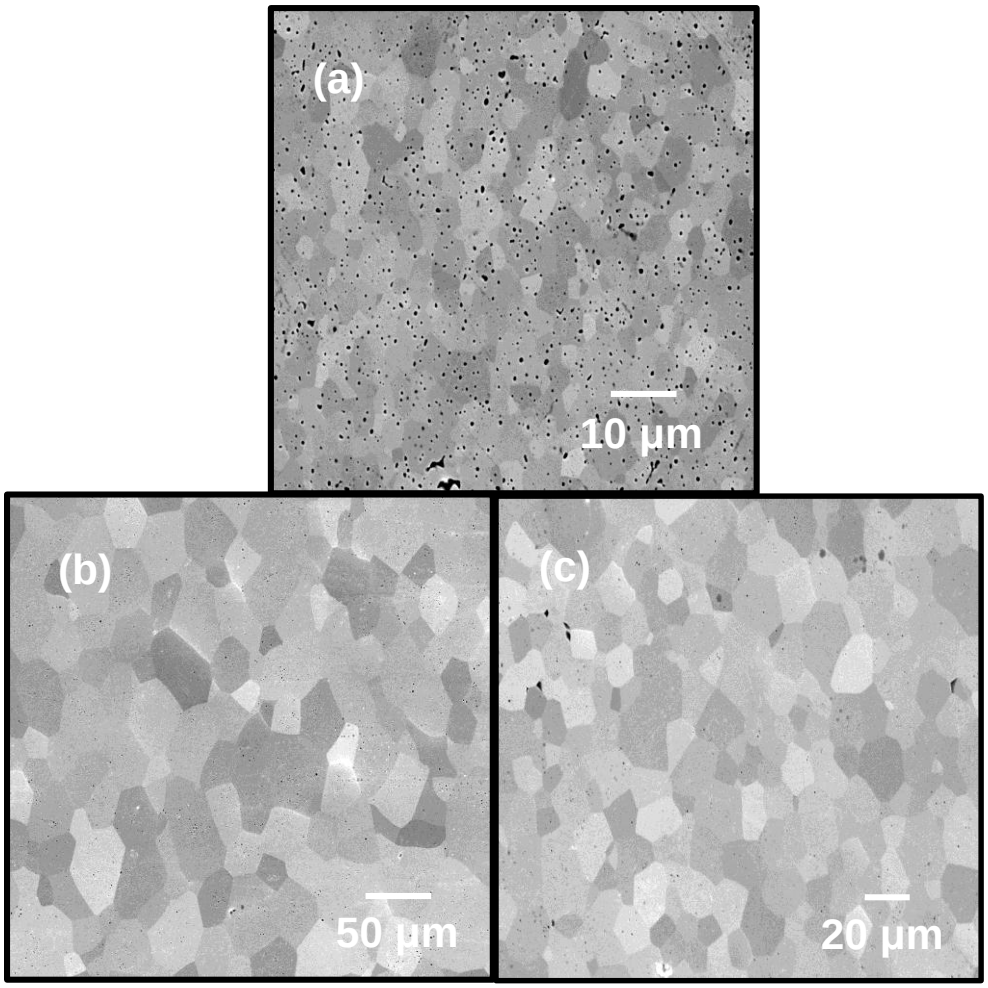

Fig. 33 SEM micrographs from polished surfaces of samples sintered from (a) as–received TaC, (b) TaC ball milled for 30 min., and (c) TaC ball milled for 60 min.

3.1.3 XRD analysis of ball milled and sintered TaC

Figure 34 shows the XRD peaks of as-received and ball milled powders. It can be observed that with increase in milling time, broadness tends to increase. This concludes that crystallite size of the TaC powder decreased with milling time. It is also evident that all the peaks observed belong to TaC and no peak shift was identified. This phenomenon

confirms that ball milling does not introduce any contamination and no phase change occurred with the selected parameters. XRD peaks of the spark plasma sintered TaC samples was also shown in Fig. 35. The position of peaks confirms that no phase change occurred during spark plasma sintering and all the peaks attained belong to TaC.

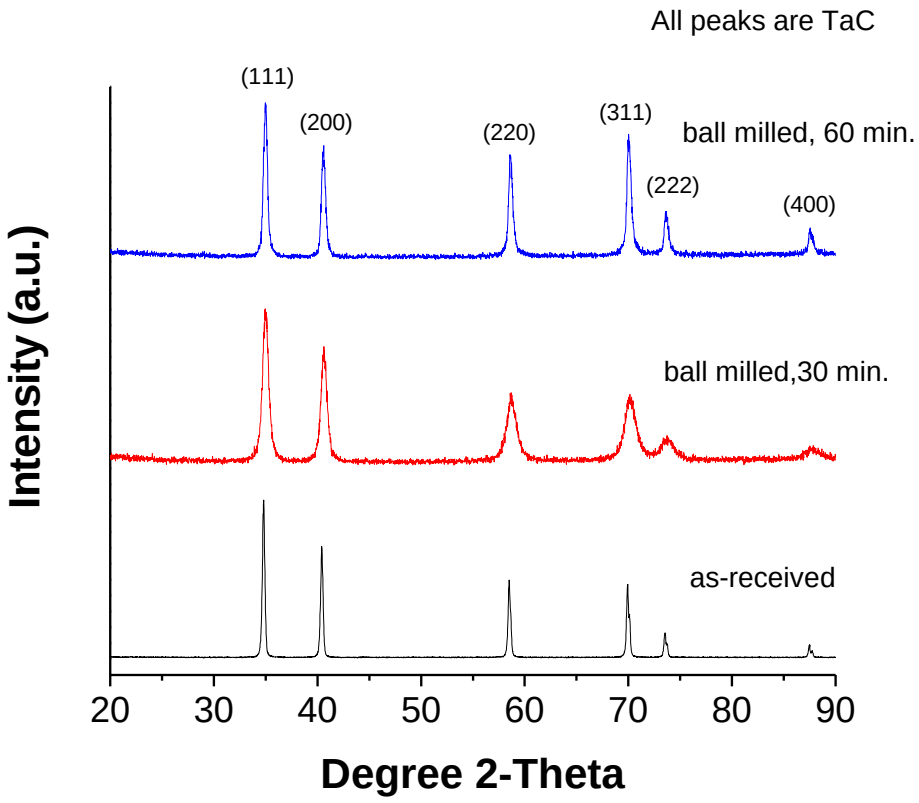

Fig. 34 XRD patterns from as-received and ball milled TaC powders.

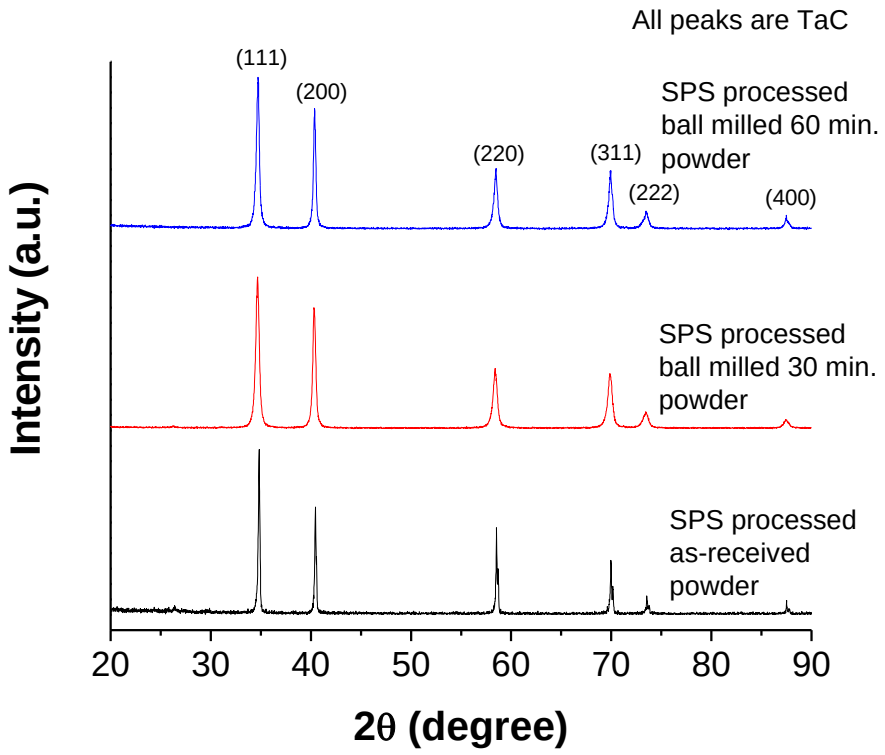

Fig. 35 XRD patterns from SPS sintered as-received and ball milled TaC powders.

3.1.4 Mechanical properties

3.1.4.1 Microhardness

The variation in hardness of as-received TaC with respect to ball milled TaC sintered samples was shown in Fig. 36. A microhardness of ~12 GPa was observed for as-received TaC sample whereas the highest hardness of ~17.6 GPa was attained for TaC ball milled for 30 min. The higher hardness for the ball milled TaC samples compared to TaC was due to higher relative density. The decrease in hardness for higher milling times (compared to 30 min ball milled sample) was due to increase in grain size.

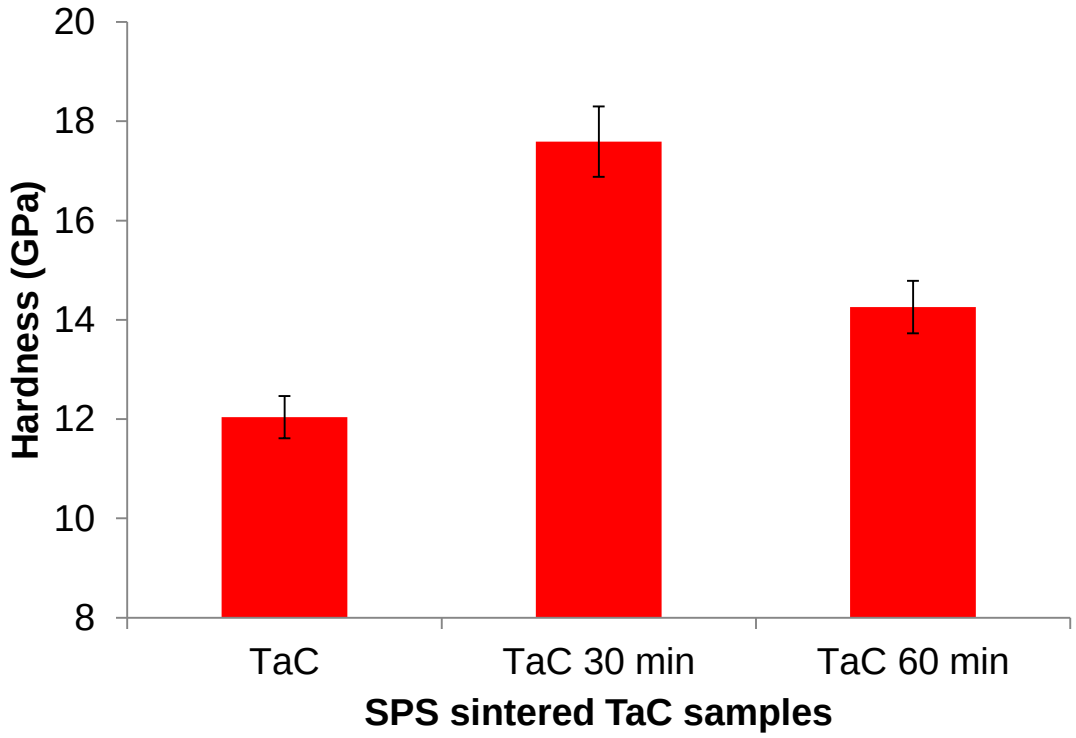

Fig. 36 Hardness of SPS sintered TaC samples for different ball milling times.

3.1.4.2 Flexure strength

Ball milled TaC showed better strength and toughness compared to as-received TaC. TaC ball milled for 60 min. showed highest flexure strength of 339.41±76.87 MPa which was ~150% more than the as-received TaC (135.69±27.39 MPa). This significant improvement in strength was attributed to particle refinement and change in shape of the starting particles from angular to round shape. The increase in relative density also played a key role in improving the flexure strength. Variation of flexure strength for the sintered samples was shown in Fig. 37.

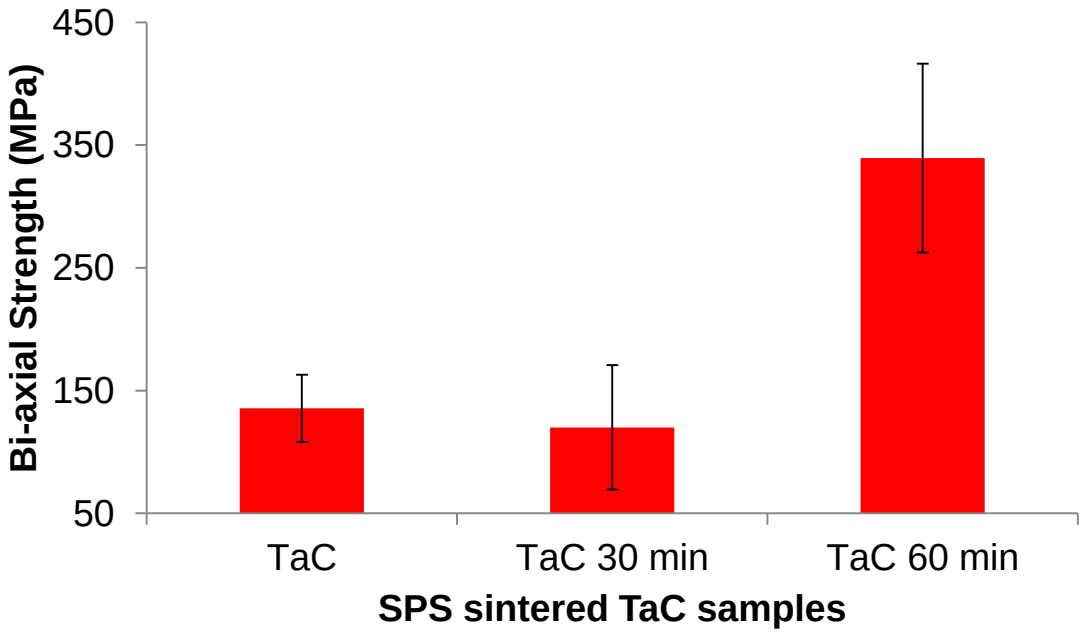

Fig. 37 Bi-axial flexure strength of SPS sintered TaC samples for different ball milling times.

3.1.4.3 Fracture toughness

Significant improvement in fracture toughness was observed in the ball milled TaC composites compared to as-received TaC. The variation of fracture toughness with sintered TaC samples was shown in Fig 38. The fracture toughness of as-received TaC was 1.88±0.23 MPa.m$^{1/2}$. The fracture toughness increased with increase in ball milling time and improved up to ~2.4 MPa.m$^{1/2}$. The highest fracture toughness of 2.39±0.37 MPa.m$^{1/2}$ was achieved for TaC with 60 min of ball milling time, whereas a fracture toughness of 2.09±0.26 MPa.m$^{1/2}$ was attained for 30 min ball milled TaC.

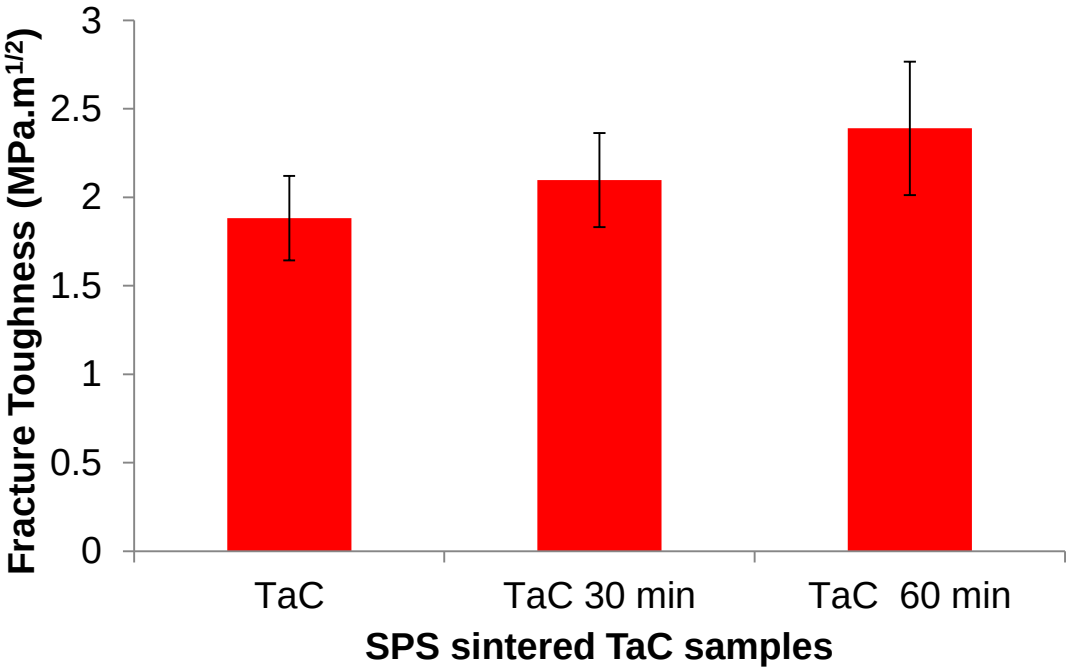

Fig. 38 Indentation fracture toughness of SPS sintered TaC samples for ball milling times.

The significant improvement in fracture toughness of the ball milled TaC is attributed to better relative density and starting particle size refinement. Since the particle size refinement during ball milling occurred through brittle fracture, the fracture strength of the ball milled samples increased (fracture strength of brittle materials increase with decrease in particle size). Figure 39 shows the indentation crack propagation in as-received TaC and ball milled TaC. Trans-granular as well as inter-granular fracture was observed in both as-received [Fig. 39(a) and (b)] and ball milled [Fig. 39(c) and (d)] samples.

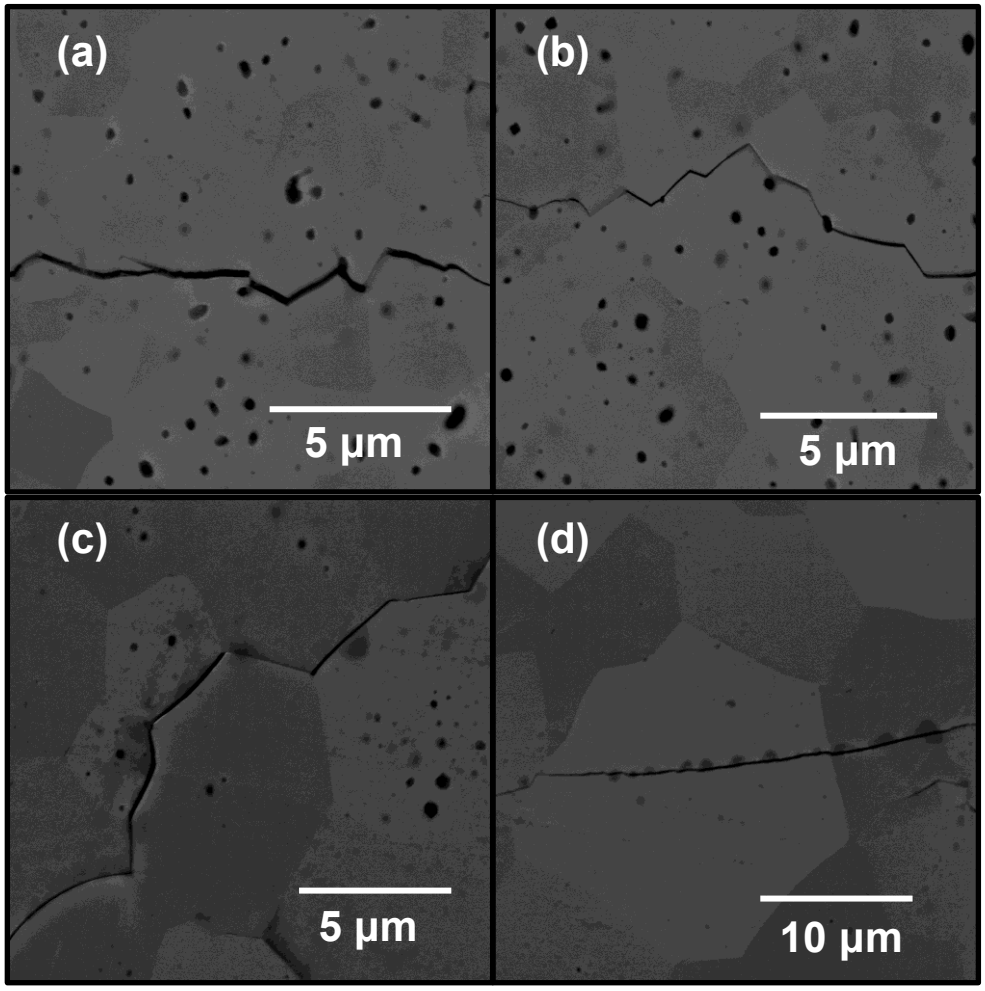

Fig. 39 SEM micrographs showing indentation crack propagation on the polished surfaces of samples SPS sintered from (a-b) as-received TaC, and (c-d) ball milled TaC.

Table 8 provides an overview of attained relative density, grain size and mechanical properties of as-received TaC and ball milled TaC.

Table 8 Relative density, grain size, and mechanical properties of as-received TaC and ball milled TaC.

Sample	**Relative density** (%)	**Grain size** (μm)		**Micro-hardness** (GPa)	**Fracture toughness** ($MPa.m^{1/2}$)	**Flexure strength** (MPa)
		Powder	**Sintered**			
As-received	95.6	0.61±0.34	3.59±1.1	12.04±0.43	1.88±0.24	135.69±27.39
30 min. ball milled	98	0.39±0.16	16.57±5.12	17.59±0.71	2.10±0.27	120.09±50.75
60 min. ball milled	99.4	0.42±0.19	15.92±6.34	14.26±0.53	2.39±0.38	339.41±76.87

3.2 Densification mechanism during spark plasma sintering of TaC

In this investigation, an attempt was made to find the densification mechanism active during spark plasma sintering of TaC by calculating the apparent activation energy. For analyzing the sintering process, we sintered samples at different temperatures ranging from 1700 °C to 2100 °C and studied the data attained during the sintering process.

3.2.1 Relative density and microstructure of SPS processed TaC samples

Figure 40**,** shows the relative density of the spark plasma sintered TaC samples at different temperatures. It can be clearly understood that with increase in temperature, the relative density tends to increase, and nearly full density was attained for TaC sintered at 2100 °C. The SEM micrographs and average grain size of sintered samples was indicated in Fig. 41. The grain size measurement from SEM micrographs reveals that grain size of 0.59±0.15 μm and 0.61±0.16 μm was observed for 1700 °C and 1800 °C sintered samples, whereas grain size of ~2.5 μm was observed for samples sintered at temperatures of 1900 °C-2100 °C. A proximate observation on SEM micrographs confirms that the grain growth initiated at 1900 °C, which is the foremost reason for attaining higher densities beyond the temperature of 1900 °C. On analyzing the data obtained from grain size and relative density measurement, we considered 1900 °C, 2000 °C, and 2100 °C to be the optimal temperatures for calculating activation energy since the average grain size obtained was relatively constant for the selected temperatures.

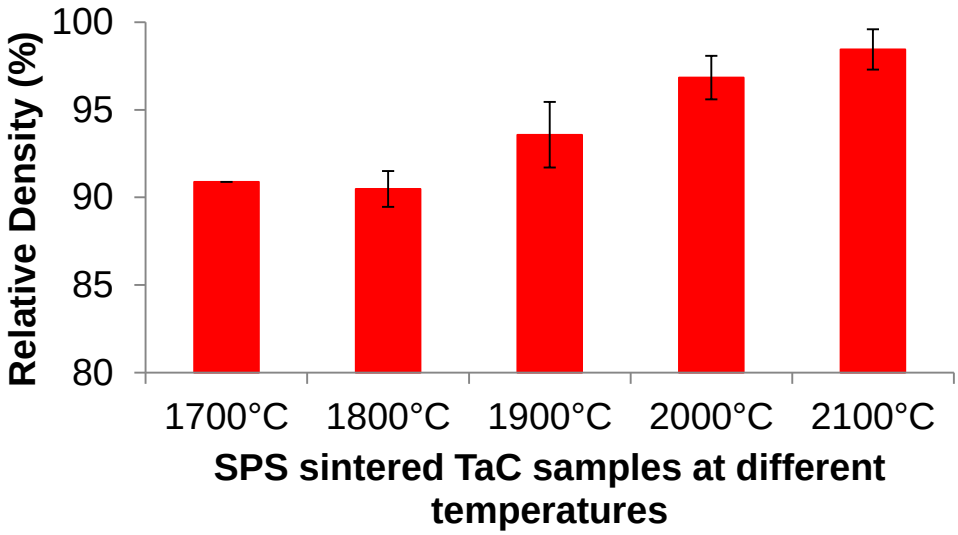

Fig. 40 Relative densities of TaC samples SPS sintered at different temperatures.

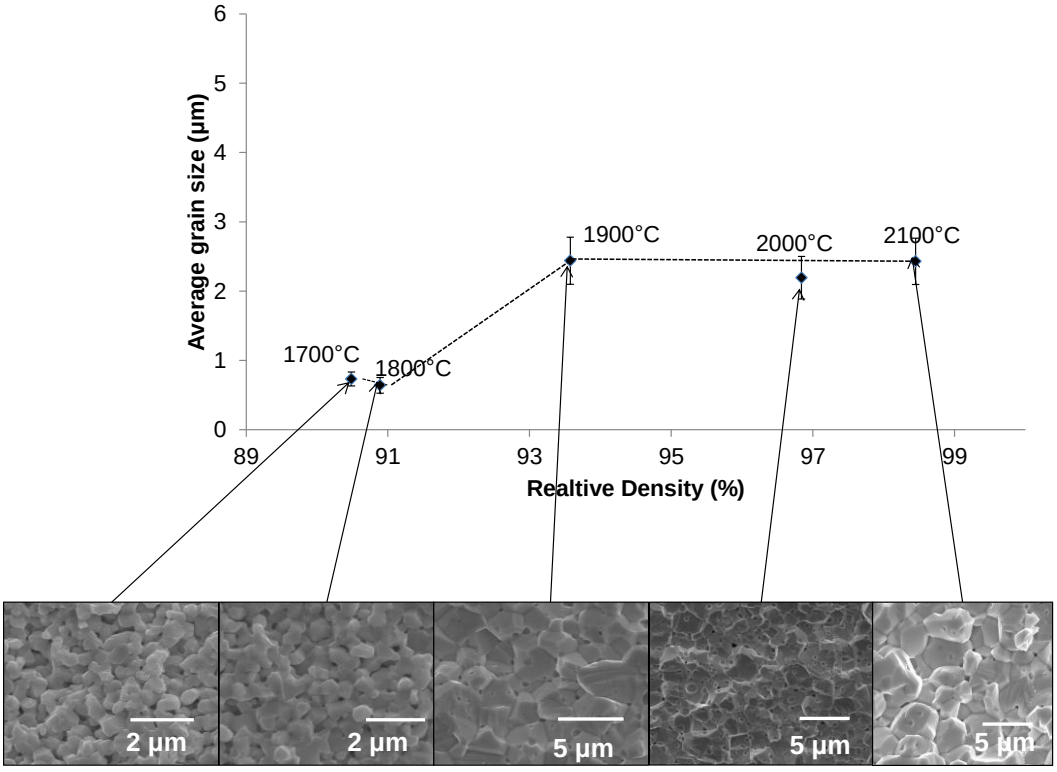

Fig. 41 Variation of average grain size with relative density for the TaC samples sintered at different temperatures.

3.2.2 Densification behavior

To understand the densification behavior of TaC samples during SPS processing, the instantaneous relative density was calculated by considering SPS displacement data. The attained displacement data was corrected by taking thermal expansion of graphite parts into account. For this correction, first TaC sample was sintered at a pressure of 70MPa with soaking time of 10 min. at their particular temperatures ranging from 1700 °C-2100 °C, and then displacement data was noted. Before sintering, the height of TaC powder bed was noted after applying an initial pressure of 5 MPa. Second, graphite rods were taken and sintered without any TaC powder at same sintering conditions. The attained displacement of graphite rods was subtracted from displacement data achieved for TaC sample to obtain the displacement only due to TaC powder. The corrected height (L) of the sample was achieved by considering initial height of the TaC powder bed and the final instantaneous relative density can be calculated from equation.

$$\rho = \left(\frac{L_f}{L}\right)\rho_f \quad \text{..... (3.1)}$$

where ρ is the instantaneous relative density, L_f is the final height of sample after sintering, L is the corrected height at time t, and ρ_f is the final relative density after sintering.

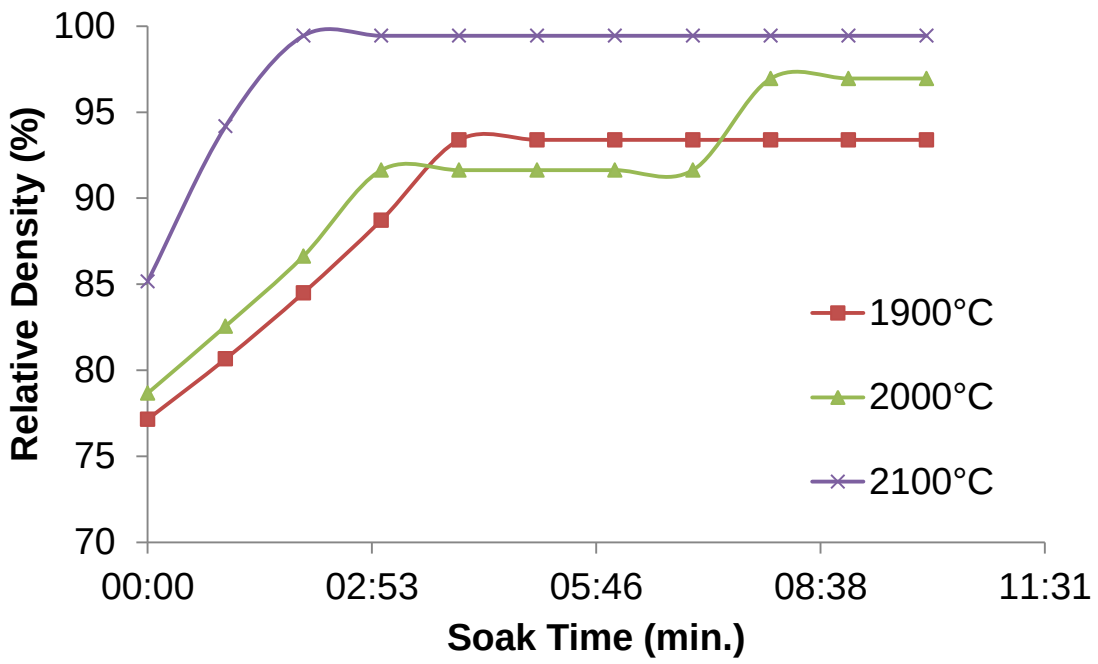

Fig. 42 Variation of instantaneous relative density with soaking time for TaC samples sintered at different temperatures with pressure of 70 MPa.

Figure 42 shows the densification curves obtained for TaC at different SPS temperatures during the soaking time. It is evident that with increase in temperature, the final relative density as well as relative density at the start of soaking time was increased. This phenomenon is very common and similar to results obtained through the general sintering process.

3.2.3 Analysis of sintering mechanisms

Studies done by various researchers [82, 90-92] reveal that densification of ceramic powders during SPS is related to the external load. Power-law creep process is one of the

prominent existing models for predicting the densification mechanism during pressure attributed sintering processes such as hot pressing, spark plasma sintering. The sintering mechanisms during SPS processing of TaC can be established by implementing the analytical model developed for creep by Coble *et al.* [79].

$$\frac{d\varepsilon}{dt} = \frac{1}{\rho}\frac{d\rho}{dt} = A\frac{D\mu_{eff}b}{kT}\left(\frac{b}{G}\right)^{m}\left(\frac{\sigma_{eff}}{\mu_{eff}}\right)^{n} \quad \text{..... (1.4)}$$

where $\frac{d\varepsilon}{dt}$ is the creep rate, ρ is the instantaneous relative density, A is a constant, D the diffusion coefficient, μ_{eff} is the instantaneous shear modulus, b the Burgers vector, T the absolute temperature, G the grain size ,σ_{eff} the instantaneous effective stress applied, m and n are exponents that depend on mechanism of densification.

To attain the densification rate all the unknown terms in the above equation are to be calculated. The instantaneous effective stress (σ_{eff}) can be calculated by using the equation below given by Li *et al.* [93]**.**

$$\sigma_{eff} = \frac{1-\rho_0}{\rho^2(\rho-\rho_0)}\sigma_{mac} \quad \text{..... (3.2)}$$

where ρ_0 is the starting green density of powder, σ_{mac} is the applied pressure (70 MPa).

The effective shear modulus (μ_{eff}) can be given by equation

$$\mu_{eff} = \frac{E_{eff}}{2(1+\upsilon_{eff})} \quad \text{..... (3.3)}$$

where E_{eff} is the effective Young's modulus of TaC, v_{eff} is the effective Poisson's ratio (0.24 for TaC).

According to Lam *et al.* [94], it was given that effective Young's modulus of any porous ceramics can be calculated from the equation

$$E_{eff} = E_{th}\left(1 - \frac{P}{P_0}\right) \quad \text{(3.4)}$$

Where E_{th} is the theoretical Young's modulus of TaC (285 GPa), P=1-ρ the fractional porosity and P_0=1-ρ_0 is the fractional porosity of green body.

On attaining all the values finally, the creep rate equation can be modified as reported by Bernard *et al.* [95].

$$\frac{1}{\mu_{eff}}\frac{1}{\rho}\frac{d\rho}{dt} = \frac{A' \exp\left(-\frac{E_a}{RT}\right)}{T}\left(\frac{b}{G}\right)^m \left(\frac{\sigma_{eff}}{\mu_{eff}}\right)^n \quad \text{(3.5)}$$

Where E_a is the activation energy controlling the densification mechanism during SPS of TaC, R is the gas constant, and A' is a new constant.

Since for applied pressure of 70 MPa, the grain size attained was relatively constant for TaC sintered at 1900 °C-2100 °C (can be seen from Fig. 41), $(b/G)^m$ can be taken as constant, which concludes that the densification mechanism is reliable only on the stress exponent (n). The value of stress exponent n can be calculated from the slope obtained by plotting $ln\left(\frac{1}{\mu_{eff}}\frac{1}{\rho}\frac{d\rho}{dt}\right)$ versus $ln\left(\frac{\sigma_{eff}}{\mu_{eff}}\right)$.

Figure 43 shows the plot of $ln\left(\frac{1}{\mu_{eff}}\frac{1}{\rho}\frac{d\rho}{dt}\right)$ versus $ln\left(\frac{\sigma_{eff}}{\mu_{eff}}\right)$, it is evident that the stress exponent value (n) varies from 1.15 to 1.45. Since the applied pressure was invaried, a constant value for 'n' should be selected and was taken as 1.2.

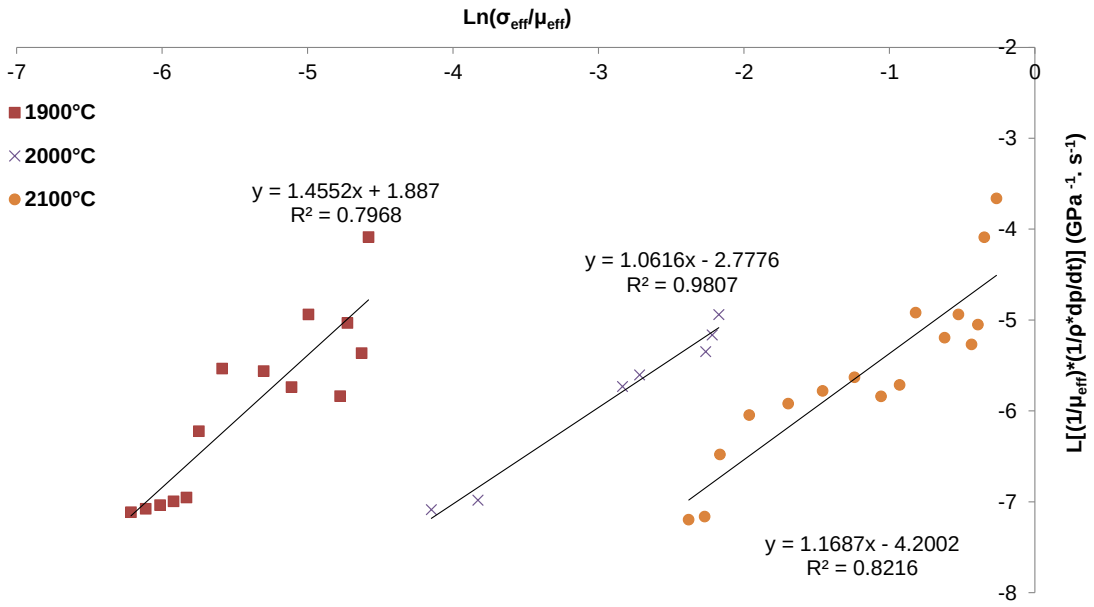

Fig. 43 Linear plot of $ln\left(\frac{1}{\mu_{eff}}\frac{1}{\rho}\frac{d\rho}{dt}\right)$ versus $ln\left(\frac{\sigma_{eff}}{\mu_{eff}}\right)$, at a constant pressure of 70 MPa for TaC powder processed using spark plasma sintering at different temperatures.

As the value of n was fixed, the apparent activation energy can be calculated from modifying the equation for creep rate as

$$ln\left[\frac{T}{\mu_{eff}}\frac{1}{\rho}\left(\frac{d\rho}{dT}\right)\left(\frac{\mu_{eff}}{\sigma_{eff}}\right)^{n}\right] = K' - \frac{E_a}{RT} \quad \text{..... (3.6)}$$

where K' is a new constant.

Figure 44 shows the plot of $ln\left[\frac{T}{\mu_{eff}}\frac{1}{\rho}\left(\frac{d\rho}{dT}\right)\left(\frac{\mu_{eff}}{\sigma_{eff}}\right)^{n}\right]$ versus $\frac{1}{T}$ (Arrhenius plot) from which the value of activation energy can be calculated from the slope obtained. The obtained activation energy for densification of TaC powder through SPS was 99.8 kJ/mol.

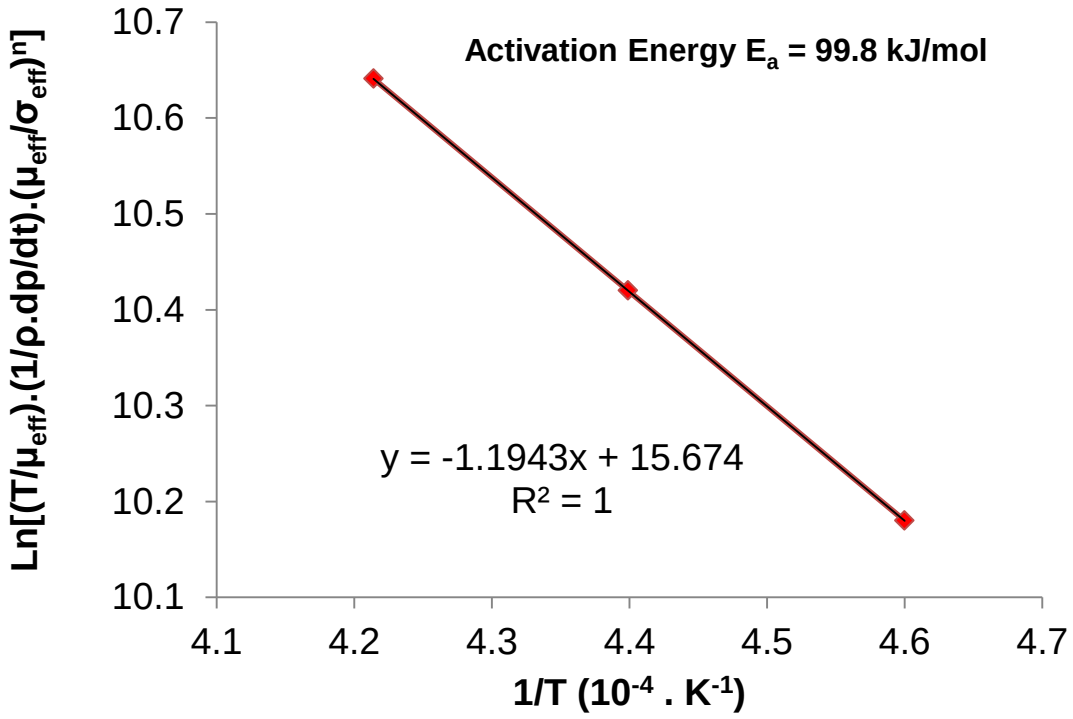

Fig. 44 Apparent activation energy calculated from plot of $ln\left[\frac{T}{\mu_{eff}}\frac{1}{\rho}\left(\frac{d\rho}{dT}\right)\left(\frac{\mu_{eff}}{\sigma_{eff}}\right)^{n}\right]$ versus $\frac{1}{T}$. The slope of the straight line provides the value of –Ea/R.

From the results obtained through sintering by applying power-law creep analysis, the calculated value for activation energy was found to be 100 kJ/mol. The value of activation energy for diffusion of carbon in TaC was reported as 360 kJ/mol when the temperature varies between 1800 °C to 2700 °C [96]. However, the exact value of activation energy for tantalum lattice diffusion is not known. It can be understood that the value is higher than the activation energy for diffusion of carbon into TaC. Even the activation energy decreases with decrease in temperature, the attained activation energy was too low to compare it with the diffusion mechanisms [97].

The conquered stress exponent value from the power law creep as shown in Fig. 43 varies from 1.2±0.2. It was reported by various authors [85, 98],during the spark plasma sintering of ceramics if the stress exponent (*n*) value varies between 1 and 2, grain boundary sliding will be the densification mechanism active during the pressure sintering of ceramics. Such mechanism was reported on TaC by Kim *et al.* [97]**,** in which the authors performed the creep tests at temperatures of 1400 °C and 1500 °C. They prepared the samples using hot pressing at a temperature of 1900 °C with a pressure of 105 MPa for 3 hours. The reported values of stress exponent (*n*) and activation energy for power-law creep were 1.8 and 150 kJ/mol respectively. They also witnessed voids and cracks under the creep conditions and TEM analysis confirmed that grain boundary sliding was the mechanism active during creep. From the reported investigations, it can be proposed that grain boundary sliding is the mechanism active during SPS of TaC powder. Clearly it is evident that TEM investigations are needed to confirm/invalidate the densification mechanism.

3.3 Spark plasma sintering of GNP reinforced TaC composites

In this investigation, GNPs in the vol.% of 2, 4, and 6 were added to TaC and spark plasma sintered at 2000 °C with a pressure of 70 MPa and soak time of 10 min. The effect of GNPs addition on mechanical properties and microstructure of TaC composites was studied and compared with monolithic TaC.

3.3.1 Relative density and microstructure of sintered TaC-GNP composites

The relative density of monolithic TaC and TaC-GNP composites was shown in Fig. 45. It can be observed that no significant improvement in density was observed by adding GNPs (2 and 4 vol.%), whereas an overall density of ~96% was achieved for all the TaC samples by the selected parameters. This confirms that the selected parameters were suitable for achieving better densification of TaC. In GNP added composites, only TaC-6 vol.% GNP showed nearly full density and ~96% density was attained for 2 and 4 percent GNP composites. This is due to non-uniform dispersion of GNPs and low volume fraction of GNP reinforcement in the composite. The improvement in densification of TaC-6% GNP composite can be attributed to rearrangement of the powder particles by applied pressure and mass transfer mechanisms such as necking and grain diffusion caused by pulsed direct current applied during SPS.

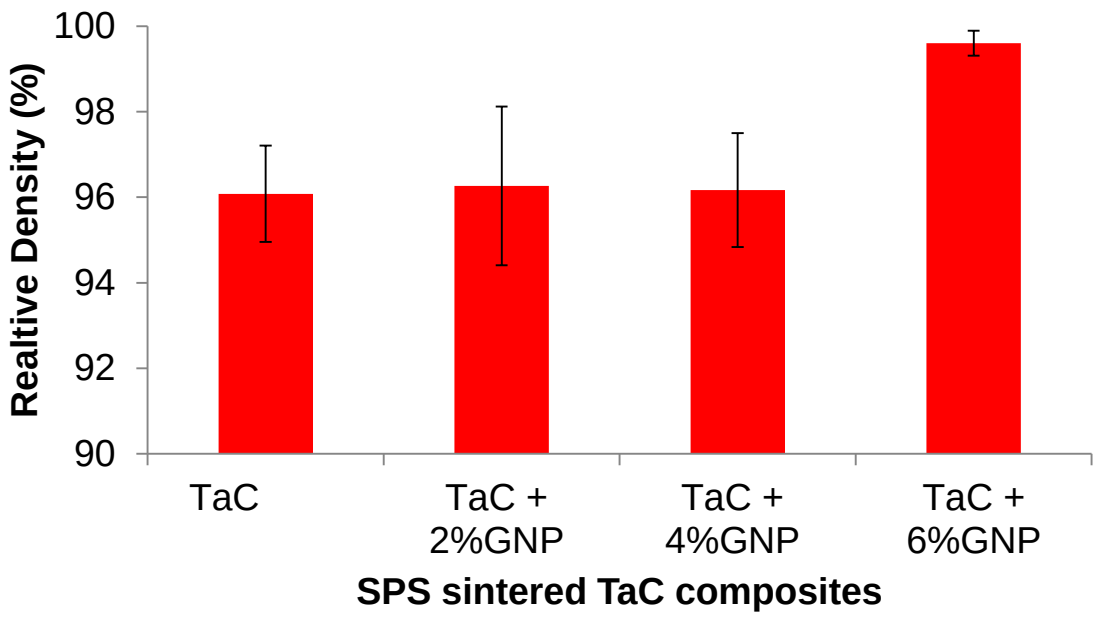

Fig. 45 Relative density of SPS sintered TaC-GNP composites for different compositions.

The SEM micrographs from the fractured surface of monolithic TaC and TaC–GNP composites were shown in Fig. 46. It can be clearly seen that grains are uniform throughout the fracture surface of all the composites. It is also evident that uniformly distributed porosity was observed for monolithic, 2 and 4 vol.% GNP added composites. Figure 46 (a) shows the fracture surface of monolithic TaC with a grain size of 5.16 μm. The survival of GNPs can be observed in all the TaC-GNP composites [Fig. 46 (b), (c), and (d)] along with some grain growth. The 2 and 4 vol.% composites had an average grain size of 7.21 and 6.93 μm respectively whereas 6 vol.% composite showed a grain size of 5.24 μm. A decrease in grain size was observed with increase in GNP content which is in good agreement with the relative density. We noticed that with increase in

reinforcement content, GNPs tend to occupy the porous regions and grain boundaries acted as a hindrance to grain growth and resulted in improving the densification of the composites. The uniform distribution of GNPs in the TaC matrix can also be observed from SEM micrographs.

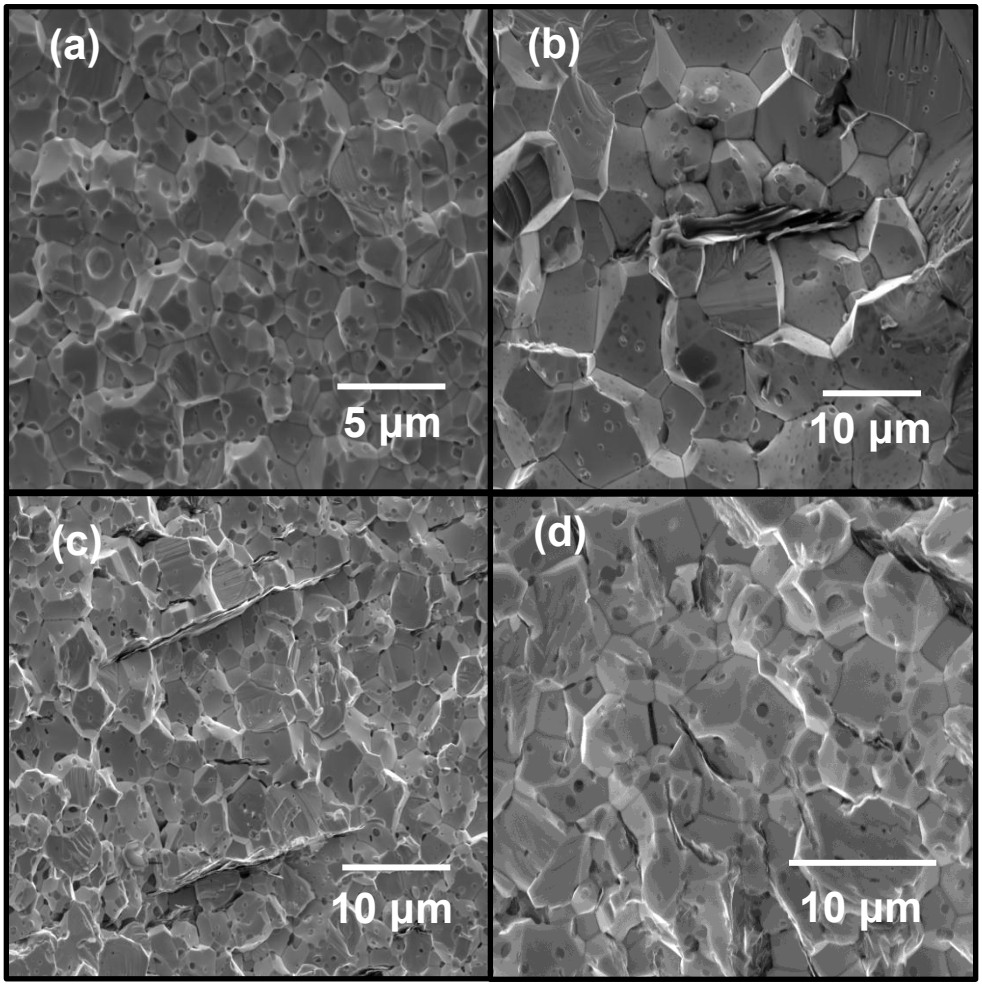

Fig. 46 SEM micrographs from the fractured surfaces of (a) monolithic TaC, (b) TaC-2 vol.% GNP, (c) TaC-4 vol.% GNP, and (d) TaC-6 vol.% GNP composites.

The high magnification SEM images of 4 and 6 vol.% GNP composites were shown in Fig. 47. From Fig. 47(a) it can be seen that GNP sheet was wrapped along the

grain boundaries of the TaC matrix and was pulled out of the fracture surface. Various researchers [39, 42] confirmed that this kind of GNP wrapping helps in strengthening the composites. GNP sheets observed in 6 vol.% composite was shown in Fig. 47(b). It can be seen that a small amount of TaC particle has melted and consolidated on the GNP sheet, which confirms the local melting of TaC due to high localized heating caused by discrepancy in thermal conductivity of GNP and TaC. It was assumed that such type of local melting also helped in improving the overall density of 6 vol.% GNP sample.

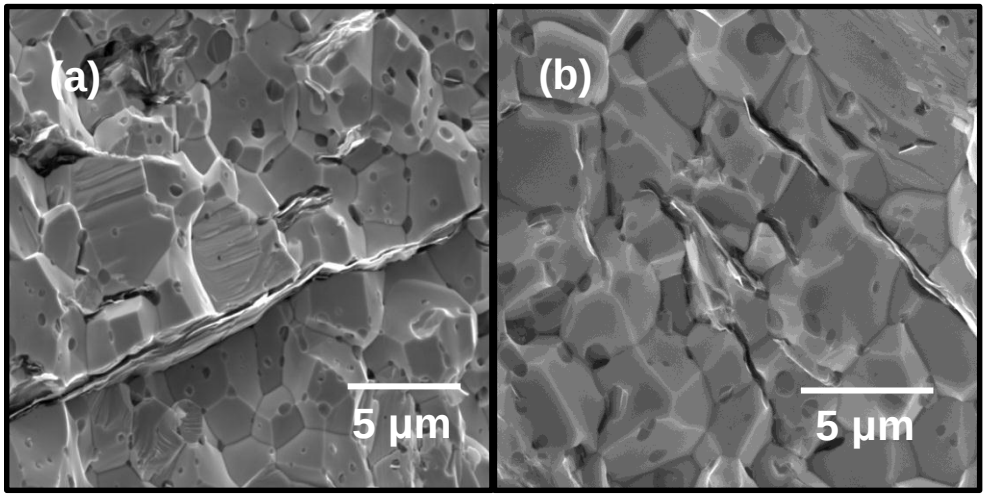

Fig. 47 High magnification SEM micrographs showing GNPs in (a) TaC-4 vol.% GNP, and (b)TaC-6 vol.% GNP composites.

3.3.2 XRD and Raman spectroscopy analysis of GNP reinforced TaC composites

X-ray diffraction (XRD) of the monolithic TaC and TaC-GNP composites was shown in Fig. 48. It was evident that graphene peak at $2\theta=26.6°$ was observed in the TaC-GNP composites. The intensity of peak in TaC-2 vol.% GNP composite was low due to the

very low volume fraction of GNP reinforcement. All other peaks identified belong to TaC and there were no unidentified peaks in the spectra. Thus, XRD analysis reveals the presence of GNPs and confirms that no other interfacial reactions took place during sintering.

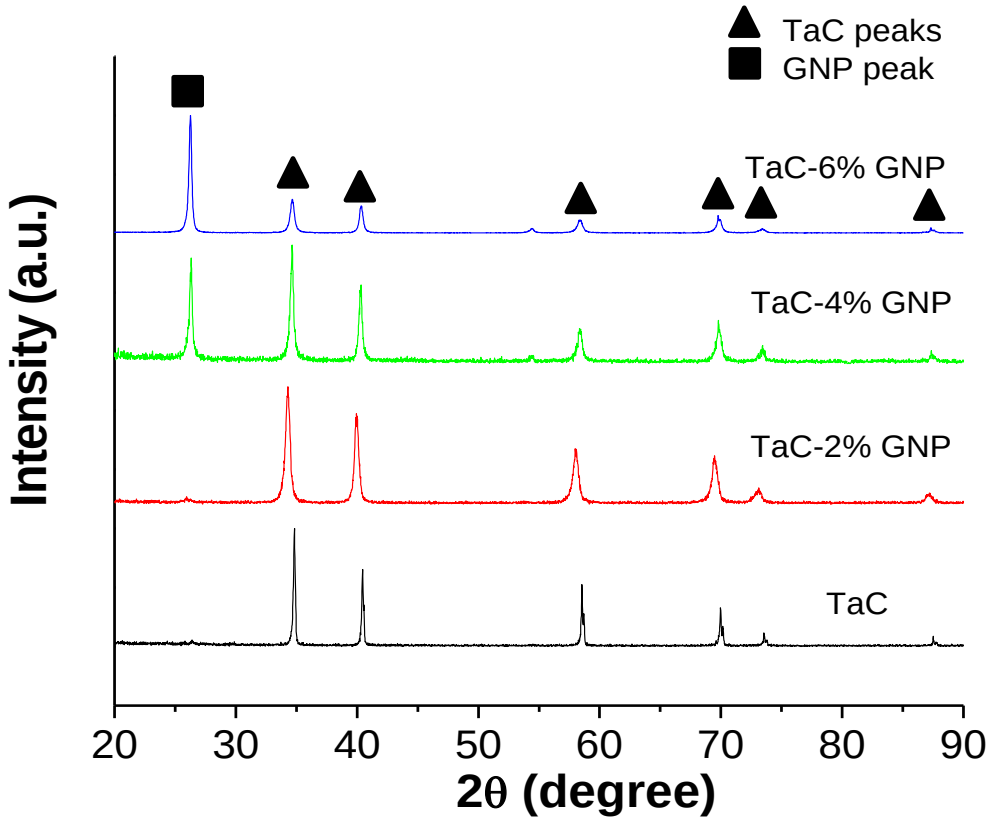

Fig. 48 XRD patterns from SPS sintered TaC and TaC-GNP composites.

Raman Spectroscopy was performed to characterize TaC-GNP composites. For any graphitic carbon, Raman peaks are generally observed at ~1350 cm^{-1} (D-Peak), ~1574 cm^{-1} (G-Peak), ~1620 cm^{-1} (D'-Peak), and ~2700 cm^{-1} (G'-Peak) [99]. The D-peak arises

due to the presence of defects and disorder whereas the stretching of C-C bond gives rise to G-peak. D' and G' peaks represent the higher order modes of D and G peaks respectively [100].

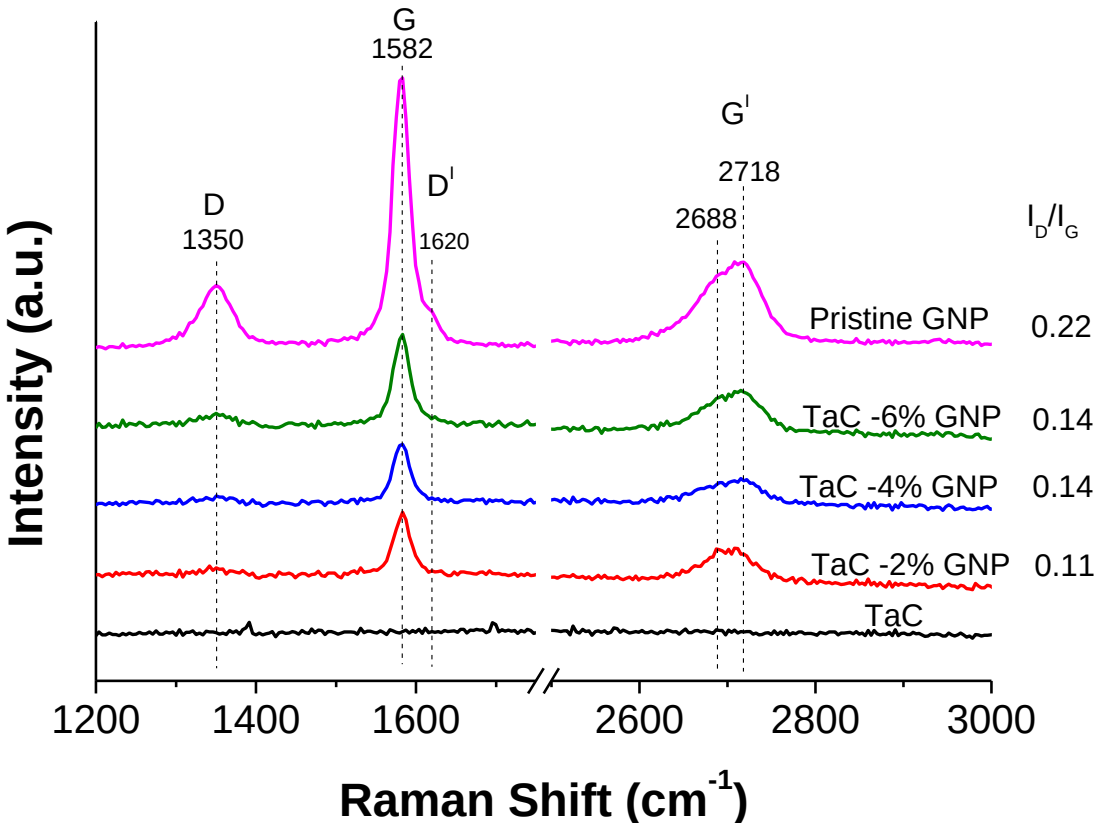

Fig. 49 Raman spectra for pristine GNP, sintered monolithic TaC, and TaC-GNP composites.

Raman spectra acquired from fracture surfaces of TaC, TaC-GNP composites and pristine GNP were given in Fig. 49. For the selected frequency range of 1200-3000 cm^{-1}, Raman peaks were not observed for monolithic TaC whereas peaks were observed at

1582 cm^{-1}, 1620 cm^{-1}, 2718 cm^{-1} that represent GNPs in the composites. Three important observations can be made from Fig. 49.

1) For the sintered samples, the intensity of D peak relative to G peak has been reduced. In addition, D' peaks were not observed which suggests that there are no defects or disorder observed in sintered composites.
2) No shift in G peak for all the composites.
3) G' peak was shifted to lower energy for 2 vol.% GNP composite whereas no peak shift was observed for 4 and 6 vol.% GNP composites.

As mentioned above, the disappearance of D and D' peak from sintered samples reveals that defects were rectified. To confirm this phenomenon, we measured the density of defects by calculating I_D/I_G (ratio of intensities of D to G peaks) value. I_D/I_G value attained for the respective composites were displayed in Fig. 49. Compared to pristine GNP, I_D/I_G value obtained for TaC-GNP composites was low indicating a decrease in density of defects which was due to sintering at high temperatures [101].

G' peak was studied to see whether there was any exfoliation of GNPs occurred. It was evident from Fig. 49 that G' peak shifted towards lower energy in 2 vol.% GNP indicating the decrease in number of GLs [102, 103]. 4 and 6 vol.% GNP composites have not showed any peak shift. Raman spectra for ball milled powders were also shown in Fig. 50. No predominant shift in the position of any of the bands indicates that ball milling does not induce any damage to GNPs.

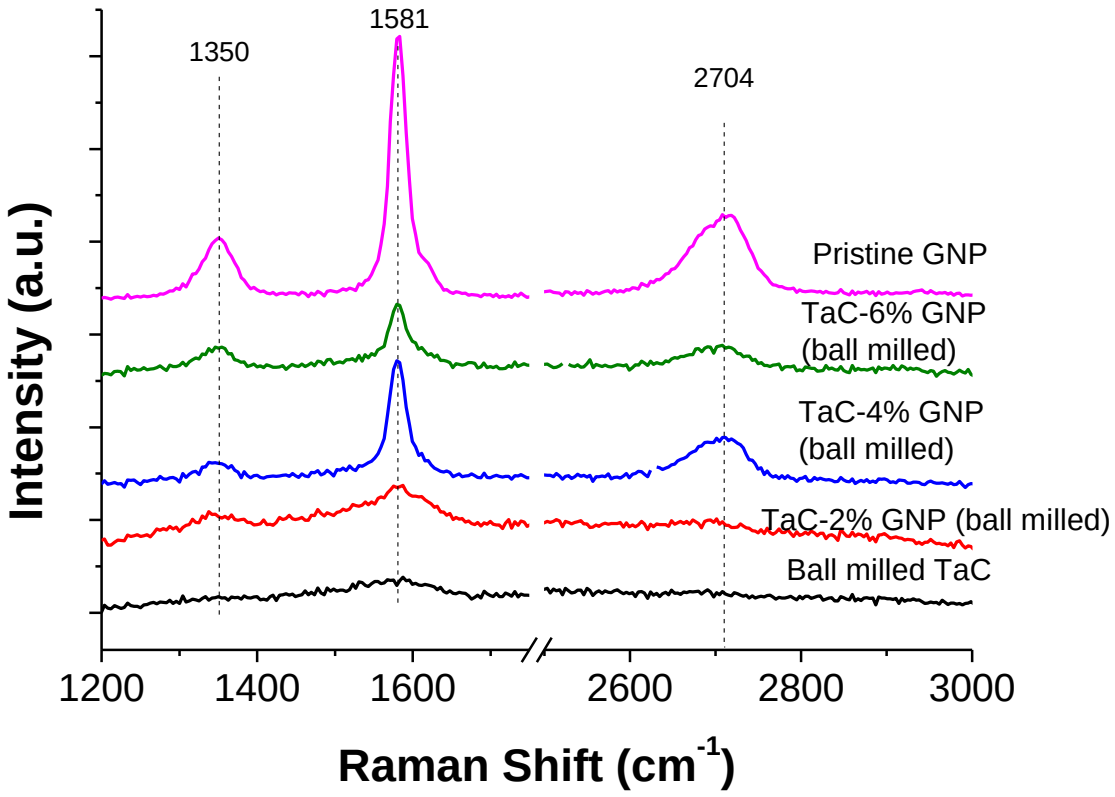

Fig. 50 Raman spectra for pristine GNPs, ball milled TaC, and ball milled TaC-GNP composite powders.

3.3.3 Mechanical properties of TaC-GNP composites

3.3.3.1 Microhardness

The variation in micro hardness of spark plasma sintered TaC composites was shown in Fig. 51. It can be observed that there was no significant improvement in hardness by addition of GNP. The monolithic TaC showed highest average hardness of 12.56±0.34 GPa and hardness tends to decrease with increase in GNP reinforcement content. The 4 and 6 vol.% GNP composites exhibited lower average hardness of 10.93±0.59 GPa, and

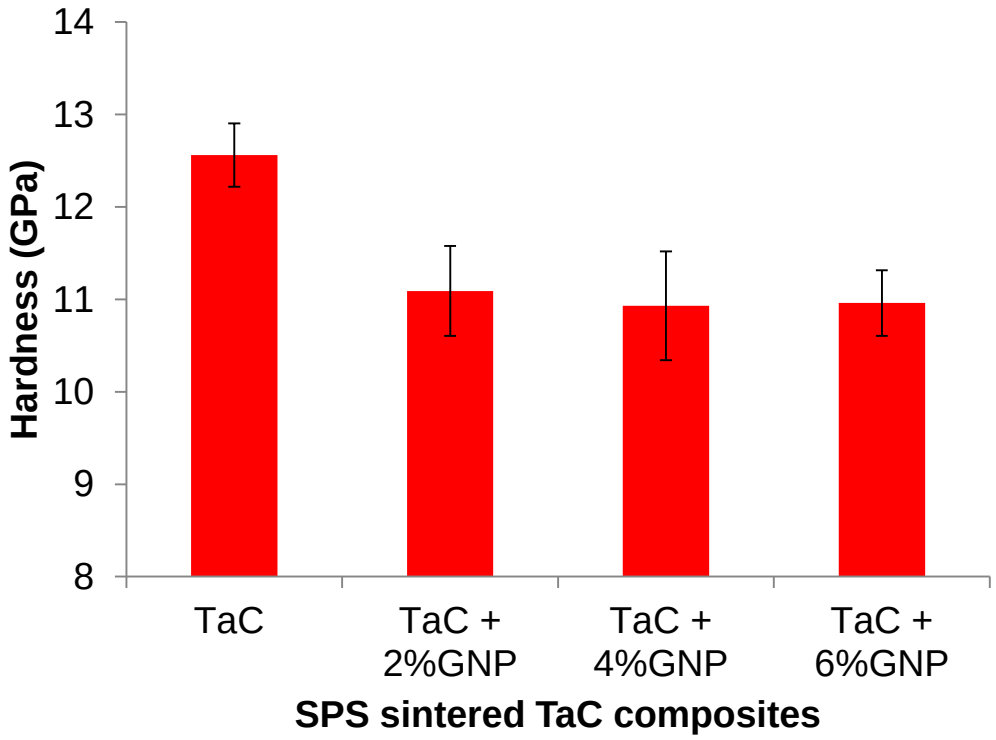

Fig. 51 Hardness of SPS sintered TaC-GNP composites for different compositions.

10.96±0.35 GPa, respectively. The overall decrease in hardness was only attributed to ~12%. Better dispersion of GNPs in the TaC matrix is supposed to increase the hardness of the composite.

3.3.3.2 Flexure strength

The variation of bi-axial flexure strengths obtained for TaC and TaC–GNP composites were shown in Fig. 52. The samples followed a trend of increasing strength with

increasing GNP content. Monolithic TaC and 2 vol.% GNP composite showed biaxial strength of 235±15 MPa and 236±24 MPa which was lower compared to strength of 4 and 6 vol.% GNP composites. The highest flexure strength of 373±35 MPa was attained for 6 vol.% GNP composite whereas 4 vol.% GNP showed flexure strength of 361±49 MPa. The increase in flexure strength for 4 and 6 vol.% GNP composites was as high as 150% compared to monolithic and 2 vol.% GNP composites. The significant improvement in strength can be attributed to uniform distribution of GNPs in the ceramic matrix and anchoring of GNPs along the grain boundaries that inhibits GNP pull out. Better density of TaC-6 vol.% GNP composite contributed in achieving the highest strength.

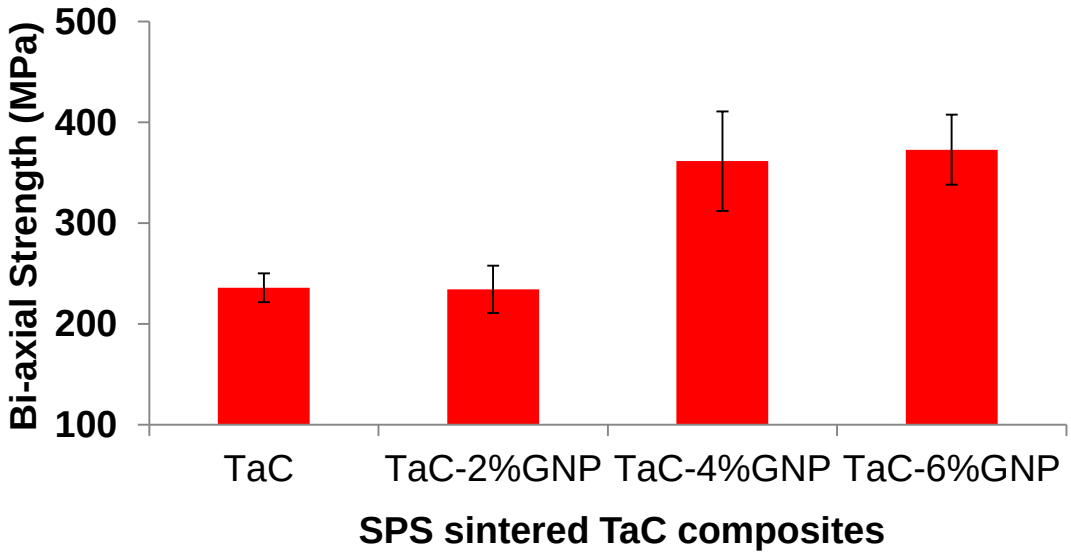

Fig. 52 Bi-axial flexure strength of SPS sintered TaC-GNP composites for different compositions.

3.3.3.3 Fracture toughness

Figure 53 was a plot of the calculated fracture toughness for monolithic TaC and TaC–GNP composites. The plot showed a systematic increase in toughness with increase in GNP concentration in the composites. The highest average toughness of 3.69±1.05 MPa.$m^{1/2}$ was attained for 6 vol.% GNP composite which was 180% higher than the average toughness recorded for monolithic TaC (2.02±0.11 MPa.$m^{1/2}$). The 2 and 4 vol.% composites had an average toughness of 2.65±0.42 MPa.$m^{1/2}$ and 3.61±0.82 MPa.$m^{1/2}$ respectively. This improvement in average toughness for GNP added composites was attributed to novel toughening mechanisms such as crack bridging, crack deflection, and necking of GNP. Better density and good dispersion also resulted in achieving higher average toughness for GNP composites. It can be observed that even though the attained density was relatively same for monolithic, 2, and 4 vol.% GNP composites, the better fracture toughness was recorded for GNP composites due to above mentioned toughening mechanisms.

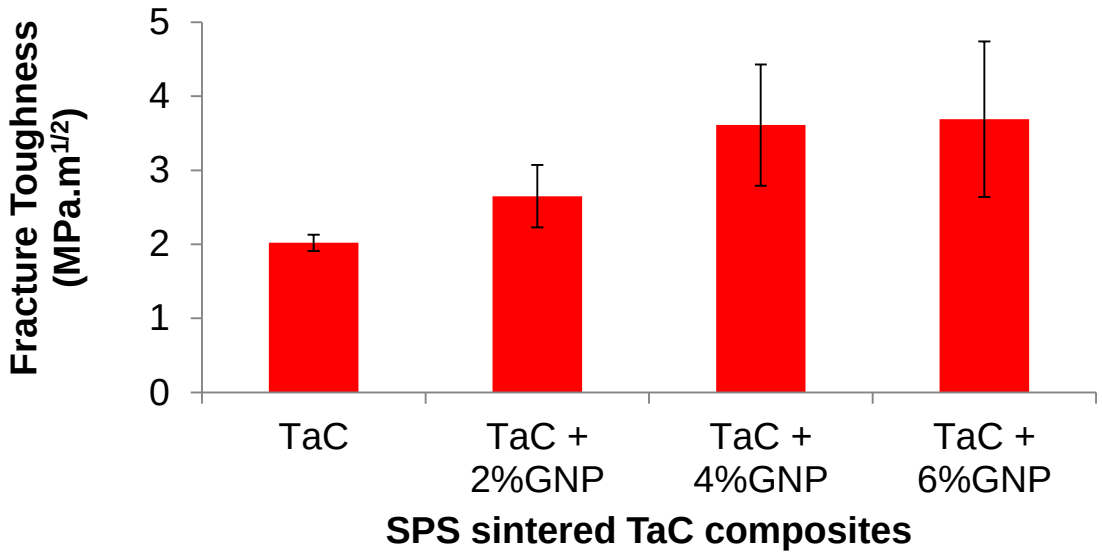

Fig. 53 Indentation fracture toughness of SPS sintered TaC-GNP composites for different compositions.

To study in detail about the crack propagation and toughening mechanisms, we carried out SEM on the polished surface of monolithic TaC and TaC-GNP composites. Figure 54 showed the induced cracks on TaC composites. It was evident that crack propagation in monolithic TaC was relatively straight without any crack deflection, whereas in GNP added composites crack followed a more tortuous path. The investigation revealed that trans-granular crack propagation was prominent in monolithic TaC whereas both inter-granular and trans-granular crack propagation was observed in GNP added composites.

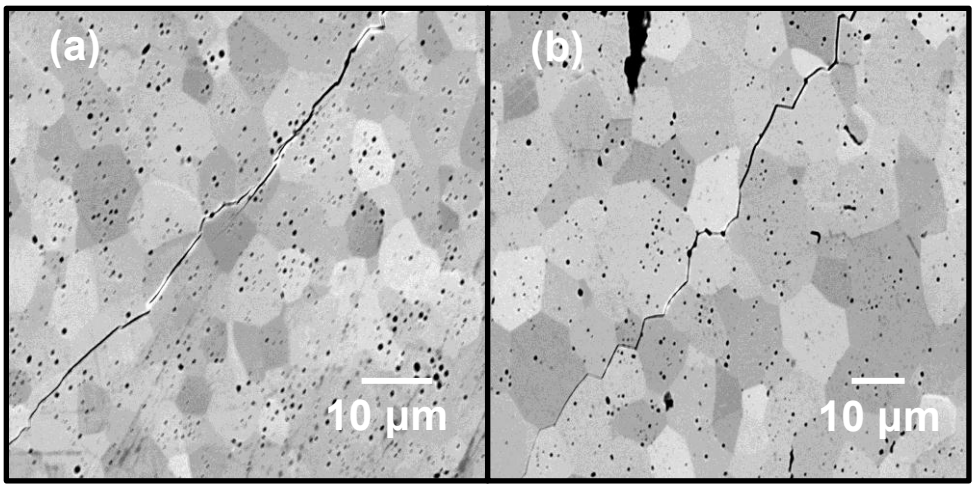

Fig. 54 High magnification SEM micrographs showing crack propagation in (a) monolithic TaC, and (b) TaC-GNP composite.

Table 9 provides an overview of attained relative density, grain size, and mechanical properties of monolithic TaC and TaC-GNP composites.

Table 9 Relative density, grain size, and mechanical properties of TaC and TaC-GNP composites.

Sample	**Relative density** (%)	**Grain size** (µm)	**Microhardness** (GPa)	**Fracture toughness** (MPa.m$^{1/2}$)	**Flexural strength** (MPa)
TaC	96.1	5.16±1.73	12.56±0.34	2.02±0.11	235±15
TaC+2%GNP	96.3	7.21±2.16	11.09±0.49	2.65±0.42	236±24
TaC+4%GNP	96.2	6.93±1.93	10.93±0.59	3.61±0.82	361±49
TaC+6%GNP	99.6	5.24±1.57	10.96±0.36	3.69±1.05	373±35

CHAPTER 4

CONCLUSIONS

- Spark plasma sintering was successfully implemented to sinter monolithic, ball milled TaC and GNP added TaC at high temperatures of 2000 °C and a relative density of >96% was achieved for all the samples.
- XRD analysis of ball milled TaC powder and sintered TaC samples indicated that particle size reduced during ball milling and grain growth occurred during SPS processing. All the observed peaks belonged to TaC which confirmed that no interfacial reactions took place during sintering.
- Significant improvement in microhardness, flexure strength, and fracture toughness of ball milled samples was observed due to better relative densities and particle size refinement of starting powders.
- Analytical model developed for power-law creep was applied to find the densification mechanism active during SPS of TaC powder. Activation energy of 100 kJ/mol and stress exponent (n) of 1.2 was attained; on comparing these values with the literature it was proposed that grain boundary sliding was the active mechanism during SPS of TaC powder.

- SEM micrographs on the fracture surface showed the presence of GNP networks in TaC-GNP composites. Uniform dispersion and anchoring of GNPs along the grain boundaries was also observed in 4 and 6 vol.% TaC-GNP composites.
- Raman spectroscopy analysis indicated that GNPs were successfully retained in TaC-GNP composites without any damage or exfoliation during SPS processing at high temperatures of 2000 °C.
- No hardening effect was observed by addition of GNPs whereas the flexure strength and fracture toughness improved to 150% and 180% respectively. This significant improvement in strength was attributed to better density and novel toughening mechanisms such as sheet pull-out, crack deflection, and crack bridging which were induced due to addition of GNPs to the TaC matrix.
- An attempt was made to find the by assuming that densification of ceramic powders during SPS was related to the external load and an activation energy.

CHAPTER 5

FUTURE WORKS

- Net shaping using spark plasma sintering.
- Laser scattering analysis to determine the exact particle size of ball milled powder.
- TEM analysis to understand in detail about the densification mechanism during SPS of TaC powder.
- Investigate thermal and electrical conductivities of TaC-GNP composites.
- Investigate in detail using Raman Spectroscopy to understand the disappearance of D peak in sintered TaC-GNP composites.

REFERENCES

1. Zhang, X., et al., *Hot pressing of tantalum carbide with and without sintering additives.* Journal of the American Ceramic Society, 2007. 90(2): p. 393-401.
2. Nieto, A., D. Lahiri, and A. Agarwal, *Synthesis and properties of bulk graphene nanoplatelets consolidated by spark plasma sintering.* Carbon, 2012. 50(11): p. 4068-4077.
3. Gasch M.J., E.D.T., Johnson S.M., *Ultra high temperature ceramic composites.* Springer, 2005. 2: p. 197-224.
4. Upadhya, K., J.M. Yang, and W.P. Hoffman, *Materials for ultrahigh temperature structural applications.* American Ceramic Society Bulletin, 1997. 76(12): p. 51-56.
5. Mullendore, A.W., J.B. Whitley, and D.M. Mattox, *Thermal fatigue testing of coatings for fusion reactor applications.* Thin Solid Films, 1981. 83(1): p. 79-86.
6. Liu, L., et al., *Microstructure and mechanical properties of the spark plasma sintered TaC/SiC composites.* Materials Science and Engineering: A, 2011. 529(0): p. 479-484.
7. Monteverde, F., C. Melandri, and S. Guicciardi, *Microstructure and mechanical properties of an HfB_2+30vol.% SiC composite consolidated by spark plasma sintering.* Materials Chemistry and Physics, 2006. 100(2–3): p. 513-519.

8. Zhang, H., et al., *Properties of ZrB_2–SiC ceramics by pressureless sintering.* Journal of the American Ceramic Society, 2009. 92(7): p. 1599-1602.

9. Rangaraj, L., C. Divakar, and V. Jayaram, *Fabrication and mechanisms of densification of ZrB_2-based ultra high temperature ceramics by reactive hot pressing.* Journal of the European Ceramic Society, 2010. 30(1): p. 129-138.

10. Yadhukulakrishnan, G.B., et al., *Spark plasma sintering of silicon carbide and multi-walled carbon nanotube reinforced zirconium diboride ceramic composite.* Materials Science and Engineering: A, 2012. 552(0): p. 125-133.

11. Khaleghi, E., et al., *Spark plasma sintering of tantalum carbide.* Scripta Materialia, 2010. 63(6): p. 577-580.

12. Bakshi, S.R., et al., *Spark plasma sintered tantalum carbide–carbon nanotube composite: Effect of pressure, carbon nanotube length and dispersion technique on microstructure and mechanical properties.* Materials Science and Engineering: A, 2011. 528(6): p. 2538-2547.

13. Chamberlain, A.L., et al., *High-strength zirconium diboride-based ceramics.* Journal of the American Ceramic Society, 2004. 87(6): p. 1170-1172.

14. Wang, H., et al., *Processing and mechanical properties of zirconium diboride-based ceramics prepared by spark plasma sintering.* Journal of the American Ceramic Society, 2007. 90(7): p. 1992-1997.

15. Monteverde, F., *Beneficial effects of an ultra-fine α-SiC incorporation on the sinterability and mechanical properties of ZrB_2.* Applied Physics A: Materials Science & Processing, 2006. 82(2): p. 329-337.

16. DiCarlo, J.A. and H.-M. Yun, *Non-oxide (silicon carbide) fibers handbook of ceramic composites*, N.P. Bansal, Editor 2005, Springer US. p. 33-52.

17. Tang, S.F., et al., *Ablation behaviors of ultra-high temperature ceramic composites.* Materials Science and Engineering a-Structural Materials Properties Microstructure and Processing, 2007. 465(1-2): p. 1-7.

18. Zhang, P., et al., *Processing and characterization of ZrB_2–SiCW ultra-high temperature ceramics.* Journal of Alloys and Compounds, 2009. 472(1–2): p. 358-362.

19. Snyder, A., et al., *Spark plasma sintering of ZrB_2–SiC–ZrC ultra-high temperature ceramics at 1800 °C.* Materials Science and Engineering: A, 2011. 528(18): p. 6079-6082.

20. Kim, P., et al., *Thermal transport measurements of individual multiwalled nanotubes.* Physical Review Letters, 2001. 87(21): p. 215502.

21. Chen, W., X. Tao, and Y. Liu, *Carbon nanotube-reinforced polyurethane composite fibers.* Composites Science and Technology, 2006. 66(15): p. 3029-3034.

22. Choi, H.J., S.M. Lee, and D.H. Bae, *Wear characteristic of aluminum-based composites containing multi-walled carbon nanotubes.* Wear, 2010. 270(1–2): p. 12-18.

23. Efraín, C.-M., *Carbon nanotube metal matrix composites*, in *Dekker Encyclopedia of Nanoscience and Nanotechnology, Second Edition*2009, Taylor & Francis. p. 611-619.

24. Deng, C.F., et al., *Processing and properties of carbon nanotubes reinforced*

aluminum composites. Materials Science and Engineering: A, 2007. 444(1–2): p. 138-145.

25. Tian, W.-B., et al., *Effect of carbon nanotubes on the properties of ZrB_2–SiC ceramics.* Materials Science and Engineering: A, 2008. 487(1–2): p. 568-573.
26. Gao, L., L. Jiang, and J. Sun, *Carbon nanotube-ceramic composites.* Journal of Electroceramics, 2006. 17(1): p. 51-55.
27. Rao, C.N.R. and A.K. Cheetham, *Science and technology of nanomaterials: Current status and future prospects.* Journal of Materials Chemistry, 2001. 11(12): p. 2887-2894.
28. Iijima, S. and T. Ichihashi, *Single-shell carbon nanotubes of 1-nm diameter.* Nature, 1993. 363(6430): p. 603-605.
29. Antunes, E.F., et al., *Comparative study of first- and second-order Raman spectra of MWCNT at visible and infrared laser excitation.* Carbon, 2006. 44(11): p. 2202-2211.
30. Wong, E.W., P.E. Sheehan, and C.M. Lieber, *Nanobeam mechanics: Elasticity, strength, and toughness of nanorods and nanotubes.* Science, 1997. 277(5334): p. 1971-1975.
31. Zhan, G.-D., et al., *Single-wall carbon nanotubes as attractive toughening agents in alumina-based nanocomposites.* Nat Mater, 2003. 2(1): p. 38-42.
32. Jiang, L. and L. Gao, *Fabrication and characterization of carbon nanotube–titanium nitride composites with enhanced electrical and electrochemical properties.* Journal of the American Ceramic Society, 2006. 89(1): p. 156-161.
33. Gonzalez-Julian, J., et al., *Enhanced tribological performance of silicon nitride-*

based materials by adding carbon nanotubes. Journal of the American Ceramic Society, 2011. 94(8): p. 2542-2548.

34. Park, S. and R.S. Ruoff, *Chemical methods for the production of graphenes.* Nat Nano, 2009. 4(4): p. 217-224.

35. Zhu, Y., et al., *Graphene and graphene oxide: synthesis, properties, and applications.* Advanced Materials, 2010. 22(35): p. 3906-3924.

36. Balandin, A.A., et al., *Superior thermal conductivity of single-layer graphene.* Nano Letters, 2008. 8(3): p. 902-907.

37. Wang, F., et al., *Gate-variable optical transitions in graphene.* Science, 2008. 320(5873): p. 206-209.

38. Khan, U., et al., *Development of stiff, strong, yet tough composites by the addition of solvent exfoliated graphene to polyurethane.* Carbon, 2010. 48(14): p. 4035-4041.

39. Rafiee, M.A., et al., *Fracture and fatigue in graphene nanocomposites.* Small, 2010. 6(2): p. 179-183.

40. Watcharotone, S., et al., *Graphene−silica composite thin films as transparent conductors.* Nano Letters, 2007. 7(7): p. 1888-1892.

41. Lee, C., et al., *Measurement of the elastic properties and intrinsic strength of monolayer graphene.* Science, 2008. 321(5887): p. 385-388.

42. Walker, L.S., et al., *Toughening in graphene ceramic composites.* Acs Nano, 2011. 5(4): p. 3182-3190.

43. Suryanarayana, C., *Mechanical alloying and milling.* Progress in Materials Science, 2001. 46(1–2): p. 1-184.

44. Núñez-González, B., et al., *Improvement of the spark-plasma-sintering kinetics of zrc by high-energy ball-milling.* Journal of the American Ceramic Society, 2012. 95(2): p. 453-456.

45. Galán, C.A., et al., *Crystallite size refinement of ZrB_2 by high-energy ball milling.* Journal of the American Ceramic Society, 2009. 92(12): p. 3114-3117.

46. Kim, B.-R., et al., *Mechanical properties and rapid consolidation of binderless nanostructured tantalum carbide.* Ceramics International, 2009. 35(8): p. 3395-3400.

47. Liu, L., et al., *Densification process of TaC/TaB_2 composite in spark plasma sintering.* Materials Chemistry and Physics, 2011. 126(3): p. 459-462.

48. Kim, G.-S., et al., *Microstructure and mechanical properties of a $ZnS–SiO_2$ composite prepared by ball-milling and spark plasma sintering.* Materials Characterization, 2008. 59(9): p. 1201-1205.

49. L.E.Toth, *Transition metal carbides and nitrides*. Refractory Materials, A series of Monographs, ed. J.L.Margrave1971, New York,NY: Academic Press.

50. Pierson, H.O., *Handbook of refractory carbides and nitrides*1996, New Jersey: Noyes. 340.

51. Zhang, X., *Densification and mechanical properties of tantalum carbide and tantalum diboride ceramics*, 2008, Missouri University of Science and Technology: United States -- Missouri. p. 140.

52. Kwon, D.-H., S.-H. Hong, and B.-K. Kim, *Fabrication of ultrafine TaC powders by mechano-chemical process.* Materials Letters, 2004. 58(30): p. 3863-3867.

53. Ma, M., et al., *Synthesis of TaC nanopowders by liquid precursor route.* Materials

Letters, 2011. 65(1): p. 96-99.

54. Monteverde, F., A. Bellosi, and L. Scatteia, *Processing and properties of ultra-high temperature ceramics for space applications.* Materials Science and Engineering: A, 2008. 485(1–2): p. 415-421.

55. Sciti, D., L. Silvestroni, and A. Bellosi, *Fabrication and properties of HfB_2–$MoSi_2$ composites produced by hot pressing and spark plasma sintering.* Journal of Materials Research, 2006. 21(06): p. 1460-1466.

56. Balbo, A. and D. Sciti, *Spark plasma sintering and hot pressing of ZrB_2–$MoSi_2$ ultra-high-temperature ceramics.* Materials Science and Engineering: A, 2008. 475(1–2): p. 108-112.

57. Talmy, I.G., J.A. Zaykoski, and M.M. Opeka, *Synthesis, processing and properties of TaC–TaB_2–C ceramics.* Journal of the European Ceramic Society, 2010. 30(11): p. 2253-2263.

58. Yan, Y., et al., *Pressureless sintering of high-density ZrB_2–SiC ceramic composites.* Journal of the American Ceramic Society, 2006. 89(11): p. 3589-3592.

59. Monteverde, F., *Progress in the fabrication of ultra-high-temperature ceramics: "in situ" synthesis, microstructure and properties of a reactive hot-pressed HfB2–SiC composite.* Composites Science and Technology, 2005. 65(11–12): p. 1869-1879.

60. Balani, K., et al., *Synthesis, microstructural characterization, and mechanical property evaluation of vacuum plasma sprayed tantalum carbide.* Journal of the American Ceramic Society, 2006. 89(4): p. 1419-1425.

61. Tului, M., G. Marino, and T. Valente, *Plasma spray deposition of ultra high temperature ceramics.* Surface and Coatings Technology, 2006. 201(5): p. 2103-2108.

62. Garay, J.E., *Current-activated, pressure-assisted densification of materials*, in *annual review of materials research, Vol 40*, D.R. Clarke, M. Ruhle, and F. Zok, Editors. 2010. p. 445-468.

63. Singh, A.K., *Spark plasma sintering of iron based amorphous alloys, composites, and coatings*, 2010, Oklahoma State University: United States -- Oklahoma. p. 110.

64. M.Tokita, *Mechanism of spark plasma sintering*, Sunitomo Coal Mining Comapny,Ltd: Japan. p. 13.

65. Yadav, V., *Spark plasma sintering of aluminum matrix composites*, 2011, Oklahoma State University: United States -- Oklahoma. p. 107.

66. Cologna, M., B. Rashkova, and R. Raj, *Flash sintering of nanograin zirconia in <5 s at 850°C.* Journal of the American Ceramic Society, 2010. 93(11): p. 3556-3559.

67. Omori, M., *Sintering, consolidation, reaction and crystal growth by the spark plasma system (SPS).* Materials Science and Engineering: A, 2000. 287(2): p. 183-188.

68. Chen, D.-J. and M.J. Mayo, *Rapid Rate Sintering of Nanocrystalline ZrO_2−3 mol% Y_2O_3.* Journal of the American Ceramic Society, 1996. 79(4): p. 906-912.

69. Munir, Z., U. Anselmi-Tamburini, and M. Ohyanagi, *The effect of electric field and pressure on the synthesis and consolidation of materials: A review of the*

spark plasma sintering method. Journal of Materials Science, 2006. 41(3): p. 763-777.

70. Shen, Z., et al., *Spark plasma sintering of alumina.* Journal of the American Ceramic Society, 2002. 85(8): p. 1921-1927.

71. Diouf, S. and A. Molinari, *Densification mechanisms in spark plasma sintering: Effect of particle size and pressure.* Powder Technology, 2012. 221: p. 220-227.

72. Matsugi, K., et al., *A case study for production of perfectly sintered complex compacts in rapid consolidation by spark sintering.* Materials Science and Engineering: A, 2003. 354(1–2): p. 234-242.

73. Xie, G., et al., *Frequency effect on pulse electric current sintering process of pure aluminum powder.* Materials Science and Engineering: A, 2003. 359(1–2): p. 384-390.

74. Heian, E.M., A. Feng, and Z.A. Munir, *A kinetic model for the field-activated synthesis of $MoSi_2$/SiC composites: simulation of SPS conditions.* Acta Materialia, 2002. 50(13): p. 3331-3346.

75. Zhang, X., G.E. Hilmas, and W.G. Fahrenholtz, *Densification and mechanical properties of TaC-based ceramics.* Materials Science and Engineering: A, 2009. 501(1–2): p. 37-43.

76. Bakshi, S.R., et al., *Spark plasma sintered tantalum carbide: Effect of pressure and nano-boron carbide addition on microstructure and mechanical properties.* Materials Science and Engineering: A, 2011. 528(3): p. 1287-1295.

77. Zhang, X., *Densification and mechanical properties of tantalum carbide and tantalum diboride ceramics*, 2008.

78. Vieira, J.M. and R.J. Brook, *Hot-pressing of high-purity magnesium oxide.* Journal of the American Ceramic Society, 1984. 67(7): p. 450-454.

79. Coble, R.L., *Diffusion models for hot pressing with surface energy and pressure effects as driving forces.* Journal of Applied Physics, 1970. 41(12): p. 4798-&.

80. Olevsky, E. and L. Froyen, *Constitutive modeling of spark-plasma sintering of conductive materials.* Scripta Materialia, 2006. 55(12): p. 1175-1178.

81. RAHAMAN, M.N., *Ceramic processing and sintering*. 2nd ed2003, New York,NY: Marcel Dekker.

82. Gendre, M., A. Maître, and G. Trolliard, *A study of the densification mechanisms during spark plasma sintering of zirconium (oxy-)carbide powders.* Acta Materialia, 2010. 58(7): p. 2598-2609.

83. Shvab, S.A. and F.F. Egorov, *Structure and some properties of sintered tantalum carbide.* Powder Metallurgy and Metal Ceramics, 1982. 21(11): p. 894-897.

84. Kislyi, P.S., S.A. Shvab, and F.F. Egorov, *Sintering kinetics of tantalum carbide.* Powder Metallurgy and Metal Ceramics, 1982. 21(10): p. 765-767.

85. Bernard-Granger, G. and C. Guizard, *Densification mechanism involved during spark plasma sintering of a codoped alpha-alumina material: Part I. Formal sintering analysis.* Journal of Materials Research, 2009. 24(1): p. 179-186.

86. Khalil, K.A. and S.W. Kim, *Effect of processing parameters on the mechanical and microstructural behavior of ultra-fine Al_2O_3– (ZrO_2+8%Mol Y_2O_3) bioceramic, densified by high-frequency induction heat sintering.* International Journal of Applied Ceramic Technology, 2006. 3(4): p. 322-330.

87. Ovri, J.E.O., *A parametric study of the biaxial strength test for brittle materials.*

Materials Chemistry and Physics, 2000. 66(1): p. 1-5.

88. Zamora, V., et al., *Crystal-size dependence of the spark-plasma-sintering kinetics of ZrB_2 ultra-high-temperature ceramics.* Journal of the European Ceramic Society, 2012. 32(2): p. 271-276.

89. *Sintering - Theory and practice.* Powder Metallurgy, 1996. 39(4): p. 260-261.

90. Dahl, P., et al., *Densification and properties of zirconia prepared by three different sintering techniques.* Ceramics International, 2007. 33(8): p. 1603-1610.

91. Bernard-Granger, G., et al., *Spark plasma sintering of a commercially available granulated zirconia powder: Comparison with hot-pressing.* Acta Materialia, 2010. 58(9): p. 3390-3399.

92. Ramond, L., et al., *Sintering of a quasi-crystalline powder using spark plasma sintering and hot-pressing.* Acta Materialia, 2010. 58(15): p. 5120-5128.

93. Li, W.B., M.F. Ashby, and K.E. Easterling, *On densification and shape change during hot isostatic pressing.* Acta Metallurgica, 1987. 35(12): p. 2831-2842.

94. Lam, D.C.C. and F.F. Lange, *Microstructural observations on constrained densification of alumina powder containing a periodic array of sapphire fibers.* Journal of the American Ceramic Society, 1994. 77(7): p. 1976-1978.

95. Bernard-Granger, G. and C. Guizard, *Spark plasma sintering of a commercially available granulated zirconia powder: I. Sintering path and hypotheses about the mechanism(s) controlling densification.* Acta Materialia, 2007. 55(10): p. 3493-3504.

96. Resnick, R., R. Steinitz, and L. Seigle, *Determination of diffusivity of carbon in tantalum and columbium carbides by layer-growth measurements.* Journal Name:

Trans. Met. Soc. AIME; Journal Volume: Vol: 233; Other Information: Orig. Receipt Date: 31-DEC-66, 1965: p. Medium: X; Size: Pages: 1915-18.

97. Kim, C., *Deformation behavior and microstructure of tantalum, and processing of carbon-tantalum carbide composites*, 1991, Michigan State University. p. 182.

98. Chaim, R., *Densification mechanisms in spark plasma sintering of nanocrystalline ceramics.* Materials Science and Engineering: A, 2007. 443(1–2): p. 25-32.

99. Ferrari, A.C., et al., *Raman spectrum of graphene and graphene layers.* Physical Review Letters, 2006. 97(18): p. 187401.

100. Dresselhaus, M.S., et al., *Perspectives on carbon nanotubes and graphene Raman spectroscopy.* Nano Letters, 2010. 10(3): p. 751-758.

101. Takai, K., et al., *Effect of heat-treatment on magnetic properties of non-graphitic disordered carbon.* Diamond and Related Materials, 2004. 13(4–8): p. 1469-1473.

102. Jorio, A., et al., *Raman study of ion-induced defects in N-layer graphene.* Journal of Physics-Condensed Matter, 2010. 22(33).

103. Martins Ferreira, E.H., et al., *Evolution of the Raman spectra from single-, few-, and many-layer graphene with increasing disorder.* Physical Review B, 2010. 82(12): p. 125429.

VITA

Ajith Kumar Kalluri

Candidate for the Degree of

Master of Science

Thesis: SPARK PLASMA SINTERING OF TANTALUM CARBIDE AND GRAPHENE REINFORCED TANTALUM CARBIDE COMPOSITES.

Major Field: Mechanical and Aerospace Engineering

Biographical:

Education:

Completed the requirements for the Master of Science in Mechanical and Aerospace Engineering at Oklahoma State University, Stillwater, Oklahoma in December, 2012.

Completed the requirements for the Bachelor of Science in Mechanical Engineering at VIT University, Vellore, India in 2010.

Experience:

- Two years of research experience in processing and characterization of ultra-high temperature ceramics using Spark plasma sintering.
- Tutored undergraduates the concepts of engineering design, modern materials, and advanced processing of engineering materials and trained them on lathe, drilling, and milling machines.
- Student intern at Defense Metallurgical Research Laboratories (DMRL), Pitti Laminations Limited, India.

Professional Memberships:
Student Member of American Society of Mechanical Engineers (ASME).